

2018

Ultralow Wear Fluoropolymer Metal-Oxide Composites: Nanomechanics & Tribochemistry

Mark Alfred Sidebottom
Lehigh University

Follow this and additional works at: <https://preserve.lehigh.edu/etd>



Part of the [Mechanical Engineering Commons](#)

Recommended Citation

Sidebottom, Mark Alfred, "Ultralow Wear Fluoropolymer Metal-Oxide Composites: Nanomechanics & Tribochemistry" (2018).
Theses and Dissertations. 4251.
<https://preserve.lehigh.edu/etd/4251>

This Dissertation is brought to you for free and open access by Lehigh Preserve. It has been accepted for inclusion in Theses and Dissertations by an authorized administrator of Lehigh Preserve. For more information, please contact preserve@lehigh.edu.

Ultralow Wear Fluoropolymer Metal-Oxide Composites: Nanomechanics &
Tribology

by

Mark Alfred Sidebottom

Presented to the Graduate and Research Committee

of Lehigh University

in Candidacy for the Degree of

Doctor of Philosophy

in

Mechanical Engineering

Lehigh University

May 2018

Copyright by Mark Sidebottom

2018

Approved and recommended for acceptance as a dissertation in partial fulfillment of the requirements for the degree of Doctor of Philosophy.

Date

Accepted Date

Committee Members:

Advisor: Dr. Brandon Krick, Mechanical Engineering and Mechanics

Dr. Natasha Vermaak, Mechanical Engineering and Mechanics

Dr. John Coulter, Mechanical Engineering and Mechanics

Dr. Raymond Pearson, Materials Science and Engineering

Acknowledgements

I would like to first acknowledge the hard work and love of my parents, Jilda and John. Mom, I cannot thank you enough for all the support you gave and continue to give me. I recall you making flashcards and quizzing me on multiplication tables constantly during third grade and working so patiently with me on my writing. You always know how to make me feel better when I'm discouraged and upset. Dad, you were and are still the strongest-willed, moral man I know. You are so incredibly selfless in your dedication to your job, waking up at the crack of dawn each day and flying out all over the continent each week for nearly a decade to support our family's dreams. Even after all that work, I always know you still had energy to play with me from little league baseball to our games of ping-pong after dinner when I was in high school.

Secondly, I'd like to acknowledge the companionship and tutoring of my brother Andrew. You are always there when I need someone to talk to, whether it be about school, sports, music, or family. I admire your passion in everything that you do from your work and your drive to make the world a better place. You were my second tutor, only to Mom growing up and you made me a much better student and person than I would have ever been alone.

To my grandparents Wilma and Fred and Mary and John, I have never met a group of kinder souls and thank you for your eagerness to spend time with me from infancy and through adulthood. To my Aunts and Uncles, thank you for all you do to keep our families

connected and strong. Thank you to my cousins, John, Dave, Ryan, Kyle, Nick and Christine for all the childhood memories and continued friendship through adulthood.

I'd like to know acknowledge the loyal friends I made at TCNJ. To Johnny, Andy, G, Nick, Berti & Erica, KOD, Alex, Max, Steve, Bobby, Nate, Walt, Mike, etc. , you all have been so supportive of me through my time at Lehigh. I appreciate all the effort you've continued to make to strengthen our friendship and keep our memories fresh. I'd also like to thank the wonderful professors of the TCNJ School of Engineering, especially Manish Paliwal for your mentorship and guidance through and after TCNJ.

My time at Lehigh has been truly one of growth. I appreciate all the wonderful friends I have made here including Josh & Holly Jones, Chuck Tian, Laura Solomon, Nipun Goel, Ben Lehar, Lindsey Wiebe, Jay Donis, Claire Bohall, and Austin Stewart. I'd like to individually thank Nate Wagenhoffer for his great friendship and support during the past four years. I would also like to Thank all the wonderful staff of the Mechanical Engineering Department, including Dick, Eli, Jimmy, Barbara, Jen, Ali, JoAnn, and Ramona for all your support and wonderful work you do. I want to acknowledge Professors Jaworski, Pearson, and Vinci for their passionate teaching and guidance during my time here.

To my fellow lab mates, Mike Goldstein, Mike Altonji, Rafi Mills, Eric Schell, Sam Zorn, Zakaria Hsain, Sam Joynson, Mike Sedaille, Claudia Kolavonic, Eric Gallant, Kasey Campbell, Tomas Grejtak, Tomas Babuska, and Cooper Atkinson, thank you for being such hardworking, supportive, and understanding. I would like to thank Fiona Cui for all her help and patience with me during the nanoindentation experiments and Gabby Esposito for all her help with DSC and FTIR. To my labmate Guosong Zeng, you are one

of the most genuine people I know, and your advice is always sound. I greatly appreciate how welcoming you are to any questions I may have towards our research and how selfless you are with your time. To John Curry, I am so humbled to have spent the countless number of hours in the lab next to you working on experiments, writing papers, and making illustrator figures. It never felt like work when you, Guosong, Krick and I were all plugging away in the lab. Beyond the lab, you and Brionna became some of my closest friends.

Outside of the lab, I would like to thank the great students of the Lehigh Cross Country and Track and Field I've been fortunate enough to coach. You all were such a wonderful outlet for me and allowed me to continue to improve as a runner. I learned so much from the countless conversations I had with you all during my runs. Thank you to the LU XC/TF coaching staff: Deb, Brooke, Carl, Matt, and Ryan for all your support while I've been here. Special thanks to head men's cross country coach Todd Eters and his wife Edann, you truly listened to the input I had on the team and were always understanding of my situation. You are both wonderful parents and great examples for the athletes that you coach.

Last, I want to thank my advisor, Brandon Krick. Ever since you interviewed me over the phone nearly five years ago asking me if I wanted to work in your lab, you've been one of my greatest supporters. You were incredibly selfless with your time and truly cared about me, not just what I did as a researcher. This was evident in how much you supported me as a runner. I believe that many others in your situation would have suggested that I stop running competitively or not coach. Instead you were always tracking my progress, rooting me on during my races, or the first one in the hospital when I broke my

arm. I am especially appreciative of all the career mentoring you've given me over the past year, spending hours revising and editing my teaching and research statements and preparing for job interviews. It has been a pleasure being a part of your lab from day one and seeing it grow into the wonderful research program you've developed and will continue to guide.

Preface

This document is broken into individual chapters, each with a specific purpose. The first chapter provides a brief description of the field of tribology (the study of interfaces in contact, i.e. friction, wear, adhesion etc.), with a specific focus on types and applications of solid lubricant materials. Friction coefficient and wear rate are defined in this chapter to provide necessary context for the remainder of document. The second chapter serves as a general background to the types and properties of fluoropolymers. A review of the relevant tribological literature on fluoropolymers and fluoropolymer composites is presented here. Chapter three discusses the motivation for this current thesis and provides a preliminary hypothesis for the ultralow wear of fluoropolymer-metal-oxide composites. The following chapter (Chapter four), discusses the methods used in material synthesis, tribometry, the metrics of friction coefficient and wear rate in more detail, and brief descriptions common characterization techniques used throughout the dissertation. This concludes the introductory portion of this work.

The next four chapters each discuss a singular aspect of interest for the Fluoropolymer-metal-oxide composite solid lubricant system. These chapters are meant to be self-supporting and do not need to be read in order. Each of these chapters is broken into the following sections: overview, motivation, hypothesis, materials and methods, results and discussion, and conclusion. The conclusion of each chapter is written as a list that highlights the key findings of the chapter. The Conclusions chapter connects the findings from the previous four chapters into a single mechanistic framework.

Table of Contents

Acknowledgements.....	iv
Preface.....	viii
Table of Contents.....	ix
List of Tables.....	xv
List of Figures.....	xvii
Abstract.....	1
Chapter 1: Introduction to Tribology.....	3
1.1 Definition and importance of tribology.....	3
1.2 Solid Lubricants: Applications and Types.....	4
1.3 The metrics of tribology: friction coefficient and wear rate.....	5
1.4 Plain Journal Bearing Example.....	7
Chapter 2: Fluoropolymers and Fluoropolymer Composites in Tribology.....	9
2.1 Types and properties of fluoropolymers.....	9
2.2 Microstructure of PTFE and PFA.....	11
2.3 Tribological properties of unfilled and filled fluoropolymer composites.....	14
2.3.1 Unfilled PTFE.....	14
2.3.2 Overview of PTFE composites for tribological applications.....	21

2.3.3 Overview of ultralow wear PTFE α -alumina composites.....	27
Chapter 3: Motivation and Research Hypothesis.....	33
Chapter 4: Materials and Methods.....	36
4.1 Material Synthesis Procedures	36
4.1.1 PTFE and PTFE-Metal Oxide Composite Synthesis Procedure.....	36
4.1.2 PFA Synthesis Procedure.....	37
4.2 Tribometers, friction coefficient, and wear rate measurements	39
4.2.1 Linear Reciprocating Tribometer.....	39
4.2.2 Friction measurements	39
4.2.3 Wear Rate Measurements	40
4.3 Characterization Methods.....	41
4.3.1 Surface Metrology: Coherence Scanning Interferometry (Scanning White Light Interferometer) and Stylus Profilometry	41
4.3.2 Nanoindentation Methods.....	44
4.3.3 Infrared Spectroscopy (Attenuated Total Reflectance, Transmission, and Reflectance).....	46
4.3.4 Differential Scanning Calorimetry (DSC)	48
4.3.5 X-Ray Diffraction (SAXS and WAXS).....	51

Chapter 5: Nanomechanics of Metal-Oxide Filler Particles lead to Ultralow Wear	
Fluoropolymers	53
5.1 Overview	53
5.2 Motivation	54
5.3 Hypothesis	58
5.4 Materials and Methods	58
5.4.1 Materials and Material Preparation.....	58
5.4.2 Tribological Experiments.....	59
5.4.3 In-Situ Nanoindentation Experiments.....	61
5.5 Results & Discussion.....	63
5.5.1 Friction and Wear Results.....	63
5.5.2 Running Film and Transfer Film Development.....	66
5.5.3 Infrared Spectroscopy of Running Films	70
5.5.4 Nanoindentation Results	73
5.6 Conclusions	80
Chapter 6: Ultralow Wear Melt Processible Fluoropolymer Alumina Composites	83
6.1 Overview	83
6.2 Motivation	84
6.3 Hypothesis	86

6.4 Materials and Methods	86
6.4.1 Materials Tested and Sample Preparation.....	86
6.4.2 Tribometer.....	88
6.4.3 Wear Rate Measurements	88
6.4.4 Experiment Conditions	88
6.4.5 Infrared Spectroscopy	89
6.5 Results & Discussion.....	89
6.5.1 Tribological behavior.....	89
6.5.2 Effect of pressure, PFA grade, and filler percentage of unfilled versus filled PFA	93
6.5.3 Tribofilm morphology	94
6.5.4 Tribofilm characterization (Infrared Spectroscopy)	95
6.5.5 Mechanistic Discussion	97
6.6 Conclusions	99
Chapter 7: Effect of Sliding on Microstructure of PFA.....	101
7.1 Overview	101
7.2 Motivation	101
7.2.1 Microstructure and Melt Behavior.....	103
7.3 Hypothesis	105
7.4 Materials and Methods	106

7.4.1 Materials Used	106
7.4.2 Tribological Testing.....	106
7.4.3 Differential Scanning Calorimetry.....	107
7.4.4 X-Ray Diffraction	107
7.4.5 Transmission Infrared Spectroscopy.....	108
7.4.6 Attenuated Total Reflectance Infrared (ATR-IR).....	108
7.5 Results and Discussion	109
7.6 Conclusion.....	123
Chapter 8: Environmental effects on tribological performance of PFA and PFA alumina composites	126
8.1 Overview	126
8.2 Motivation	127
8.2.1 Preliminary Experiments: Effect of relative humidity on wear, friction and tribofilm formation	128
8.3 Hypothesis	129
8.4 Materials and Procedure	129
8.5 Results & Discussion.....	131
8.5.1 Friction performance as a function of relative humidity	131
8.5.2 Wear rate as a function of relative humidity.....	132

8.5.3 Tribofilms	134
8.5.4 ATR-IR Results	136
8.6 Conclusions	138
Chapter 9: Conclusions	141
References	143
Vita.....	152

List of Tables

Table 1: Properties of Various Fluoropolymers.....	10
Table 2: Flexural Modulus and Flex Life (fatigue resistance) as a function of crystallinity for PTFE [10].	12
Table 3: Particle manufacturer and reported particle size of metal-oxide particles used in PTFE composites.....	59
Table 4: N ₂ Gas adsorption (BET, specific surface area), and Static Light Scattering (SLS, true particle diameter) of metal-oxide particles composited with PTFE.	59
Table 5: Friction coefficient for the five PTFE metal-oxide composite materials averaged over the first 10,000 cycles, 50,000 cycles, the entire experiment (500,000 cycles), and for the last 200,000 cycles	66
Table 6: Wear rates for the five PTFE metal-oxide composite materials averaged over the first 10,000 cycles, 50,000 cycles, the entire experiment (500,000 cycles), and for the last 200,000 cycles	66
Table 7: List of PTFE and PFA resin types, alumina filler used, and amount of filler used in fluoropolymer composites experiments run in this chapter.	87
Table 8: Differences between the grades of Chemours ® PFA are listed in the table below:	87
Table 9: Initial and final wear rates and friction coefficients (μ) for various weight percentages of Al ₂ O ₃ in PFA and PTFE composites tested. K_{initial} is the mass based	

wear rate after 1,000 sliding cycles. K_{final} is the final differential mass-based wear rate: for unfilled polymers this is the final 5,000 sliding cycles (from 5,000 to 10,000 total cycles); for filled polymers this is the final 200,000 sliding cycles (from 300,000 to 500,000 total cycles). μ_{initial} is the average friction coefficient over first 1,000 cycles and μ_{final} is the average friction coefficient for the last experiment (i.e. 5,000 to 10,000 total cycles for unfilled and 300,000 to 500,000 total cycles for filled) 93

Table 10: Different grades of PFA used for tribological tests. PPVE= $\text{CF}_2\text{CFOC}_3\text{F}_7$, PEVE= $\text{CF}_2\text{CFOC}_2\text{F}_5$. Melt flow rate is a crude approximation for molecular weight (lower molecular weight fluoropolymer flow easier and typically crystallize easier than high molecular weight fluoropolymers..... 106

Table 11: DSC data for the solid-solid transition for all PFA grades tested (bulk and wear debris) for the primary melt..... 109

Table 12: DSC data for all PFA grades tested (bulk and wear debris) for the primary melt. 109

Table 13: Wear rates as a function of relative humidity for unfilled and 5 wt. % PFA-Alumina composites. The number of cycles within the parenthesis represents the number of cycles tested when the total wear rate (total volume lost divided by total sliding distance and average applied force) was calculated. K_{final} is the wear rate during the last 200k sliding cycles. 134

List of Figures

Figure 1: US energy consumption by energy source, sector, and overall efficiency [4]. ...	4
Figure 2: Common contact geometries of various tribometers.....	6
Figure 3: Example of journal bearing lifetime prediction using wear rates for PTFE, Rulon Maroon (PTFE and Glass Fibers), and ultralow wear PTFE/Alumina Composite.....	8
Figure 4: Spherulite schematic adopted from Sperling [12].	11
Figure 5: Visual description of PTFE microstructure. (a) SEM micrograph of replica of fractured PTFE surface [95] .(b) PTFE fiber arrangement of stacked crystalline and disordered regions.(c) Crystalline slice ~20 nm in thickness within PTFE fiber.(d) Spacing between the rigid polymer chains within the crystalline region [84].	13
Figure 6: Switchboard model for semi-crystalline polymer likely formed by PFA. Reprinted with permission from [13].	14
Figure 7: Friction of PTFE on PTFE (49% crystalline) as a function of sliding speed Reprinted with permission from [17].	15
Figure 8: Effect of temperature (a) and pressure (b) on wear rate as a function of sliding speed. Reprinted with permission from [19].	16
Figure 9: Wear debris formation of PTFE caused by shear during sliding. Reprinted with permission from [16].	18

Figure 10: Wear rate of unfilled PTFE as a function of kinetic friction coefficient for a range of testing temperatures. Reprinted with permission from [23].	19
Figure 11: Mode-II fracture model for wear of unfilled PTFE. Maximum allowable sliding velocity and minimum temperature for mild wear of PTFE are defined in equations 5&6 respectively. Reprinted with permission from [23].	20
Figure 12: Wear volume versus number of revolutions of PTFE-carbon fiber composites against mild steel of increasing roughness measured by center line average roughness (Ra) (graphitic-non-abrasive, non-graphitic-abrasive) [37].	22
Figure 13: Wear rate of PTFE composited with a variety of fillers as a function of sliding velocity at 10 N load [18].	25
Figure 14: FTIR spectra of transfer film. Peaks corresponding to carboxylate salts (1650 cm^{-1} , 1432 cm^{-1}), waters of hydration (3388 cm^{-1}), and CF_2 from PTFE backbone (1152 cm^{-1} , 1206 cm^{-1}). Reprinted with permission from [48].	29
Figure 15: Mechanically driven chain reaction of PTFE- Al_2O_3 composite forming carboxylic acid endgroups which bond to active sites on the metal counterface and alumina particles. Reprinted with permission from [48].	31
Figure 16: (a) Cold press and sintering process for PTFE- Al_2O_3 composites. (right) Screw injection molding process for PFA - Al_2O_3 composites.	33
Figure 17: Injection molded PFA Al_2O_3 composite samples. (left: simple plaque geometry, right: block-on-ring plaque with four samples	38

Figure 18: Linear reciprocating tribometer and flat-on-flat contact schematic.	39
Figure 19: Basic elements of a Coherence Scanning Interferometer [59].	42
Figure 20: Diagram of how constructive interference occurs at each point along the surface as the objective lens scans vertically [59].	43
Figure 21:a) Typical load-displacement curve for nanoindentation experiment, (b) Diagram of contact area before, during and after indentation. Reprinted with permission from [60].	45
Figure 22: Simplified principles of the transmission infrared spectroscopy technique....	47
Figure 23: Schematic of attenuated total reflectance infrared light spectroscopy.	48
Figure 24: Schematic of major components of a differential scanning calorimetry plot..	50
Figure 25: Wear rate of PTFE-Alumina composites was shown to drop by 100x for particles below 500nm threshold by Blanchet et al. The friction coefficient for both systems was found to be independent of particle size. Reprinted with permission from [41].	54
Figure 26: Difference observed in transfer films of PTFE composited with different size alumina fillers. Reprinted with permission from [41].	55
Figure 27: Summary of wear rate versus supplier designated particle size. The outlier particle in circled in red which is micro in size but still ultralow wear [62].	57
Figure 28: Indentation Data Analysis Procedure. (Top) Load does not begin immediately, as tip is still approaching the particle's surface, which may affect hardness and	

modulus calculations. (Bottom) Depth data is shifted so loading begins at zero contact depth.....	60
Figure 29: Schematic of load as a function of time for particle indents. The slope of the unloading curves was taken from the first 10% of the data.	62
Figure 30: Tribological Results for alumina filled PTFE experiments. (a) friction coefficient as a function of sliding distance (note x-axis is logarithmic) (b) Volume lost vs sliding distance for all three PTFE Al ₂ O ₃ composites tested. Slope of these curves corresponds to the wear rate (steep slope-higher wear, shallow slope-lower wear rate)	63
Figure 31: Photograph images of the worn surface of the five composite samples are highlighted before testing, after 1,000 cycles (50 m), after 5000 cycles (250 m), after 10,000 cycles (500 m), and after 500,000 cycles (25 km).	67
Figure 32: Scanning White Light Profilometry scans across the transfer film of the five types of PTFE-metal oxide composites. The maximum depth across each scan and wear rate over the last 10km of sliding (200k cycles) is highlighted on the right hand side of the figure.	69
Figure 33: Attenuated total reflectance infrared spectra of various PTFE-Alumina particles before testing and after 500k sliding cycles (25km).	71
Figure 34: Summary of in-situ nanoindentation experiments. (a) experiment setup (b) all load vs displacement curves (c) load displacement curves for experiment with maximum load less than 2000 μ N (d) all load indentation curves of experiments with	

less than 4000 μ N maximum load (e) All loading curves for experiments with maximum loads of greater than 4000 μ N.....	73
Figure 35: (Top) Hardness values for all indentation experiments. (Bottom) Reduced Modulus values for all indentation experiment. Error bars are due to the statistical scatter of the four unloading curves within each indent. The porous particles did not complete the prescribed loading cycle and the hardness values reported are just an average of the completed unloading curves.	76
Figure 36: Alumina particle hardness as a function of maximum indentation depth. With increasing indentation depth, lower particle hardness was observed overall.	78
Figure 37 : TEM image of PTFE-Al ₂ O ₃ composite surface (porous 4 μ m).Reprinted with permission from [62]	79
Figure 38: X-ray microtomography of PTFE-Al ₂ O ₃ (porous 4 μ m) micrograph after completion of all wear experiments. Reprinted with permission from [62].	79
Figure 39: Visual framework for the role of alumina filler particles in reducing the wear of bulk PTFE and the formation of tribofilms.....	82
Figure 40: Friction coefficient of unfilled PFA 340 and PTFE over 10,000 cycles [73].	89
Figure 41: Friction coefficient versus sliding distance of PFA 340 with 5.0, 7.5, and 10.0 wt. % alumina, and PTFE with 5 wt. % alumina on linear (a) and semi-log (b) scales.	90

Figure 42: (a) Volume lost versus sliding distance for PFA 340 and PFA 340 Al₂O₃ composites. (b) Volume lost versus sliding distance for first 50,000 sliding cycles. (c) Volume lost versus sliding distance for entire 500,000 sliding cycle experiment [73].
..... 91

Figure 43: Effect of pressure, PFA grade, and filler weight percentage on friction and wear. 93

Figure 44: Tribofilms of PFA 340 and PFA 340 with Al₂O₃ [73]. 95

Figure 45: (a) ATR spectra of bulk and worn surfaces of PFA unfilled and PFA with 10 wt% Al₂O₃. Note that the chemical differences are only truly noticeable between the worn PFA composite surface. All other surfaces tested have nearly identical chemical spectra. (b) FTIR spectrum of transfer film formed from sliding PFA with 10 wt. % Al₂O₃ on 304L stainless steel countersample [73]. 97

Figure 46: Tribochemical mechanism for formation of perfluorocarboxylate salts in PFA- α Alumina composites. R_f is the fluorinated end of the perfluorinated alkyl vinyl ether side group. 99

Figure 47: Typical DSC curves of PFA and microstructure schematic. The sub-ambient solid-solid transition is associated with the transition of PFA crystallites from a triclinic crystalline structure to a hexagonal crystalline structure at higher temperatures. Crystalline portions of PFA are composed of TFE rich sections and are represented in the DSC curves in the large melting endotherms in the high temperature region. 103

Figure 48: DSC curves of the first, heat, crystallization and second heat of PFA 440 (1.5 mol.% PPVE) and its wear debris.	110
Figure 49: DSC curves of the first, heat, crystallization and second heat of PFA 416 (1.9 mol.% PPVE) and its wear debris.	112
Figure 50: DSC curves of the first, heat, crystallization and second heat of PFA 950 (3.4 mol.% PEVE) and its wear debris.	113
Figure 51: XRD data for PFA (1.5 mol. % PPVE) bulk and wear debris. Reduced FWHM of the wear debris sample correlates with a larger apparent crystallite size (D).	115
Figure 52: Sub-ambient solid-solid transition temperature for wear debris and bulk PFA of various comonomer concentrations. It should be noted that the high mol. % comonomer sample is PEVE and the two smaller comonomer concentrations are PPVE.	118
Figure 53: a) Transmission infrared spectra of PFA (1.5 mol. % PPVE) bulk and wear debris. b) Inset of carboxylic acid region of ATR spectra highlighting the free carboxylic acids only present in the bulk sample, which are formed after chain scission of the PFA backbone occurs during sliding.	120
Figure 54: ATR-IR results for three samples of PFA (1.5 mol.% PPVE). The Ratio of relative absorbance of CF ₂ and CF ₃ curves using area integration (b) and maximum peak values(c) for the bulk, wear debris, and running film show an increase in comonomer is present in the wear debris.	121

Figure 55: Effects of sliding on PFA microstructure and chemistry	125
Figure 56: Tribofilms of filled PFA samples tested in low and high relative humidity .	128
Figure 57: Friction coefficient vs. sliding distance. (left) unfilled PFA in dry nitrogen, 30% RH Air, and 45% RH Air. (Right) PFA-Al ₂ O ₃ (5 wt.%) in dry nitrogen, 30% RH, and 45 RH environments.	130
Figure 58: Volume lost vs. sliding distance. (left) unfilled PFA in dry nitrogen, 30% RH Air, and 45% RH Air over 508 m. (Right) PFA-Al ₂ O ₃ (5 wt.%) in dry nitrogen, 30% RH, and 45 RH environments over 25.4 km.	131
Figure 59: Volume lost vs. sliding distane. (left) unfilled PFA in dry nitrogen, 30% RH Air, and 45% RH Air over 508 m. (Right) PFA-Al ₂ O ₃ (5 wt.%) in dry nitrogen, 30% RH, and 45 RH environments over 25.4 km.	134
Figure 60: Tribofilms as a function of sliding distance and relative humidity	136
Figure 61: Attenuated Total Reflectance Infrared Spectra of PFA-Alumina bulk (untested) surfaces	137
Figure 62: Attenuated Total Reflectance Infrared Spectra of PFA-Alumina running films (tested surface).	138
Figure 63: Visual framework for the role humidity in reducing the wear of bulk PFA and the formation of tribofilms.	140
Figure 64: Summary of the tribochemical mechanism that promotes ultralow wear in fluoropolymer alumina composite materials.	141

Abstract

Fluoropolymers and fluoropolymer composite materials are commonly used solid lubricant materials. Over the past fifteen years, the addition of nanostructured alumina particles to polytetrafluoroethylene (PTFE) was shown to improve the wear rate of unfilled PTFE by nearly 10,000x. In this work, the hardnesses of both porous and dense micron sized metal-oxide particles (alumina and CoAl_2O_4) were independently measured using in-situ nanoindentation experiments that correlated directly with wear rate of the PTFE-metal-oxide composites. Framework for developing ultralow wear of PTFE-nanostructured alumina composites was extended to melt processable perfluoroalkoxy polymer (PFA)-nanostructured alumina composites. These composites also exhibited a nearly 10,000x improvement in wear rate compared to unfilled PFA through the development of robust tribofilms. Wear debris of unfilled PFA was found to have increased crystallinity compared to bulk unfilled PFA samples. Infrared spectra of the wear debris of unfilled PFA revealed the formation of new carboxylic acid endgroups which supports the hypothesis that shear stress during sliding causes chain scission of the PFA backbone. Wear of PFA - nanostructured alumina composites was determined to be 100x greater in dry nitrogen environments compared to humid lab air environments. Infrared spectroscopy revealed the formation of carboxylic salt groups on the surface of the PFA-alumina composites was minimal in samples tested in dry nitrogen compared to samples tested in humid laboratory air. The mechanism leading to the 10,000x improvement in wear rate of fluoropolymer-metal-oxide composites was attributed to the reaction of the broken fluoropolymer

backbone with environmental (O_2 and H_2O) with friable, metal-oxide fillers that reinforced the surface of the fluoropolymer without wearing away the countersurface material.

Chapter 1: Introduction to Tribology

1.1 Definition and importance of tribology

Tribology is defined as the study of friction, surface interactions and wear caused by two or more bodies in relative motion to one another. It was derived from the Greek word “tribo”, which means “to rub”, and was first coined by a group of British scientists, led by Peter Jost, in 1964 [1]. These scientists believed it was necessary to differentiate tribology from other fields within engineering and science [1]. Tribology plays a key role in many engineering applications such as lubrication for rotary motion typically found in engines, turbines, and pumps. Tribology is also critical in reciprocating sliding applications such as those found in gas compressors [2], [3]. Tribologists typically are trying to minimize frictional interaction, (with some key exceptions such as brakes), and minimize wear of the interacting surfaces. The financial value associated with reduced energy consumption and longer part lifetimes has been estimated to be worth 1.0-1.4% of a developed nations GDP.

A 2017 report titled “Tribology Opportunities For Enhancing America’s Energy Efficiency” to the Advanced Research Projects Agency-Energy, part of the Department of Energy, describes how the application of tribological innovations and technologies can greatly reduce energy consumption in the United States [4]. The report states that the US currently uses about 100 quads of energy per year ($1 \text{ quad} = 1 \times 10^{15} \text{ Btu} = 1.055 \times 10^{18} \text{ J} = 293 \text{ Billion kWh}$). US energy consumption can be broken into five primary sectors: Electricity Generation, Residential, Industrial, Commercial, and Transportation (Figure 1). The authors of the report identified the Transportation, Electricity Generation, and Industrial

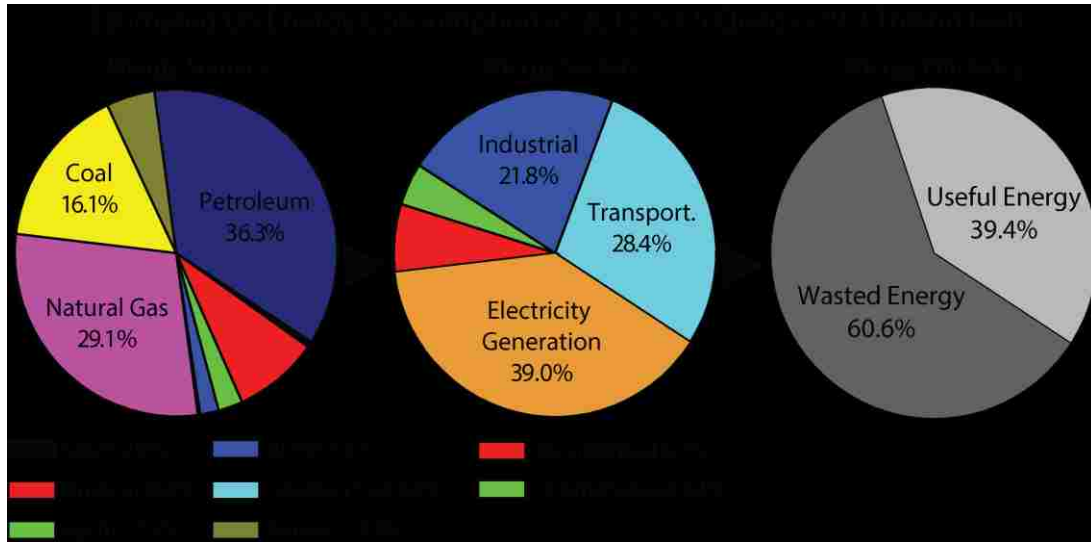


Figure 1: US energy consumption by energy source, sector, and overall efficiency [4].

sectors to have the greatest potential gain from tribological innovation. In passenger cars for example, frictional losses consume 33% of the total fuel energy used to propel the vehicle. Half of these frictional losses occur within the engine and transmission of the vehicle. Improvements in the design and materials of the piston assembly (“rotating assembly”), bearings, valve train, and pumps in passenger automobiles could lead to nearly 60% energy savings! In total, the report estimates that nearly 11% of energy consumed in the US each year (10.7 quads) could be saved through tribological research!

1.2 Solid Lubricants: Applications and Types

To reduce the energy consumed during operation, many engineering systems use lubrication. The purpose of a typical lubricant is to separate the surfaces in contact during operation, minimizing wear of the surfaces and the energy required during operation. However, there are many cases where lubricants and greases will not properly function or

are undesirable. One such application includes high purity manufacturing or chemical processes, common in the semiconductor, food, or oil and gas industries. In these cases, lubricants will cause contamination, which could lead to unsatisfactory performance of the final product. Many of these processes also take place in low vacuum environments, where such lubricants would simply vaporize and no longer act as a protective layer between the surfaces.

To address these conditions, tribologists have developed solid lubricants, which can be chemically inert and operate in a wide range of operating temperatures and environments. Solid lubricants can be classified into two categories, thin film coatings (molybdenum disulfide, graphite, diamond-like carbon coatings, and graphene are some of the more common coatings) and bulk solid lubricants (bronze, fluoropolymers (PTFE, PFA, FEP, TEFLON ®), ultra-high-molecular-weight polyethylene (UHMWPE), polyamideimide (PAI, Torlon®), polyetheretherketone (PEEK), and polyimides (PI, Vespel®, Meldin®). Though thin film coatings are often excellent solutions for tribological problems, they are beyond the scope of this dissertation. The author will only focus on bulk solid lubricants in this dissertation, specifically a class of materials known as fluoropolymers. Chemical makeup, microstructure, relevant physical and tribological properties of fluoropolymers will be presented in the proceeding sections after introducing tribology metrics.

1.3 The metrics of tribology: friction coefficient and wear rate

The designer of any engineering interface is concerned with the amount of frictional energy that is consumed during sliding. Tribologists quantify this consumed energy by

measuring the friction coefficient of the material system, first studied by Leonardo da Vinci between 1480-1518, then formally defined by French physicist Guillaume Amontons in 1699 [5]–[7]. The friction coefficient is defined as the ratio of the force resisting motion (the friction force) divided by the applied load normal to the interface (called the normal force). Typical contact geometries tribologists use to determine friction coefficient are shown in Figure 2.

It is important to note that friction coefficient is a system property, not simply a material property. The friction coefficient between two materials in contact may vary due to different contact pressure, sliding speed, true contact area, surface roughness, temperature of contact, and environment (like vacuum, air, or inert environments such as N_2). Tribologists try to replicate the sliding conditions (contact pressure, sliding velocity, environment temperature and composition) of their simplified tests to the desired application. This allows for tribologists to obtain a true, representative friction coefficient, for a more complex mechanical system like a journal bearing.

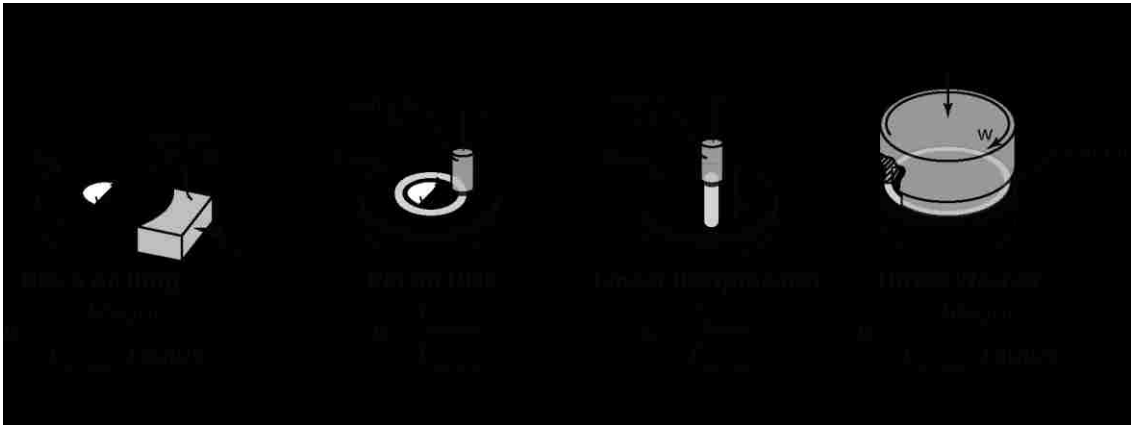


Figure 2: Common contact geometries of various tribometers.

The second metric tribologists are often concerned with is the system's wear rate. If the operating conditions of the material are known (normal force, sliding distance), the systems wear rate can be used to predict the lifetime of the component. By minimizing wear rate, lifetime will increase, which minimizes maintenance and reduces waste material. A common definition used to characterize wear rate of a system is known as Archard's Wear Law (Equation 1) [8].

$$\text{Equation 1: } K \left(\frac{\text{mm}^3}{\text{N}\cdot\text{m}} \right) = \frac{\text{Volume Lost}}{\text{Normal Force}\cdot\text{sliding distance}}$$

Archard and Hirst tested several samples across a range of material classes (metals, polymers, and ceramics) [8]. They found that under a wide range of pressures, nearly all the materials developed a linear relationship for volume of material removed for an applied load and sliding distance. Archard and Hirst then defined the ratio of the volume lost for a known load and sliding distance as the wear rate of the material. To illustrate how friction coefficient and wear rate can be used to predict frictional losses and lifetime of a tribological system, an example of a journal bearing will be presented.

1.4 Plain Journal Bearing Example

To illustrate the implications the improvement in wear performance allows, a simple lifetime prediction for dry plain journal bearings (also known as bushings) made of unfilled PTFE ($K \sim 5 \times 10^{-4} \text{ mm}^3/\text{Nm}$, $\mu \sim 0.12$), glass filled PTFE ($K \sim 5 \times 10^{-7} \text{ mm}^3/\text{Nm}$, $\mu \sim 0.3$), and $\alpha\text{-Al}_2\text{O}_3$ filled PTFE ($K \sim 4 \times 10^{-8} \text{ mm}^3/\text{Nm}$, $\mu \sim 0.23$) was completed (Figure 3). The journal bearing has a diameter of 25 mm, is 10 mm wide, is under a 150 N load, and the shaft inside of it is rotating at 100 rpm. Failure of the bearing is described as when 100 μm

of the bearing diameter is worn away, which causes unacceptable misalignment of the rotating shaft. The unfilled bearing would consume 2.4 W of frictional energy during operation and fail after 42 minutes, which is unacceptable. The glass-filled PTFE bushing would consume 5.9W of frictional energy and fail in a month. The ultralow wear PTFE- α alumina composite would consume 4.5W during sliding and would fail after slightly over a year of sliding! This reduces the amount of times the bearing would need to be replaced each year by over tenfold without a significant increase in frictional energy losses!

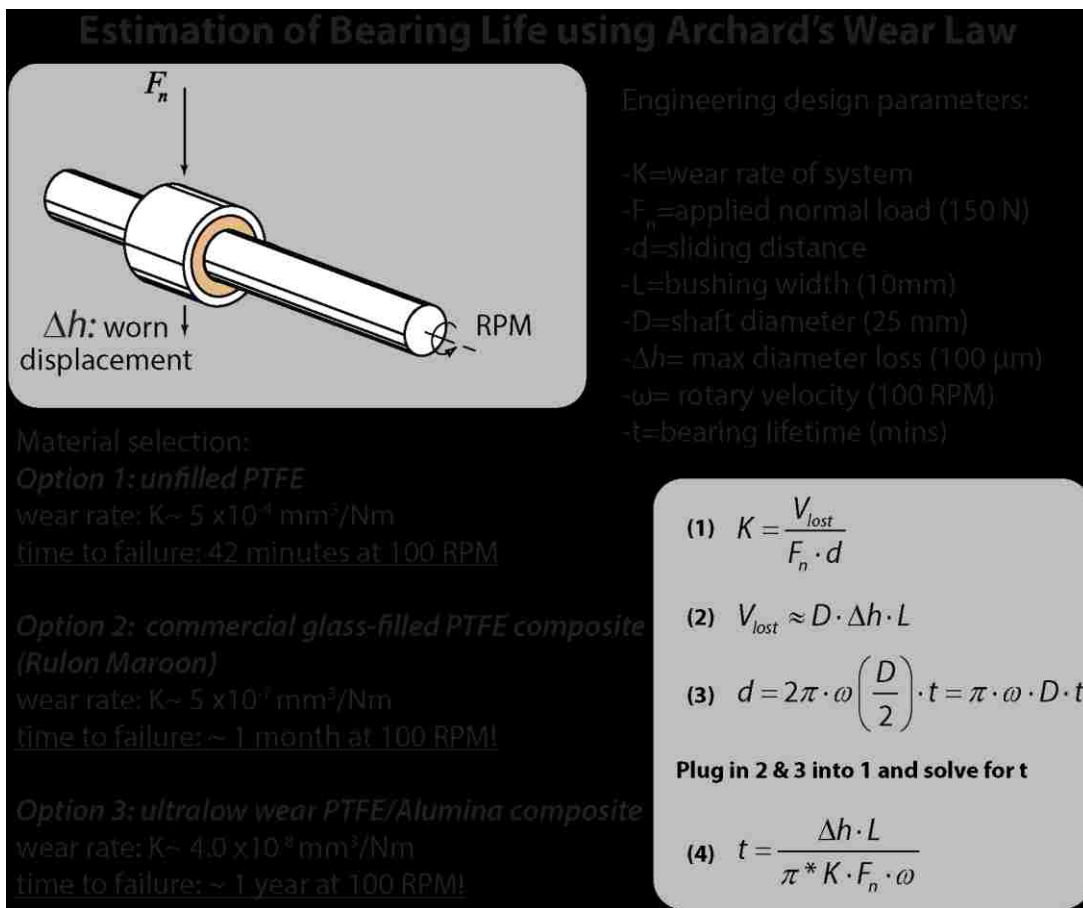


Figure 3: Example of journal bearing lifetime prediction using wear rates for PTFE, Rulon Maroon (PTFE and Glass Fibers), and ultralow wear PTFE/Alumina Composite

Chapter 2: Fluoropolymers and Fluoropolymer Composites in Tribology

2.1 Types and properties of fluoropolymers

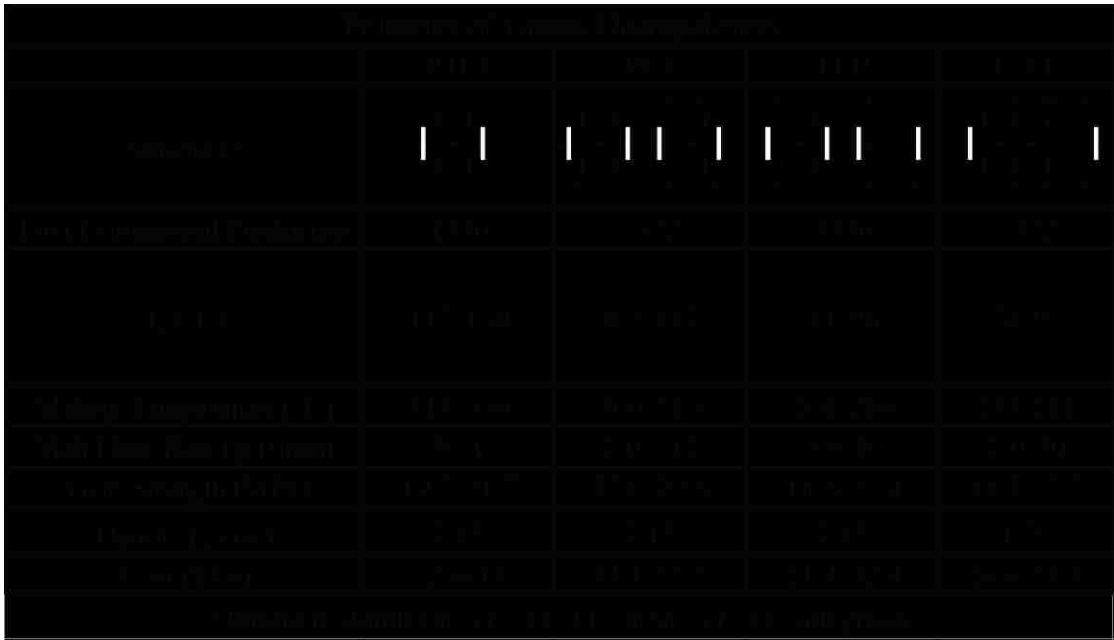
In 1938, the first bulk fluoropolymer, polytetrafluoroethylene (PTFE), was discovered accidentally by Roy Plunkett. PTFE was first commercially sold in the early 1950's by the DuPont Corporation under the brand name TEFLON® [9]. PTFE is extraordinary compared to many polymers, due to its high operating temperature, chemical stability in a multitude of environments, and its low coefficient of friction. PTFE is also very stable in vacuum environments. However, PTFE is limited by its incredibly high melt viscosity (near infinite) caused by its very high molecular weight (10^6 - 10^8 g/mol), which makes injection molding impossible [10]. In order to lower melt viscosity of PTFE, reduced molecular weight PTFE resins were developed but were inferior in repeated loading applications (fatigue) [10]. The reason for this drop in mechanical performance was due to the increased crystallinity within the microstructure of low molecular weight PTFE resins. To avoid this drawback, other fluoropolymers were developed to allow for reduced melt viscosity while improving fatigue resistance through decreased crystallinity.

The first melt processible fluoropolymer developed was fluoroethylene propylene (FEP), which was commercially released in 1960 [11]. FEP is a co-monomer of tetrafluoroethylene (TFE, $\text{CF}_2\text{-CF}_2$) and hexafluoropropylene ($\text{CF}_2\text{-CF-CF}_3$). FEP has an improved melt flow rate compared to most PTFE resins due to reduced molecular weight ($\sim 10^5$ g/mol), but has a corresponding drop-off in the maximum-operating temperature

(FEP~205 °C, PTFE ~288 °C) [11]. In the early 1970's two additional fluoropolymers were developed, perfluoroalkoxy polymer (PFA) and ethylene tetrafluoroethylene (ETFE) [11]. PFA is a copolymer of TFE and perfluoroalkyl vinyl ether (PAVE, $CF_2-CF-OR_f$), typically one to three carbons in length. PFA has superior mechanical properties to FEP and a higher operating temperature (260 °C), while still remaining melt processible [11]. ETFE, a copolymer of TFE and ethylene (CH_2-CH_2), was developed to enhance the mechanical properties of PTFE while expanding the operating temperature of polyethylene. Table 1 summarizes the properties of the aforementioned fluoropolymers.

Bulk fluoropolymers are used as electrical insulators (wire and cable housing) due to their high dielectric constants and are especially desirable at high operating temperatures. In addition, PFA and FEP tubing is used in many chemical processing plants due to its high

Table 1: Properties of Various Fluoropolymers

The table content is completely redacted with a solid black box. Only a few vertical white lines are visible, suggesting the presence of a grid structure with approximately 10 columns and 5 rows.

resistance to chemical and thermal degradation, allowing for production of high purity components. Avoiding contamination is especially important in the semi-conductor industry, which requires extreme purity to control electronic properties. Fluoropolymers are very desirable for tribological systems due to their low coefficient of friction. This low friction performance has been attributed to the unique microstructure fluoropolymers form during crystallization. The microstructure of PTFE and PFA, the two main fluoropolymers evaluated in this dissertation, will be described in the following section.

2.2 Microstructure of PTFE and PFA

When semi-crystalline polymers are synthesized or cooled from a molten state, most polymer molecules arrange themselves in a spherulitic structure (Figure 4) [12]. From the center of the spherulite, crystalline regions nucleate out and create lamellar or layered structures. Within these lamella, polymer chains neatly stack amongst themselves creating

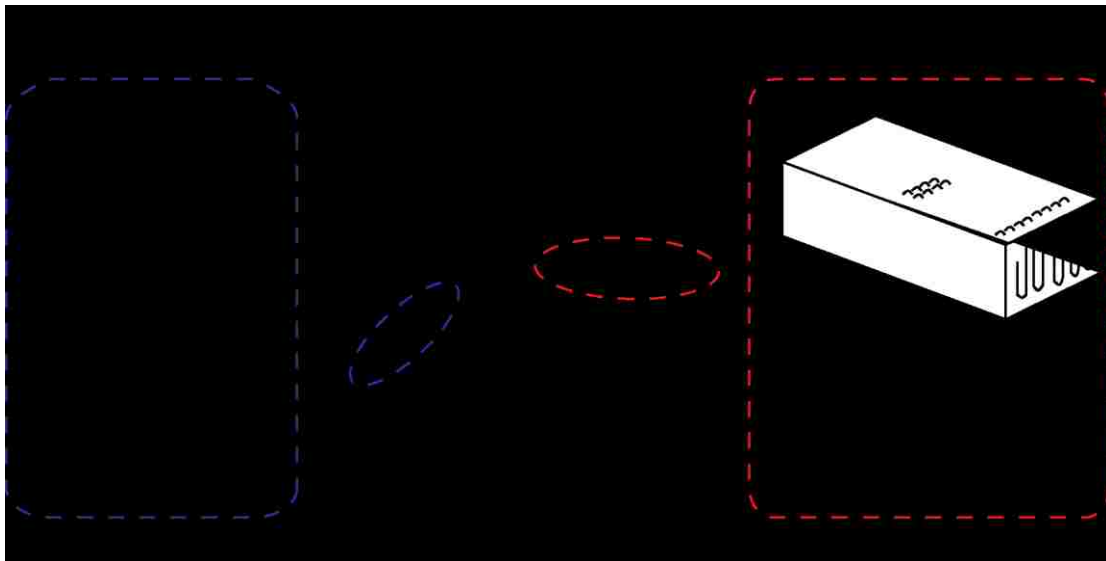


Figure 4: Spherulite schematic adopted from Sperling [12].

Table 2: Flexural Modulus and Flex Life (fatigue resistance) as a function of crystallinity for PTFE [10].

% Crystallinity	Specific Gravity	Flexural Modulus, psi	Flex Life (Cycles to Failure)
50	2.14	40,000	4×10^6
53	2.15	54,000	$1-4 \times 10^6$
75	2.22	150,000	6×10^4
85	2.25	170,000	1×10^3

a dense region within the spherulite. Polymer chains may leave the crystalline phase and reenter another crystal or the disordered region of the microstructure, commonly referred to as the amorphous region. Within the amorphous region, polymer chains are less likely to align themselves. Therefore, the amorphous region has significantly less density than the crystalline region. The ratio of the crystalline region to the amorphous region is defined as the percent crystallinity and is greatly affected by molecular weight (shorter chains crystallize easier), molecular structure (higher frequency and length of side chains within polymer prevent neat crystals from forming), and crystallization temperature (faster cooling reduces crystallinity). Crystallization can also be enhanced by applied stress during manufacturing processes such as drawing or extrusion. The percent crystallinity of polymers greatly affects their mechanical properties including stiffness, fracture, and fatigue properties (Table 2).

PTFE has a molecular weight that is an order of magnitude higher than most other commercial polymers ($>1 \times 10^8$ g/mol vs 3×10^4 - 1×10^6 for most commercial polymers). Due to its drastically high molecular weight, PTFE will not form spherulites under typical crystallization and molecular weight conditions. However, PTFE is still able to pack itself

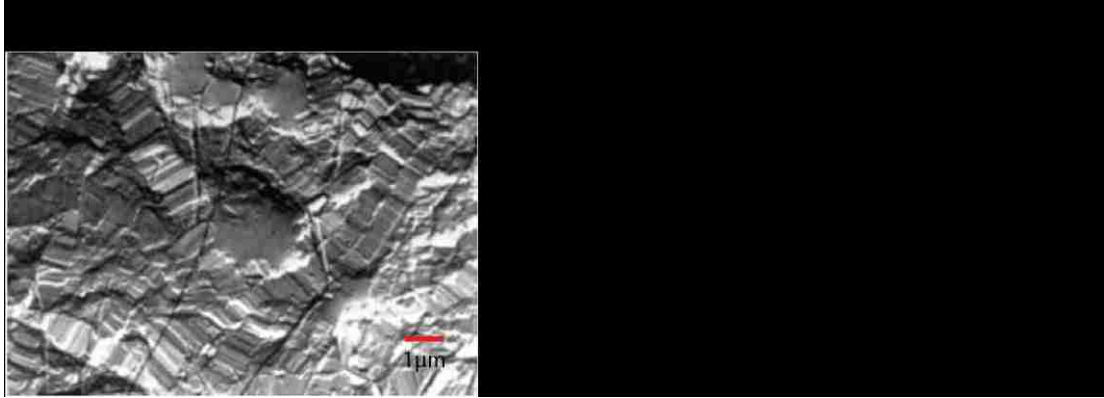


Figure 5: Visual description of PTFE microstructure. (a) SEM micrograph of replica of fractured PTFE surface [95]. (b) PTFE fiber arrangement of stacked crystalline and disordered regions. (c) Crystalline slice ~20 nm in thickness within PTFE fiber. (d) Spacing between the rigid polymer chains within the crystalline region [84].

into well-organized lamellar structures (Figure 5a) [13]. These lamellar regions are composed of thicker crystalline regions and very thin amorphous regions that separate them (Figure 5b). Rigid chains of PTFE stack upon one another into thin lamellar sheets within the crystalline region (Figure 5c-d).

The microstructure of PFA is similar in many respects to PTFE, however; there are some critical differences. The molecular weight of PFA is significantly lower than PTFE, which allows it to be melt processed. During cooling from the melt, PFA chains form crystallites that are also lamellar in structure similar to PTFE. In extreme cases at very slow cooling at elevated temperatures, PFA spherulites can form [13]. The addition of the PAVE comonomer lowers the linearity of the TFE backbone (**Error! Reference source not found.**) and prevents extended neat alignment of molecules known to exist in PTFE. This greatly reduces the crystallinity of PFA compared to PTFE with similar molecular weight. A schematic of the likely molecular structure of PFA is shown in Figure 6. As the

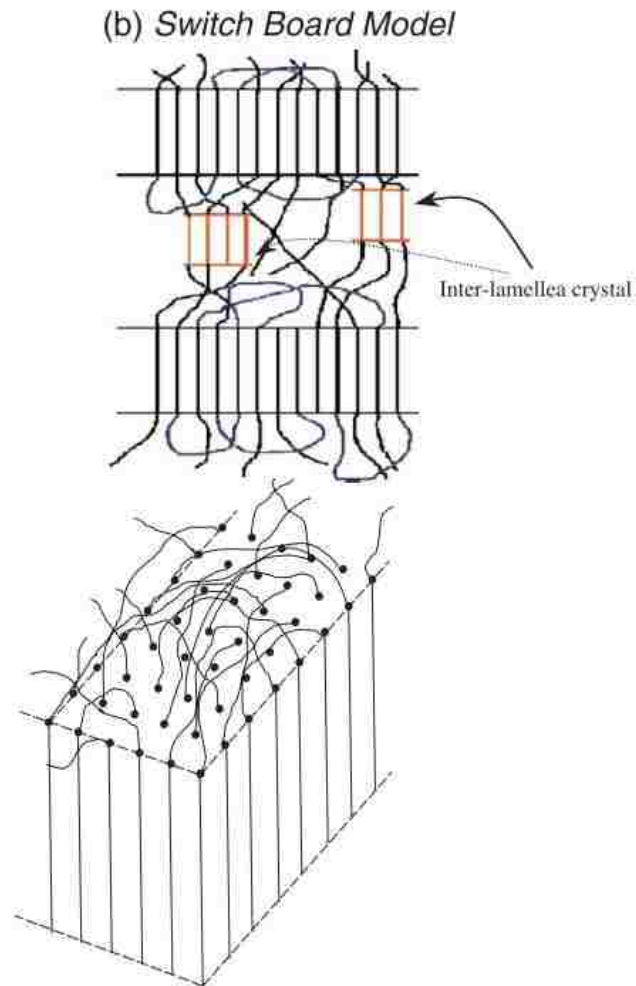


Figure 6: Switchboard model for semi-crystalline polymer likely formed by PFA. Reprinted with permission from [13].

proceeding section will show, the microstructure of PTFE, PFA, and their composites plays a very large role in their tribological behavior.

2.3 Tribological properties of unfilled and filled fluoropolymer composites

2.3.1 Unfilled PTFE

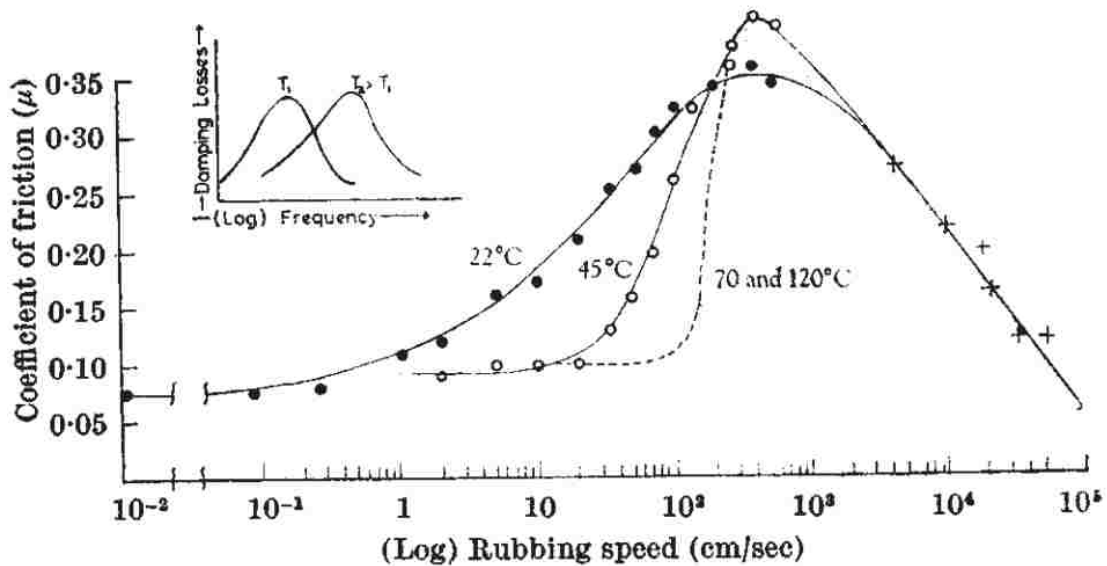


Figure 7: Friction of PTFE on PTFE (49% crystalline) as a function of sliding speed Reprinted with permission from [17].

Unfilled PTFE has exceptionally low friction coefficient against a variety of sliding surfaces (as low as 0.04) and has been used in dry journal bearings for over 50 years [14], [15]. Friction of unfilled PTFE is known to be a function of contact conditions (pressure, velocity, and sample temperature). For example, Biswas and Vijayan, show that with increasing contact pressure (0.14, 0.42 MPa) friction coefficient drops (0.35, 0.24) [16]. Friction coefficient was found to be dependent on sliding velocity and temperature by McLaren and Tabor with low friction (<0.15) occurring at slower sliding speeds (<70 mm/s) at room temperature (Figure 7) [17]. At elevated temperatures (45, 70, 120 °C), the friction coefficient remained low up to sliding velocities 1000 mm/s. This ability to maintain low friction at lower sliding velocity was attributed to ability of the polymer to

relax before the next application of stress (the frequency of applied stress is greater at higher sliding velocities).

Wear of PTFE was also found to be dependent on contact pressure, sliding velocity, and sample temperature by Tanaka & colleagues [18]–[20]. For similar sliding velocities, samples tested at higher temperature showed moderate increase in wear rates (2-3x higher) (Figure 8a) [19]. Samples tested at higher pressures exhibited increased wear rates of up to 10 times with a 5x increase in pressure (Figure 8b). Increased sliding velocity was shown to increase wear by nearly an order of magnitude for several levels of applied contact pressures (Figure 8b). Using an Arrhenius relationship, Tanaka et al. created a master curve that could account for linear wear rate of PTFE at any temperature, sliding velocity, and contact pressure:

$$\alpha = \frac{K_o(a_t v)(p/p_o)^n}{b_s}$$

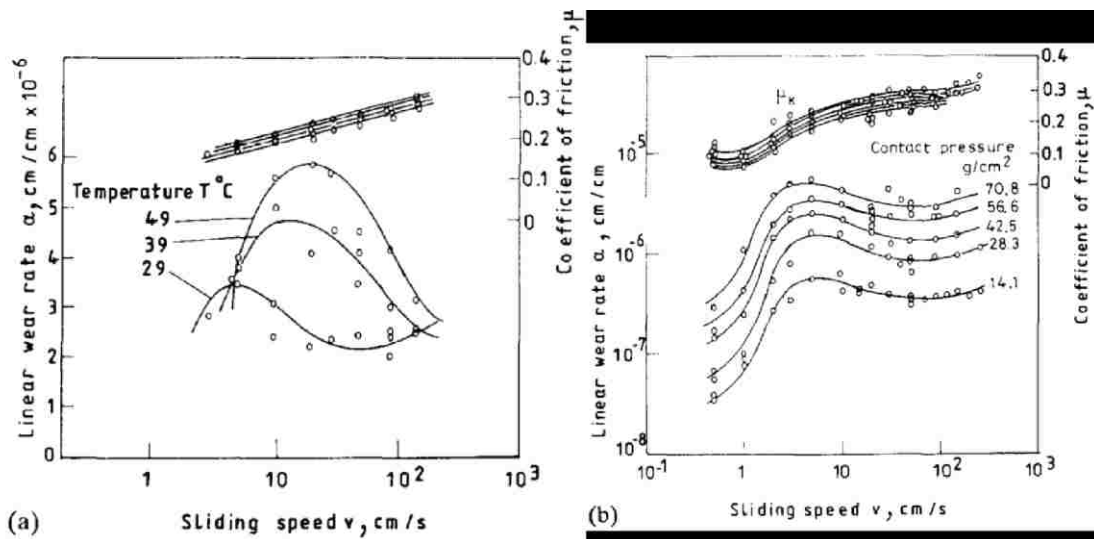


Figure 8: Effect of temperature (a) and pressure (b) on wear rate as a function of sliding speed. Reprinted with permission from [19].

where a_t and b_s are shift factors that vary with temperature, $n = 1.4$, $p_o = 28.3 \text{ kgf/cm}^2$ and $k_o(v)$ is the wear rate as a function of sliding velocity at a given temperature [19].

It is worth noting that PTFE exhibits wear rates that are 10-100x worse than many other bulk polymers [21], which has been attributed to its unique microstructure and extremely high crystallinity by multiple authors [16], [20], [22]. The microstructural arrangement of PTFE from the melt and the effects of sliding are summarized in (Figure 9). The banded lamellar microstructure of PTFE is originally in a random orientation after cooling from the molten phase (Figure 9b). After repeatedly being exposed to shear stress during sliding, the orientation of crystallites within the microstructure of PTFE are rearranged and form parallel to the sliding surface (Figure 9c, d). This rearrangement creates a “deck of cards” mechanism that sheds out large, flakey wear debris (Figure 9e, f) [16].

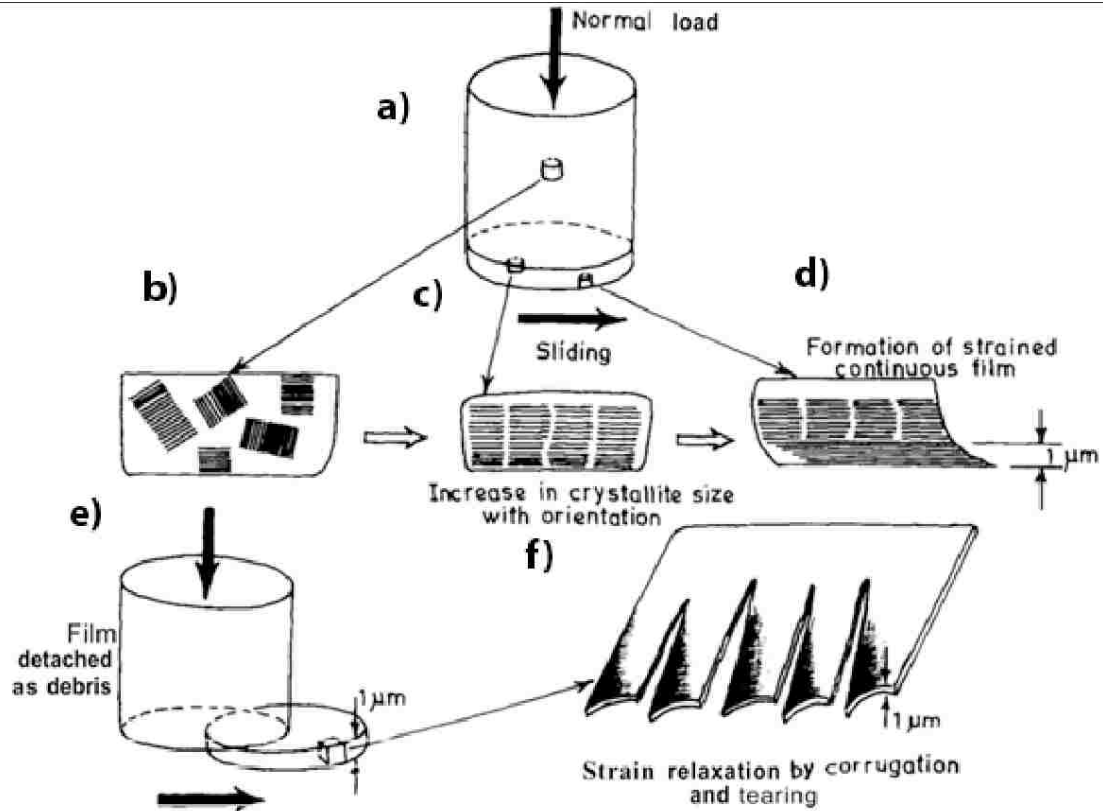


Figure 9: Wear debris formation of PTFE caused by shear during sliding. Reprinted with permission from [16].

Blanchet and Kennedy [23] summarized the friction coefficient and wear of PTFE using an Arrhenius relationship in a similar manner as Tanaka *et al.* [19]. Blanchet and Kennedy noted that at low values of friction coefficient, PTFE remained in its low wear regime and when high friction was recorded, high wear rates were also observed for a range of temperatures (23-66 °C) and sliding speeds (1 mm/s- 200mm/s). They correlated the mild and severe regimes of PTFE were a result of differences in shear stress due to kinetic friction coefficient (Figure 10).

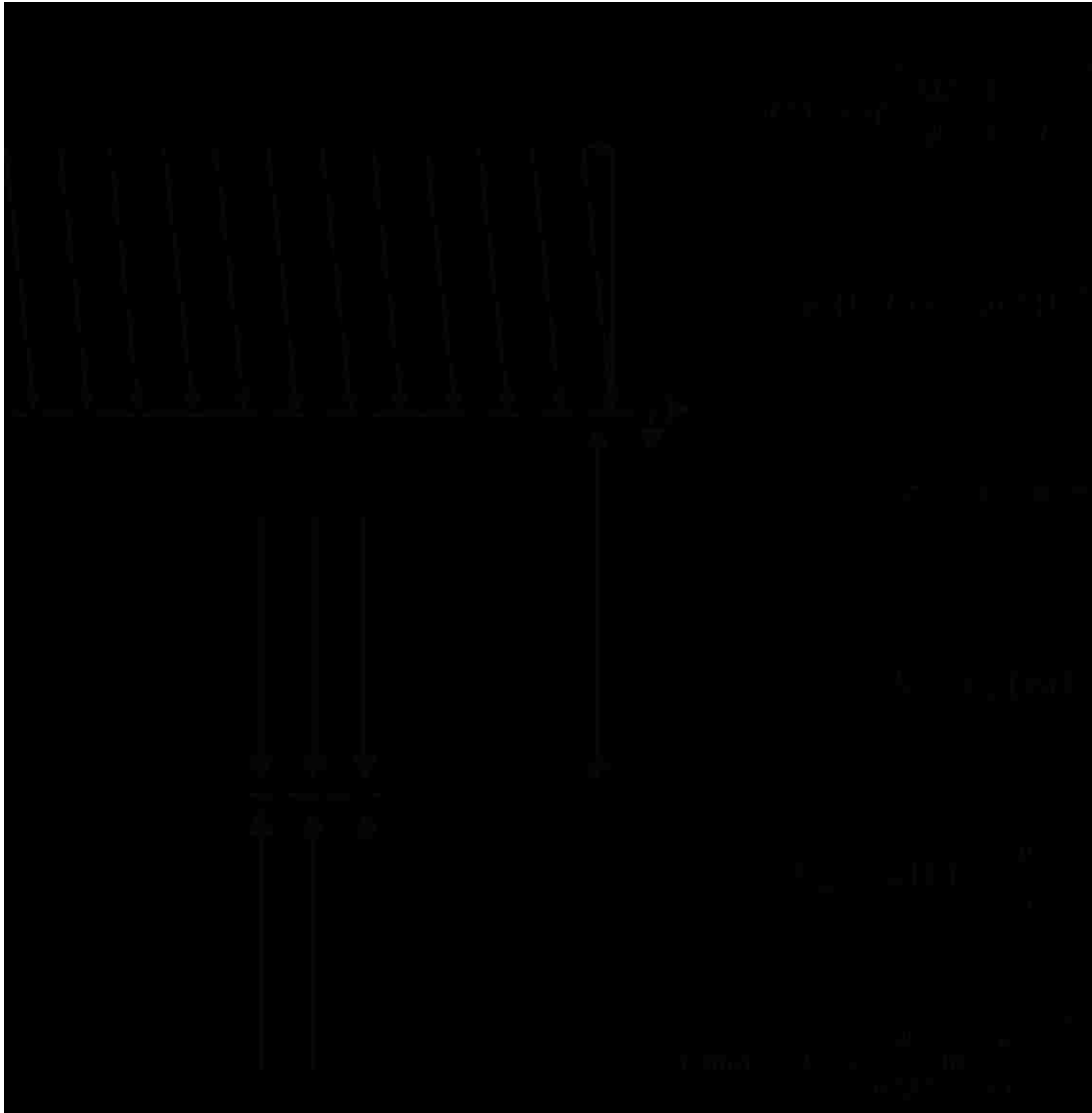


Figure 11: Mode-II fracture model for wear of unfilled PTFE. Maximum allowable sliding velocity and minimum temperature for mild wear of PTFE are defined in equations 5&6 respectively. Reprinted with permission from [23].

2.3.2 Overview of PTFE composites for tribological applications

PTFE with reinforcing fillers (carbon fibers, glass fibers, bronze particles, and mineral fillers (oxides, carbides etc.)) has been an important segment of tribology research for over fifty years. To counteract the severe wear condition of PTFE at higher speeds and pressures, an assortment of filler materials (carbon fibers, glass fibers, MoS₂, ZnO, carbon nanotubes, lead oxides, etc.) have been added to PTFE [18], [19], [23]–[35]. Most fillers serve to moderately reduce wear (by one or two orders of magnitude) with an acceptable trade-off in higher frictional losses. In general, reinforcing fillers are desirable because they are inexpensive especially compared to some high-end thermoplastics, such as PEEK. In addition, most reinforcing fillers can be mixed into PTFE powders quite easily and can withstand the high sintering temperature of PTFE (380 °C) without thermal degradation. In the proceeding paragraphs, some influential studies done on the tribological behavior of PTFE with reinforcing fillers will be highlighted.

One of the preliminary works on PTFE composites was written by J.K Lancaster in the late 1960's and early 1970's [36], [37]. Lancaster compared the wear of PTFE composites with various fillers (mica, asbestos, MoS₂, carbon fiber, and graphite) and the wear of the metallic counterface each composite slid against. Lancaster was particularly interested in how the filler affected the roughness of the counterface. Lancaster describes that two processes typically dominated countersurface roughness: transfer film development and countersurface abrasion. Transfer films are thin polymer layers that form on top of the typically metallic counterface. These films are usually formed by the ejected wear debris bonding to the counterface. Lancaster observed that if the transfer film

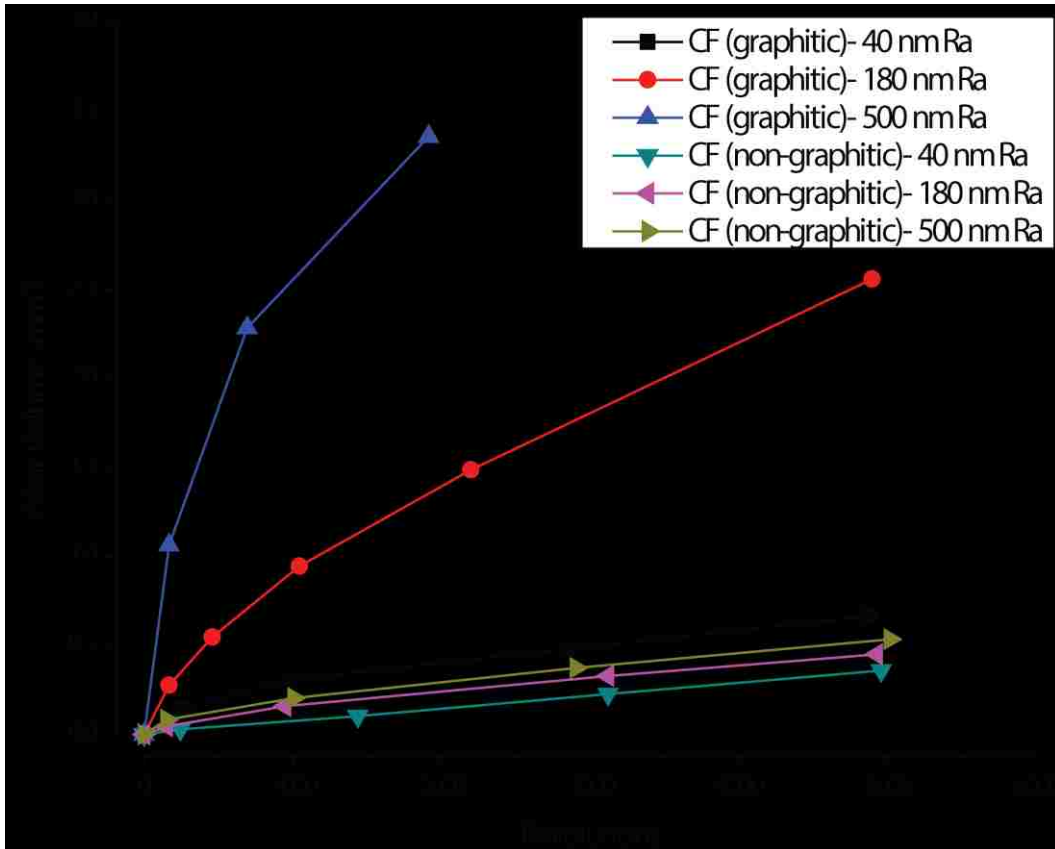


Figure 12: Wear volume versus number of revolutions of PTFE-carbon fiber composites against mild steel of increasing roughness measured by center line average roughness (Ra) (graphitic-non-abrasive, non-graphitic-abrasive) [37].

increases the countersurface's roughness, the transfer film will promote higher wear and if the transfer film decreases the counterface's roughness, a reduced wear will be observed. The second factor in promoting low wear is abrasion of the counterface caused by the fillers particles/fibers. Too hard/large sized fillers cause deep scratches and increase the counterfaces's roughness, which lead to micro-cutting of the polymer composites. Smaller, softer additive particles lead to decreased roughness of the counterface, as the polymer interface goes from a micro cutting to fatigue failure mode [37].

Lancaster showed a counterintuitive example of these wear modes by filling PTFE with two types of carbon fibers. The first type of carbon fiber was heat treated to be graphitic in nature (graphite is a solid lubricant, and easily shears under applied load) and the second type was non-graphitic (stronger resistance to shear) and abrasive in nature. Graphitic carbon fibers showed a decrease in wear performance even though the graphitic fibers promoted formation of a polymeric transfer film on the steel counterface. The transfer film increased the roughness of the counterface and promoted the high wear regime. Non-graphitic carbon fibers abraded the steel counter face and no transfer film was formed. However, this abrasion reduced the counterface's roughness and led to a consistently low wear over a range of initial countersurface roughnesses (Figure 12).

In 1977, Arckles, Theberge, and Schireson [38] investigated wear of PTFE composited with glass fibers (15 % by weight) [38]. PTFE was also composited with Poly oxy-benzoate (POB, 10, 15 wt. %), polyphenylene sulfide (PPS, 20, 40 wt. %), and a composite of PTFE with PPS, graphite, and MoS₂ (30, 50 wt. % filler) for tribological testing. POB and PPS are both high temperature polymers with high friction coefficients (POB~0.37, PPS~ 0.7) and superior mechanical properties (higher stiffness and tensile strength compared to PTFE). Tests were performed on thrust-washer bearings at high velocities (7.62 m/s) and 0.25 MPa of contact pressure. In addition to measuring the wear of the composite samples, Arckles *et al.* also investigated the wear of the steel countersurface (mg/hr).

Results of the tests showed improved wear of nearly 1,000 times for all the samples tested compared to the PTFE control. Observed wear of the steel countersurface was the

main difference between the composites tested. The wear of the steel counterface slid against the PTFE- glass fiber composite was thirty times greater than the wear of the steel against unfilled PTFE (0.030 mg/hr vs 0.001 mg/hr). Composites made with the soft polymer fillers only increased wear of the metal countersurface two to three times (0.002-0.003 mg/hr). In the discussion, Arkles *et al.* accentuates that fillers must have stronger mechanical properties than PTFE and cannot be lamellar structured, such as graphite and MoS₂. These materials are unable to support the load of the already weak PTFE structure due to their poor shear strengths. Arkles *et al.* conclude that hard, inorganic fillers improve the wear of the polymer at the expense of the metal countersurface. Softer fillers must be used as an alternate and delivered similar wear performance without damaging the

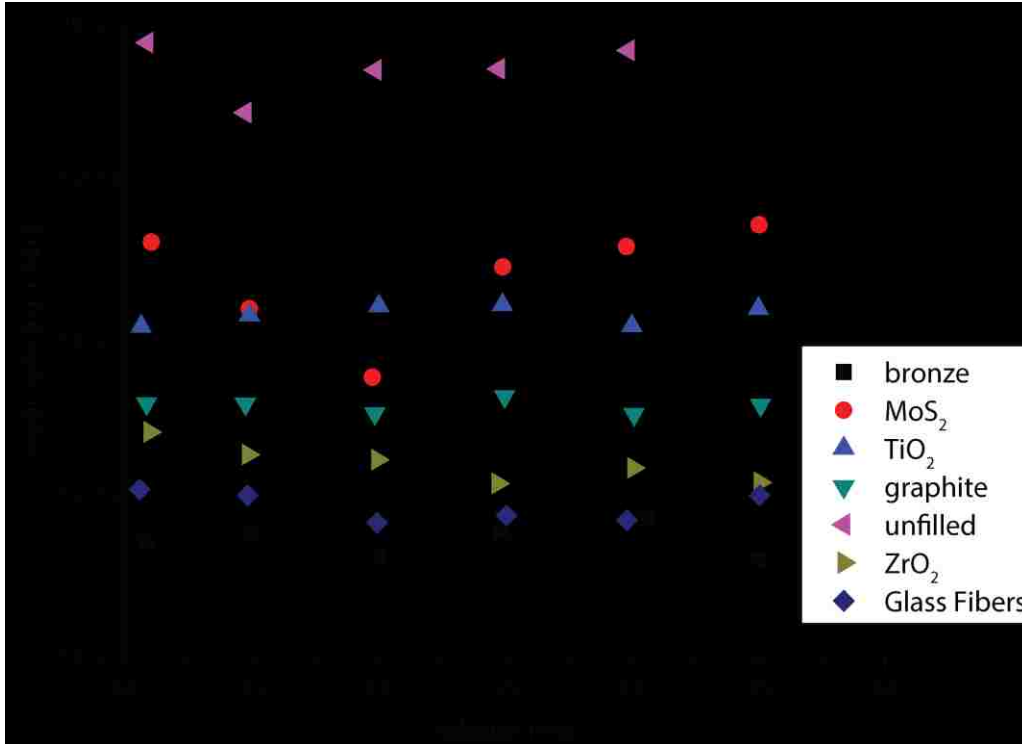


Figure 13: Wear rate of PTFE composited with a variety of fillers as a function of sliding velocity at 10 N load [18].

counterface [38].

An additional study on the role of filler properties on wear and frictional performance of PTFE composites was completed by Tanaka and Kawakami in 1982 [18]. They investigated PTFE with glass fibers (25 wt. %, 7 μm \O , 100 μm long), bronze (40 wt. %, several microns in size), ZrO₂ (40 wt. %, <45 μm), TiO₂ (20 wt. %, <45 μm agglomerates of particles <0.3 μm in size), MoS₂ (20 wt. %, several microns in size), and graphite (15 wt. %, several microns in size). All samples were cut into 3 mm diameter cylinder flats for testing against mild steel discs. For nearly all the fillers tested, higher wear and friction coefficient were observed initially before transitioning into a lower wear

and friction coefficient regime. Sliding velocity and load had little effect on friction coefficient and most of the samples tested exhibited friction coefficient values very close to unfilled PTFE ($\mu \sim 0.2$). Friction performance was found to be independent of filler particle type ($\mu \sim 0.2-0.3$) except for ZrO_2 filled PTFE ($\mu \sim 0.6$) due to its large particle size ($40 \mu m$). Most fillers improved the wear rate of PTFE by one to three orders of magnitude and exhibited lower wear rates when tested under lower applied forces (10 N vs 50N) (Figure 13). Abrasion of the counter surface was observed for PTFE composites with glass fibers, bronze and ZrO_2 and was not observed for TiO_2 , MoS_2 , and graphite fillers. Larger wear debris were observed for smaller fillers (MoS_2 & TiO_2) compared to the wear debris of larger fillers (bronze, ZrO_2 , and glass fibers).

Tanaka and Kawakami suggest a model of preferential load support to explain the improved wear performance of the composite materials. The theory suggests that long fibers will preferentially carry the load over the PTFE matrix, shielding it from potential damage. They generalized this relationship with the following equation:

$$\sigma_f = 2 \left(\frac{l}{r} \right) \tau + \sigma'_m$$

where σ_f is the stress of the fiber, σ'_m is the compressive stress on the polymer matrix within the composite, τ is the shear strength of the polymer matrix, and l/r is the aspect ratio of the filler particle. If the aspect ratio is greater than unity, stress on the fiber ($l/r > 1$) is increased significantly. Spherical particles such as ZrO_2 or bronze have aspect ratios near unity and can also preferentially support the load. Platelet-like particles such as MoS_2 and graphite have an aspect ratio nearly equal to zero, which means the particles carry the same

stress as the polymer matrix. Tanaka and Kawakami stress that too fine particles cannot prevent destruction of the PTFE's banded, lamellar structure and leads to higher wear (MoS₂, TiO₂, and to a lesser extent graphite). Larger particles prevent the rearrangement of PTFE's microstructure though preferential load support. The benefits of a larger harder particle are limited as exhibited by ZrO₂, which increased the abrasion of the steel interface and increased friction ($\mu \sim 0.6$) of the composite as well. Authors suggest that filler type is relatively unimportant if particles are between 3 μm and 30 μm .

In conclusion, several hypotheses have been developed to account for the improved properties of PTFE composites. Two principal mechanisms claimed are preferential load support [18], [34], where the stress on the PTFE matrix is partially carried by the filler particles, and arresting crack propagation [23], [28], where filler particles prevent the growth of cracks and prevent large scale delamination of PTFE sheets. An additional theory suggests the formation of a robust, thin transfer film adheres to the countersurface and prevents abrasion of the PTFE composite [29], [31], [32]. This theory will be discussed in more detail in the following section.

2.3.3 Overview of ultralow wear PTFE α -alumina composites

Though the addition of hard inorganic filler particles/fibers to PTFE improves performance significantly, they can lead to abrasion of the metal countersurface, which is also undesirable. A new class of PTFE composited with certain Al₂O₃ filler particles, called ultralow wear PTFE- α alumina, reports wear rates that are four orders of magnitude less than unfilled PTFE [25], [39]–[43]. The worn surfaces of this tribosystem are characterized

by brown films that develop on the surface of the polymer composite (running film), and the surface of the countersample (transfer film). Many theories have been presented that highlight the role of these tribofilms in this unprecedented wear reduction and this section will serve as a brief summary on ultralow wear PTFE-alumina systems [41]–[47].

The initial work on ultralow wear PTFE was by Burris and Sawyer in 2006 [39]. In this investigation, PTFE was reinforced with ZnO (50 nm) and Al₂O₃ nanoparticles (38, 44, and 80 nm). The authors tested the composites against 304L SS at 6.25 MPa and 50.8 mm/s. PTFE with 80 nm Al₂O₃ nanoparticles exhibited the lowest wear rate of all the composites by over an order of magnitude. In all cases, an increase in the amount of filler particles lead to a decrease in the amount of run-in (distance required to reach steady-state wear, i.e lowest wear rate) but once reaching steady state, all the wear rate values were very close for all filler percentages (1, 2, 5 and 10 wt. %). It was hypothesized that this run-in behavior ceases once a large percentage of filler particles consolidates at the sliding interface. Friction of the well performing composites was significantly higher than unfilled PTFE ($\mu \sim 0.12$) and ranged from 0.22- 0.30. The authors attributed the order of magnitude improvement in wear of the 80 nm composites compared to other PTFE composites tested showed that the increased particle size and agglomeration of the 80 nm Al₂O₃ particles

100k and 1M cycles

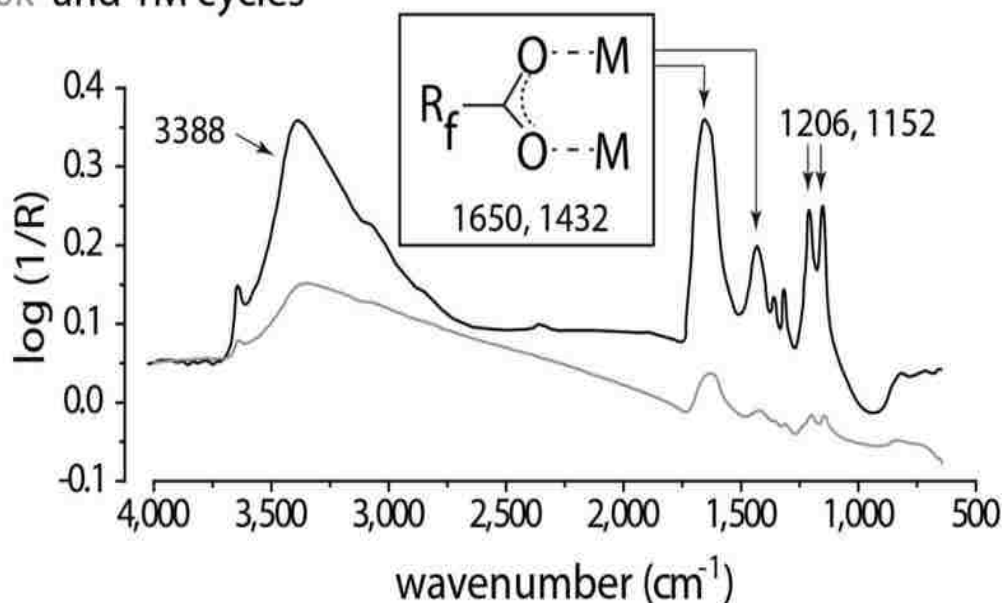


Figure 14: FTIR spectra of transfer film. Peaks corresponding to carboxylate salts (1650 cm^{-1} , 1432 cm^{-1}), waters of hydration (3388 cm^{-1}), and CF_2 from PTFE backbone (1152 cm^{-1} , 1206 cm^{-1}). Reprinted with permission from [48].

allowed them to significantly outperform the smaller Al_2O_3 and ZnO particles, since they could better prevent delamination wear of PTFE's lamellar microstructure.

In a follow-up study, Harris *et al.* investigated the chemical composition of the running film and transfer film of the PTFE- α Al_2O_3 composite system [48]. Infrared spectroscopy was used to determine the chemical composition of the transfer film developed on stainless steel counterface during sliding at the same contact and sliding conditions as Burriss and Sawyer [39]. The one experimental difference Harris *et al.* employed was they used a "stripe test" instead of a single stroke length during the duration of the experiment. To perform a stripe test, the length of the sliding stroke is modified with increasing sliding distance to evaluate how the transfer film evolved during sliding. In this study the sliding

stroke was modified after 1, 10, 100, 1k, 10k, 100k, and 1M cycles. Reflectance FTIR was performed on each area to analyze evolution of the composition of the transfer films. The authors found that at the higher sliding distances, corresponding to 100k and 1 million cycles, FTIR spectra showed carboxylate salt groups as well as CF₂ groups on the metallic counterface (Figure 14). Harris *et al.* provided a mechanism for the development of the carboxylic salt groups. The first step of this process consists of chain scission of the PTFE backbone, which results in perfluoroalkyl free radicals at the separation sites. These free radicals bond with oxygen and decompose to form acyl fluoride endgroups. These acyl fluoride groups bond with water to form carboxylate acids, which chelate to the metallic surface of the countersample and to the surface of the alumina particles concentrated at the surface of the PTFE composite (**Error! Reference source not found.**). This hypothesis is supported by previous studies that highlight higher wear in vacuum and dry nitrogen environments as well as increased hardness of the PTFE-Al₂O₃ surface after sliding [44], [49], [50].

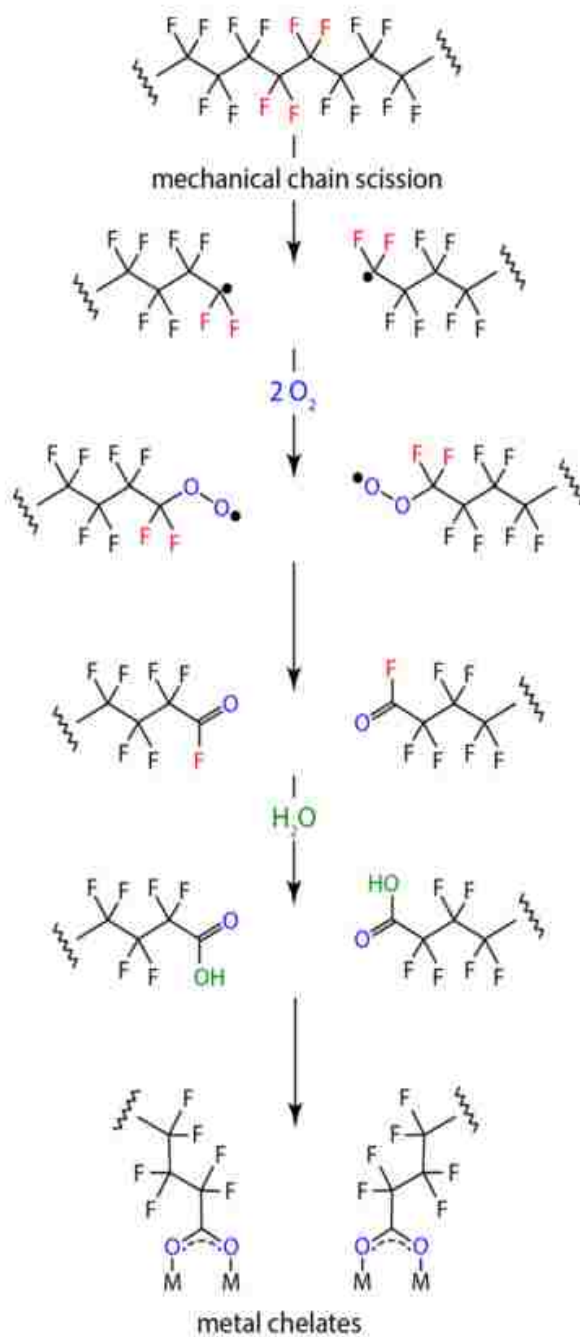


Figure 15: Mechanically driven chain reaction of PTFE- Al_2O_3 composite forming carboxylic acid endgroups which bond to active sites on the metal counterface and alumina particles. Reprinted with permission from [48].

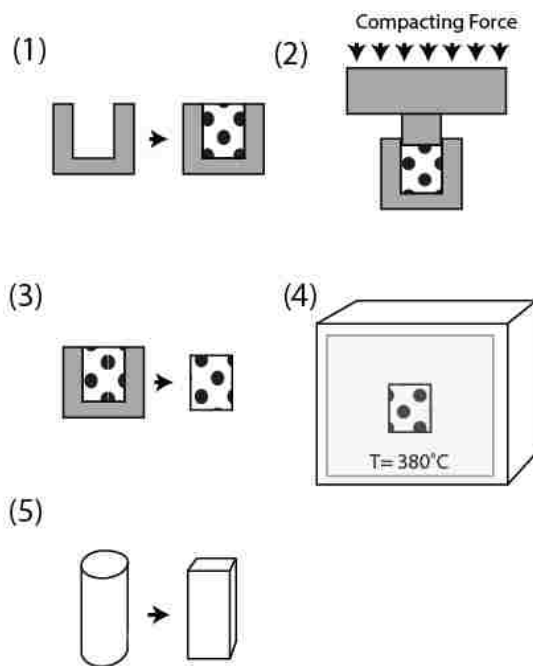
The importance of transfer film development in creating ultra-low wear PTFE-Alumina systems was reviewed by Ye *et al.* in 2016 [51]. The authors provided historical context, that since transfer films are often very thin ($<10\ \mu\text{m}$, sometimes $<1\ \mu\text{m}$), tribologists often struggled to quantitatively characterize the properties of these films. An inverse trend between wear rate and transfer film thickness was found for PTFE composite materials. Composites achieving ultra-low wear (wear rates $< 5 \times 10^{-7}\ \text{mm}^3/\text{Nm}$) were found to have transfer film thicknesses of less than $1\ \mu\text{m}$ [52]. The wear rate of ultra-low wear PTFE composites was found to correlate with the average size of the uncovered region (bare metal) of the countersample. As these regions reduced in size during the initial stages of wear, the wear rate of the PTFE-composite system reduced from greater than $1 \times 10^{-4}\ \text{mm}^3/\text{Nm}$ to less than $5 \times 10^{-7}\ \text{mm}^3/\text{nm}$. Additional testing evaluated the hardness [53], adhesion [54], and wear properties [54] of the transfer films of ultralow wear PTFE-alumina systems. Increased hardness of these transfer films was found to correlate directly with improved wear resistance [53]. Both the adhesion strength and wear resistance of the transfer film was found to increase with increased sliding distance [54].

Wear and friction studies on PFA have been very few and far between [55], [56], especially compared to PTFE and PTFE composites, which have been thoroughly studied. Previous studies on PFA and PFA composites have shown that PFA has increased frictional losses (0.15 vs 0.07) and a slight reduction in wear compared to PTFE (four times less than PTFE). One of the primary objectives of this study is to determine which aspects of the PFA and PTFE composite systems are the same and which aspects are different, and how do these changes affect the tribological properties of the system.

Chapter 3: Motivation and Research Hypothesis

PTFE α -alumina composites have exceptionally low wear rates ($\sim 10,000\times$ lower than unfilled PTFE). A major barrier to the commercial success of these composites is the time intensive cold press and sintering process (Figure 16a). This process requires proper dispersion of alumina into the PTFE granular resin and then the powder mixture must be pressed into a relatively simple shape (tube, disc, or rod). The “green” part then is sintered above its melting temperature to allow the particles to coalesce. The part is then removed and machined into its final geometry. This process can lead to excessive material waste due to machining and is undesirable for large quantities of parts.

a) Compression molding and sintering



b) Injection molding

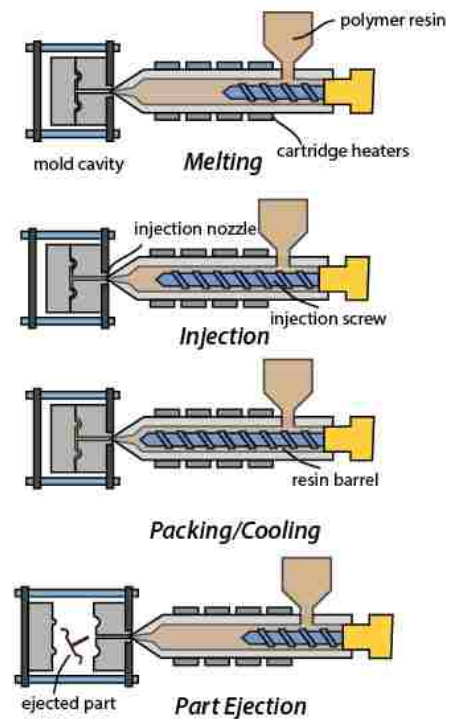


Figure 16: (a) Cold press and sintering process for PTFE- Al_2O_3 composites. (right) Screw injection molding process for PFA- Al_2O_3 composites.

PFA- α alumina composites could be an ideal alternative to PTFE- α alumina composites because PFA's lower melt viscosity allows it to be injection molded. PFA maintains many of PTFE's desirable properties such as high operating temperature, high chemical stability, and dielectric properties with a slightly increase in frictional losses. The injection molding process, described in Figure 16b, creates complex geometries rapidly with minimal post-machining required. This minimizes the number of total manufacturing steps and the amount of material wasted. Additionally, PFA and α -alumina particles can be melt mixed using a compounder and pelletized, which avoids the time-consuming alcohol dispersion technique used in PTFE- α alumina composites. PFA- α -alumina pellets could be sold directly to companies which could then injection mold the PFA- α alumina parts themselves. To evaluate the behavior of PFA α -alumina composites, tribological testing and material characterization methods will be used to compare PTFE and PFA alumina composites.

In the following chapters, the author will look at the following aspects of the tribological behavior of the fluoropolymer (PFA) metal-oxide system:

Chapter 5: Nano mechanics of Metal-Oxide Filler Particles lead to Ultralow Wear Fluoropolymers. *Hypothesis: Porous alumina and metal oxide particles will lead to lower wear and less abrasion of the counterface, compared to dense metal-oxide particles of similar size distribution.*

Chapter 6: Ultralow Wear Melt Processible Fluoropolymer Alumina Composites. *Hypothesis: Melt processable PFA-metal oxide composites will exhibit similar ultralow wear mechanism as PTFE metal-oxide composites.*

Chapter 7: Effect of Sliding on the Microstructure and Tribochemistry of Unfilled PFA.
Hypothesis: Increased in the crystallinity of wear debris and chain scission of the polymer backbone of PFA will occur during sliding experiments.

Chapter 8: Environmental effects on tribological performance of PFA and PFA alumina composites. *Hypothesis: Wear of PFA-alumina composites will be ten to one-hundred times higher in dry nitrogen due to the lack of tribofilm development.*

Chapter 9 incorporates the findings of each chapter into a singular mechanism that describes the wear of fluoropolymer metal-oxide systems.

Chapter 4: Materials and Methods

4.1 Material Synthesis Procedures

4.1.1 PTFE and PTFE-Metal Oxide Composite Synthesis Procedure

All PTFE composites used Chemours PTFE 7C grade resin which has an average particle size of $\sim 30\mu\text{m}$. For PTFE- metal oxide composites, PTFE resin was mixed with 5 wt. % of the metal oxide particles. Once the PTFE resin and filler particles were mixed, they were submerged in isopropanol and mixed using a sonicating horn (Branson SFX 450) for 5 mins with a duty cycle of 50%. These samples were then allowed to dry for 1 week in laboratory air.

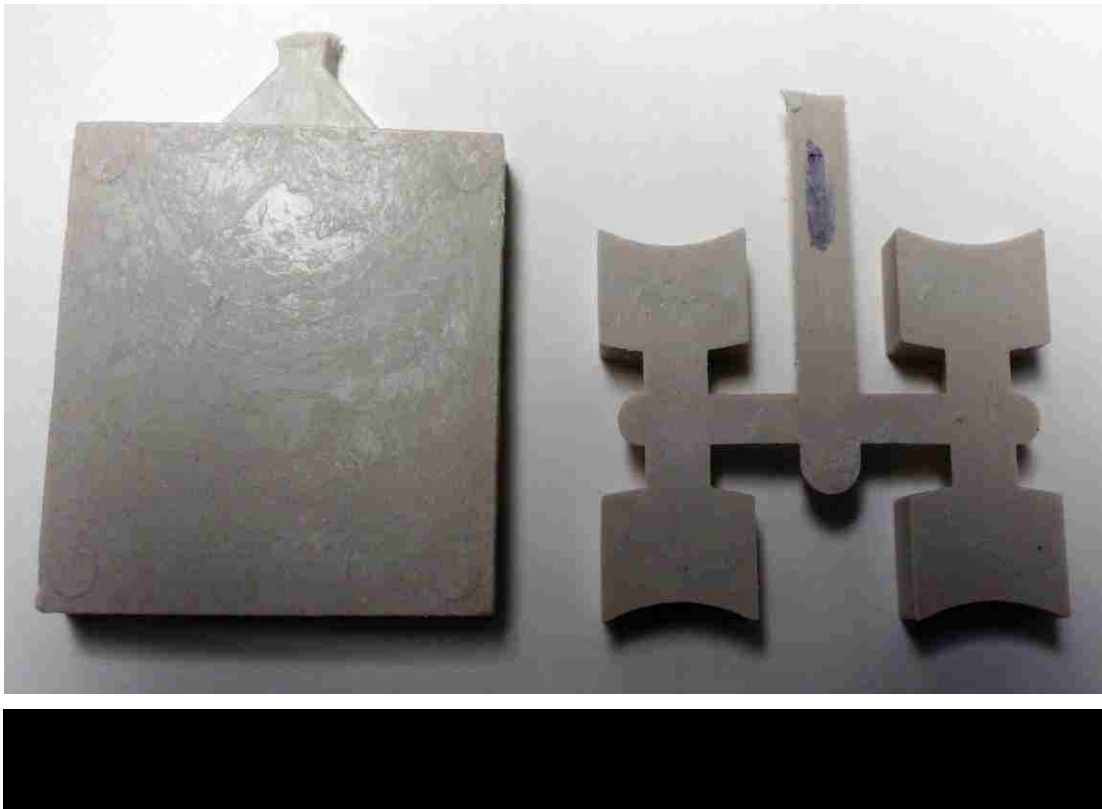
The dried PTFE-particulate mixtures were compressed into a nominally 1.5” tall by 0.5” diameter cylinder using a hydraulic press at ~ 75 MPa of pressure to achieve a dense part. These samples were then sintered using the following temperature profile: heat polymer samples up to 380°C at a rate of 120°C/hr ($T_{\text{melt}}=328^\circ\text{C}$ for PTFE). After reaching 380°C , the samples were held at this temperature for three hours and then were cooled down to room temperature at a rate of 120°C/hr . This process ensures that the PTFE resin particles have enough time above the melt temperature to coalesce and form strong interparticular bonds. The samples were then machined using an end mill into their final geometry for testing (6.3mm x 6.3mm x 12.7mm rectangular prism). Samples were then ground using 800 grit SiC paper ($R_a\sim 100$ nm), then sonicated in methanol for thirty minutes to remove any surface contamination. These samples were then dried for a minimum of four hours in laboratory air before testing began. All samples were tested against 304L

stainless steel countersamples that were prepared to have a random roughness orientation using a lapping process. These samples were washed with soap and water then rinsed in methanol at least thirty minutes before testing began.

4.1.2 PFA Synthesis Procedure

Three grades of Chemours Teflon® PFA (340, 345, and 440) were chosen as the PFA resin used in the study. All the grades of PFA tested have the same comonomer (perfluoropropyl vinyl ether). The samples were prepared using a ZSK 18mm co-rotating twin screw mega compounder which has a typical screw design for dispersion of inorganics in fluorinated materials. The alumina particles were dried for eight hours at 100 °C before compounding with the PFA resin. The compounded mixture was extruded, quenched, and pelletized. The pellets were dried and then injection molded into two geometries, a simple plaque and more complex BOR sample (Figure 17). The injection molding machine was a Boy Machines 22 AV single screw vertical barrel, vertical platen injection molding machine. The molds were kept at 285°C and slowly cooled for approximately forty seconds before the part was ejected. The α -alumina particles were purchased from Nanostructured & Amorphous Materials, Inc. (Houston TX, Stock # 1015WW). These particles are micron sized porous agglomerates that were found by static light scattering to have an average diameter of 3.95 μm . The surface area of the particles was determined to be 41.4 m^2/g using BET.

The plaques of unfilled PFA and PFA alumina were cut into 6.3 mm x 6.3 mm x 12.7 mm samples for wear testing. The surface to be tested was wet ground using 800 grit SiC sandpaper on a grinding wheel to a surface finish of $R_a \sim 100$ nm. The test samples were then placed in a methanol bath and sonicated for thirty minutes to remove any potential contaminants from the surface that may have been left due to grinding. All polymer samples are left to dry for at least four hours in laboratory air before testing to ensure a true initial mass. Samples were tested against 304L SS countersamples that were lapped to a $R_a \sim 150$ nm. The countersamples were washed with soap and water and then rinsed in methanol at least 30 minutes before testing begins.



experimental conditions:

$$F_N = 50 \text{ or } 250 \text{ N}$$

$$P = 1.25 \text{ MPa or } 6.25 \text{ MPa}$$

$$V = 50.8 \text{ mm/s}$$

$$\text{Stroke Length} = 25.4 \text{ mm}$$

linear reciprocating tribometer

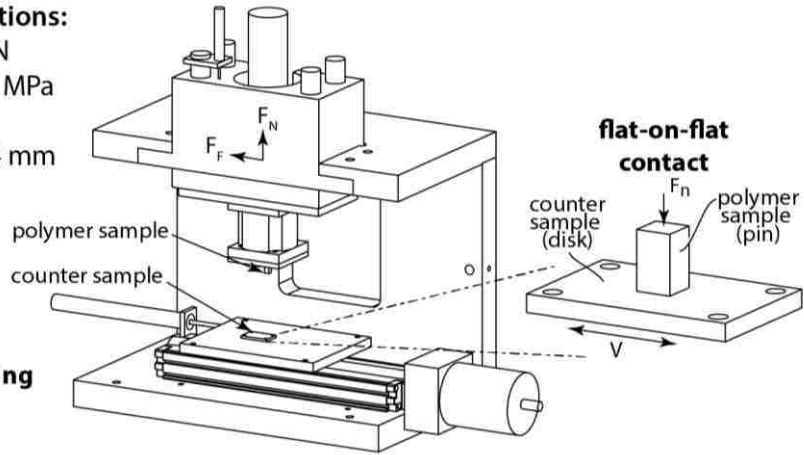


Figure 18: Linear reciprocating tribometer and flat-on-flat contact schematic.

4.2 Tribometers, friction coefficient, and wear rate measurements

4.2.1 Linear Reciprocating Tribometer

The principle tribometer used for testing the tribological properties of the fluoropolymer metal composites was the linear reciprocating tribometer (Figure 18). A linear reciprocating tribometer works by first mounting the polymer sample directly to a multi-axis load cell, which will be used to monitor friction coefficient and normal load. The load is applied by a pneumatic thruster, which presses the polymer sample onto the steel countersample. A stepper motor drives a linear ball screw stage, which controls the sliding velocity and stroke length of the experiment. All control of pneumatics, linear stage, and data acquisition is performed using LabVIEW® (National Instruments, Austin TX).

4.2.2 Friction measurements

To ensure accurate friction measurements, the load cell, polymer pin, and countersample must be properly aligned. Any misalignment, even within acceptable

machining tolerances, can lead to undesirable error and false reporting of the friction coefficient. To counter any potential effects of misalignment error, the samples friction coefficient is averaged over the middle fifty percent of the stroke [57]. This counteracts any misalignment effects and eliminates any changes in coefficient of friction due to acceleration and deceleration at the end of the stroke.

4.2.3 Wear Rate Measurements

Wear of the polymer samples is evaluated using two separate methods. The first method calculates the wear of the polymer using incremental mass measurements (Equation 2). A Mettler Toledo XS 205 precision balance was used for all experiments. This balance has a 0.01mg resolution, which allows for precise measurement for even very small wear events. The difference in the mass measurements before and after a test (Δm) is then divided by the known density of the material to determine the volume loss. Volume loss is then divided by the measured normal force and sliding distance to determine the wear rate of that test. Mass measurements are taken in a semi-logarithmic order (i.e before testing and after 1k, 2k, 3k, 4k, 5k, 10k, 20k, 30k, 40k, 50k, 100k, 200k, 300k, 0.5M cycles) to determine the evolution of the wear rate, with an emphasis of wear over the first 50,000k cycles. The second method to measure wear of polymer composite samples is through height loss (h_{loss}) measurements, which is monitored using an LVDT or linear encoder. This method allows in-situ measurement of the wear rate during sliding and is defined using Equation 3. In this case, volume loss is calculated by multiplying the change in position of the LVDT and the cross-sectional area of the polymer pin.

$$K \left(\frac{\text{mm}^3}{\text{N}\cdot\text{m}} \right) = \frac{V_{lost}}{F_n \cdot d} = \frac{\Delta m / \rho}{F_n \cdot d} \quad (\text{Equation 2})$$

$$K \left(\frac{\text{mm}^3}{\text{N}\cdot\text{m}} \right) = \frac{V_{lost}}{F_n \cdot d} = \frac{h_{loss} \cdot A}{F_n \cdot d} \quad (\text{Equation 3})$$

4.3 Characterization Methods

The primary goal of this section is to introduce to the various techniques and methods used throughout the dissertation document. These sections are meant to provide context but are in no means meant to be comprehensive guides to these techniques. More in depth information on these techniques can be found through the references mentioned in each section.

4.3.1 Surface Metrology: Coherence Scanning Interferometry (Scanning White Light Interferometer) and Stylus Profilometry

Surface Metrology is the study of how to accurately measure the height profile of a surface. There are two primary types of methods used to measure the height of asperities

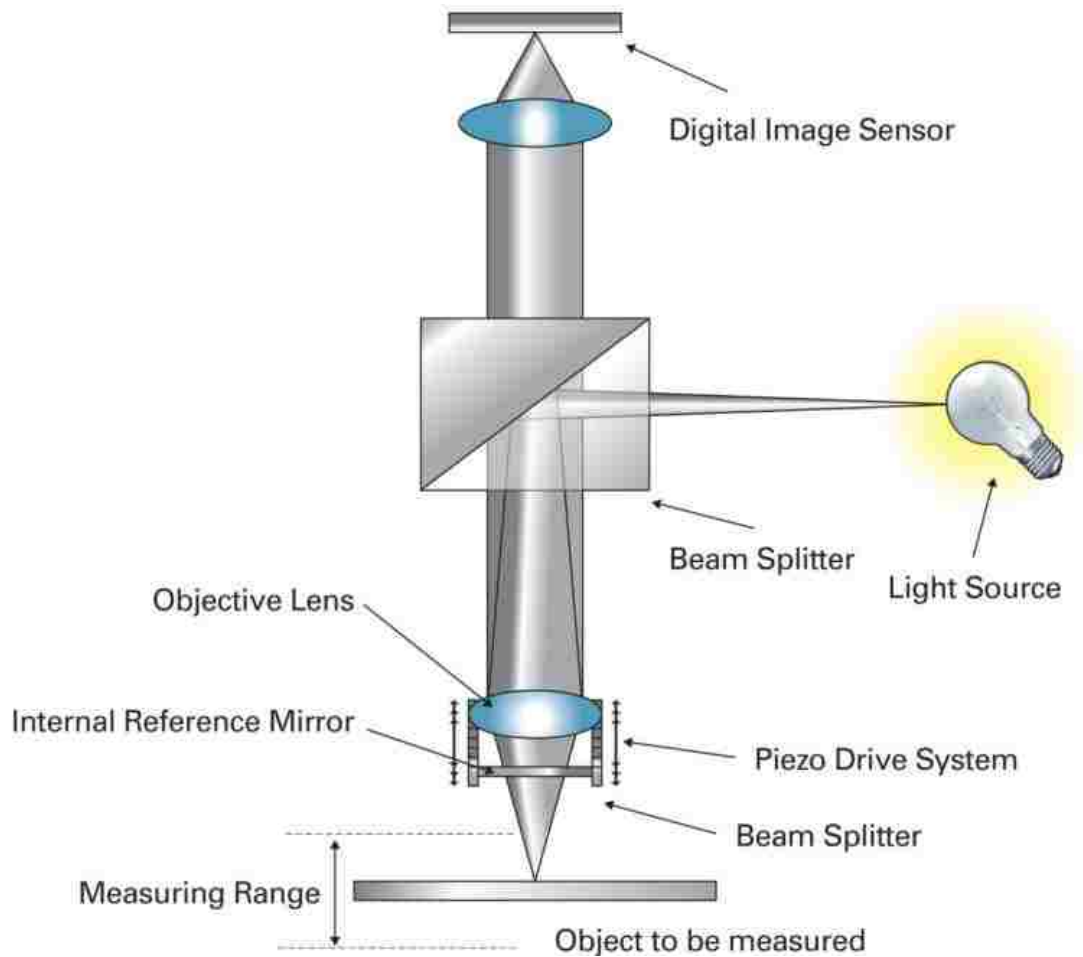


Figure 19: Basic elements of a Coherence Scanning Interferometer [59].

on a surface. The first method type is called Coherence Scanning Interferometry (Figure 19), which uses light interference to measure the height of a surface. To determine the surface profile of a sample, a beam of light enters a beam splitter and is split into two beams. One beam of light travels down to an internal reference mirror and is reflected back to the digital image sensor. The other beam of light exiting the beam splitter hits the object to be measured and reflects towards image sensor. These two beams of light create a “fringe” pattern of constructive interference at the sample height. When this constructive

interference reaches its maximum value, the distance from the sample's surface and the distance from the reference mirror are the same. By slowly lowering the objective lens, one can measure the height of each pixel within the objective lens region of focus (Figure 20). The vertical resolution of coherence scanning interferometers can range between 0.1 nm for monochromatic light sources to 1-5nm for white light sources (polychromatic) [58], [59]. Spatial resolution is limited by the Rayleigh criterion which for white light is ~100-300 nm.

The second method used to measure surface height variation across a surface is called stylus profilometry. The working principle of this method is a small probe (0.1 μm -50 μm in diameter) is held in contact against the surface to be measured at a small contact load

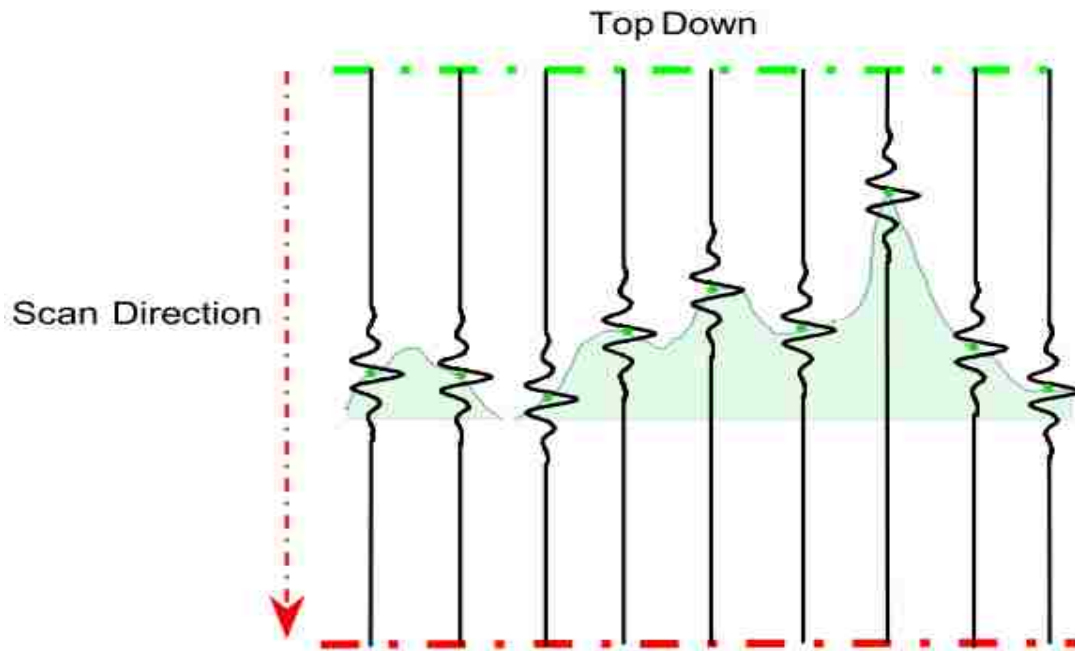


Figure 20: Diagram of how constructive interference occurs at each point along the surface as the objective lens scans vertically [59].

(1-15 mg). While the probe is being driven across the sample's surface at controlled speed, the vertical deflection of the probe is measured using a transducer. A series of line scans across the surface can be used to create a 3D map. The vertical resolution of the instrument can be as small as 0.05 nm and the lateral resolution is dependent on the radius of the stylus tip that is used. The two limitations of stylus profilometry is speed of scanning, which is significantly slower than coherence scanning interferometry and surface damage caused by the profilometer tip [58].

4.3.2 Nanoindentation Methods

Nanoindentation is a commonly used method for determining the hardness (resistance to plastic deformation) and elastic modulus of thin film materials and small-scale structures which cannot be tested using traditional tensile or bending test configurations. Nanoindentation was developed by Oliver and Pharr in 1992 and later revisited by the authors in 2004 [60]. A typical indentation test begins by a piezo-driven stage guiding a diamond indenter tip into the sample at a defined rate ($\mu\text{N/s}$ or nm/s) until a prescribed load or depth has been reached and then the tip is retracted out of the sample at a defined rate. During indentation and retraction of the tip, the force applied to the indenter tip is monitored using a force transducer. The load applied to the sample is plotted as a function of displacement. There are two sections within the load-displacement curve (Figure 21). The first section is the loading curve which begins at initial contact of the indenter and ends at the maximum applied load and depth. This section represents both elastic (recoverable) and plastic deformation (permanent) of the test specimen. After reaching maximum load,

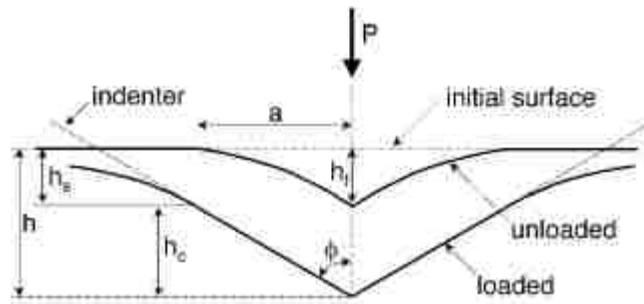
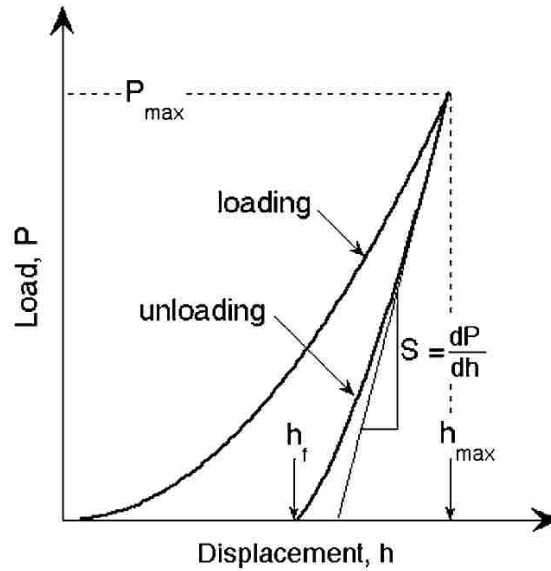


Figure 21:a) Typical load-displacement curve for nanoindentation experiment, (b) Diagram of contact area before, during and after indentation. Reprinted with permission from [60].

the indenter is unloaded from the surface. The unloading section of the curve is entirely elastic and may be used to determine the hardness and elastic modulus of the test specimen.

To determine hardness of a specimen, the maximum load P_{max} is divided by the permanently deformed contact area, $A(h_c)$ ($H = P_{max}/A(h_c)$). In order to calculate permanently deformed area, the height of contact periphery (h_c) must be calculated by subtracting the maximum depth (h_{max}) by the sink in height ($h_s = \zeta * P_{max}/S$, where $\zeta = 0.75$ in most cases and S is the slope of the unloading curve near the maximum load). Once h_c , is calculated,

it is plugged into the area function equation, which is based on the geometry of the indenter that was used and typically the equation follows the following form: $A(h_c) = C_2 * h_c^2 + C_1 * h_c + C_{0.5} * h_c^{0.5} + C_{0.25} * h_c^{0.25} + C_{0.125} * h_c^{0.125} + C_{0.0625} * h_c^{0.0625}$ where $C_2 - C_{0.0625}$ are fitting constants from an indentation calibration analysis. The effective elastic modulus of the sample is calculated using the slope of the unloading curve and the projected area of contact ($E_{eff} = S * \sqrt{\pi} / (2\beta * \sqrt{A(h_c)})$, where $\beta = 1$ typically). If the poisson's ratio of the test specimen is known, the elastic modulus of the specimen may be determined using $1/E_{eff} = (1-\nu^2)/E + (1-\nu_i^2)/E_i$, where the subscript i denotes the elastic modulus of the indenter.

4.3.3 Infrared Spectroscopy (Attenuated Total Reflectance, Transmission, and Reflectance)

Infrared (IR) spectroscopy is a characterization technique that utilizes vibrational theory to identify types of bonds present within a sample. IR spectroscopy requires that the vibration of these bonds produce an associated dipole moment or there will be no absorbance of infrared light. The frequency of absorption for a particular bond is dependent on (1) the mass of the two atoms (lighter atoms vibrate faster) and (2) the strength of the bond between the two atoms (atoms connected with a double bond vibrate faster than the same atoms connected with a single bond). During an infrared spectroscopy scan, an infrared laser is pointed towards a sample and the laser is transmitted to an infrared detector. The IR detector determines the amount of light that has been transmitted through the sample for the range of measured frequencies (typically between 500 cm^{-1} - 4000 cm^{-1} wavenumber) which is given as a percentage of the incident IR beam. These transmitted intensities are typically plotted as a function of wavenumber. IR spectra are also commonly

plotted as absorbance as a function of wavenumber ($Absorbance = 2 - \log(\%Transmittance)$).

Three types of infrared spectroscopy were used in the context of this thesis. The first type of IR technique is called transmission infrared spectroscopy. A thin film (typically 100-1000 μm in thickness) of a sample is created typically through compressive force (such as a bolt or hydraulic press). If the quantity of the sample to be tested is in very small supply, it may be added and ground with ionic salts (KBr is often used). Ionic salts do not absorb IR light between 400-4000 cm^{-1} , which is the range of most IR experiments. The sample is placed in direct line of an infrared beam and the transmission spectra is collected (Figure 22). This technique was utilized exclusively to measure the chemical spectra of the wear debris collected at the edge of the transfer films.

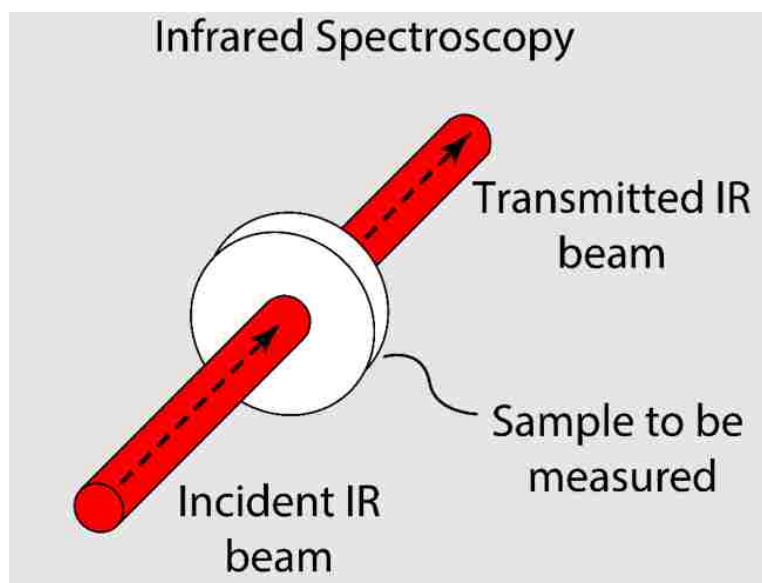


Figure 22: Simplified principles of the transmission infrared spectroscopy technique.

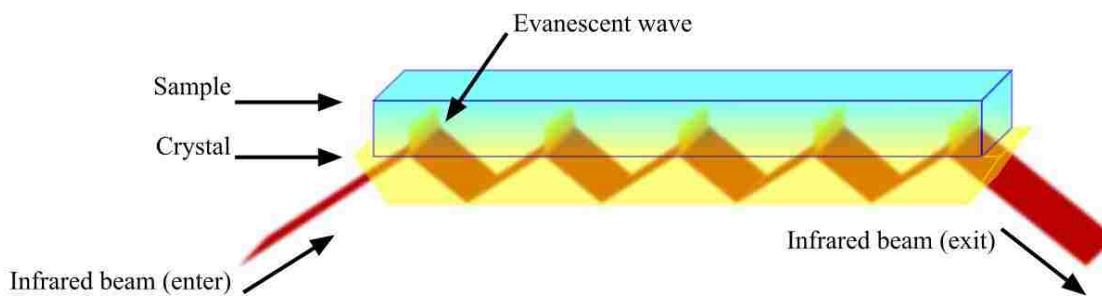


Figure 23: Schematic of attenuated total reflectance infrared light spectroscopy.

Attenuated total reflectance infrared spectroscopy (ATR-IR) was the second type of IR spectroscopy used on fluoropolymer-alumina composite systems. In ATR-IR, an infrared beam enters a crystal with a high index of refraction that will internally reflect the infrared beam and contact the sample that is pressed onto the crystal surface. This technique typically penetrates 0.5-2 μm into the sample to be tested and then is reflected into the crystal (Figure 23). One advantage of ATR-IR over transmission infrared spectroscopy is due to its limited penetration depth, it can be used to measure samples within water, which would completely absorb all IR light using in the transmission method. A third method of infrared analysis called reflectance infrared microscopy utilized the reflectance of infrared light from the surface of a specimen. This method is often coupled with an optical microscope and can be used to determine spatial differences in chemical signal on a sample. In this work, this method was typically used to characterize the transfer film deposited on the stainless steel countersurface.

4.3.4 Differential Scanning Calorimetry (DSC)

Differential Scanning Calorimetry (DSC) is a common method used to evaluate the thermal properties (crystallinity, glass transition temperature, and melt temperature) of

polymer materials. A sample of polymer (typically between 2-10mg) is loaded into a small tin container that is pressed-sealed shut. An empty tin container is used as a control to compare to the polymer sample. Both samples are heated using a servo heating system which measures precisely the amount of energy supplied to each sample in order for it to rise at the user defined rate (in this work, samples were heated at samples at 10°C/min). The heat flux rates are normalized by sample weight and plotted as a function of temperature (Figure 24).

There are two types of transitions that are often observed in DSC curves. First order transitions are defined as peaks on the DSC plots. Two first-order transitions of primary importance are the melting peak (endothermic) and crystallization peak (exothermic).



Figure 24: Schematic of major components of a differential scanning calorimetry plot.

These peaks can be integrated with respect to the baseline heat capacity to determine the heat of fusion (ΔH_f) and heat of crystallization (ΔH_c) of the polymer. The heat of fusion may be used to determine the crystallinity of a polymer sample by dividing by the idealized heat of fusion for a 100% crystalline polymer ($\% \text{ Crystallinity} = (\Delta H_{f, \text{ measured}} / \Delta H_{f, \text{ ideal}}) * 100\%$). It is possible for a polymer to have first-order transitions below the melting/crystallization peaks. These are due to crystallographic changes (mesophasic transitions (solid-solid) transitions, i.e. triclinic to hexagonal) within the crystalline region of the polymer. The other type of transitions that can often be observed in DSC curves are second order transitions associated with the glass transition temperature. These appear as

steps on the DSC endotherms and signal when a polymer transitions from its glassy to its rubbery state (Figure 24). This temperature is associated with a drastic difference in mechanical properties of polymers. Often a three-order reduction in elastic modulus is observed when heating a polymer past its glass-transition temperature.

In DSC analysis of polymers, it is very important to complete a full melt, crystallization, and complete second melt to determine the influence of thermal history on thermal properties such as ΔH_f . For example, two samples of the same polymer that were cooled at different rates will have very different first melting curves. After recrystallization, the second melt of these polymers should be identical since the samples have the same chemical structure and molecular weight distribution. Therefore, the DSC first melt can be used to determine differences in thermal/mechanical history between two polymer samples while the second heat can be used to determine if any chemical differences (molecular weight, percentage of comonomer) between two samples of the same polymer type may exist. It should be noted that DSC does not directly measure molecular weight or percentage of comonomer, but differences in the second heat could imply these differences exist if the composition of the two samples being compared are well known.

4.3.5 X-Ray Diffraction (SAXS and WAXS)

Wide angle x-ray diffraction may be used to determine the interplanar atomic distance, d (Bragg's Law) and the average size of the crystalline domains, D (Scherrer equation). The working principle behind X-ray diffraction is that X-rays at certain angles constructively interfere with one another, and these angles correspond to certain crystallographic planes. Using Bragg's law one can determine the interplanar spacing d of

for the peak at angle θ (typically $2\theta = 10-90^\circ$). The FWHM of this peak at θ can also be used to approximate the average crystalline size domain, D .

$$\text{Bragg's Law: } d = \frac{n\lambda}{2 \sin \theta}$$

$$\text{Scherrer Equation: } D = \frac{K\lambda}{B \sin \theta}$$

Small angle X-ray diffraction is typically measured between $2\theta = 0-10^\circ$ is used to determine larger structures within a sample. In SAXS, the typical convention is to plot intensity as a function of the scattering vector, q which is equal to $4\pi \sin \theta / \lambda$. Typically the scattering intensity $I(q)$ will give a misrepresentation of the 2D data. To correct for this misrepresentation, the Lorentz Correction can be used by plotting the $I(q) \cdot q^2$ as a function of q . This helps remove any bias and produces much cleaner graphs with obvious peaks. The value of θ at the maximum peak intensity may be used to determine the average interplanar spacing, d similar to WAXS. Additional information about the polymer including the crystallinity, the average lamellar thickness, the long spacing (average distance between crystallites), and the electron density between samples may be determined. The details of these calculations are may be found in referenced [61].

Chapter 5: Nanomechanics of Metal-Oxide Filler Particles lead to Ultralow Wear Fluoropolymers

5.1 Overview

Recent work in the tribological community has highlighted the role of particle properties (size and porosity) in the formation of ultralow wear ($K < 5 \times 10^{-7} \text{ mm}^3/\text{Nm}$) PTFE alumina composites. The goal of this work is to determine how the hardness of metal-oxide particles affect the tribological performance (friction and wear) of PTFE-metal-oxide composite systems through coupled tribology, profilometry, infrared spectroscopic experiments coupled with in-situ nanoindentation of the metal oxide particles themselves. Four types of alumina particles ranging between 4-15 μm in size with varying porosity and one CoAl_2O_4 particles ranging with an average particle size near 1-2 μm were chosen for these experiments. Wear rate and friction coefficient were lowest for the porous 4 μm alumina composites while the dense 15 μm alumina composite had the largest wear rate and friction coefficient. Abrasive scratches were present on the metallic counterface for the dense 4 μm , dense 8 μm and 15 μm alumina composites through optical profilometry. ATR-IR measurements revealed similar chemical structure on the worn polymer composite surface regardless of particle type used. In-situ indentation experiments determine the dense 8 μm and dense 15 μm alumina particles had hardness values between 6-10 GPa while the hardness of the porous alumina particles ranged between 0.31-2.5 GPa. A clear trend between particle hardness and wear of the composite material was established with softer

compliant particles promoting ultralow wear and thin-robust tribofilms in contrast to the high abrasion of the counterface observed by the PTFE-dense alumina composites.

5.2 Motivation

Understanding what properties make a successful filler particle is crucial to create an ultralow wear fluoropolymer composites. Not all metal-oxide particles composited with PTFE will develop ultralow wear. Originally, particle size was thought to be the most

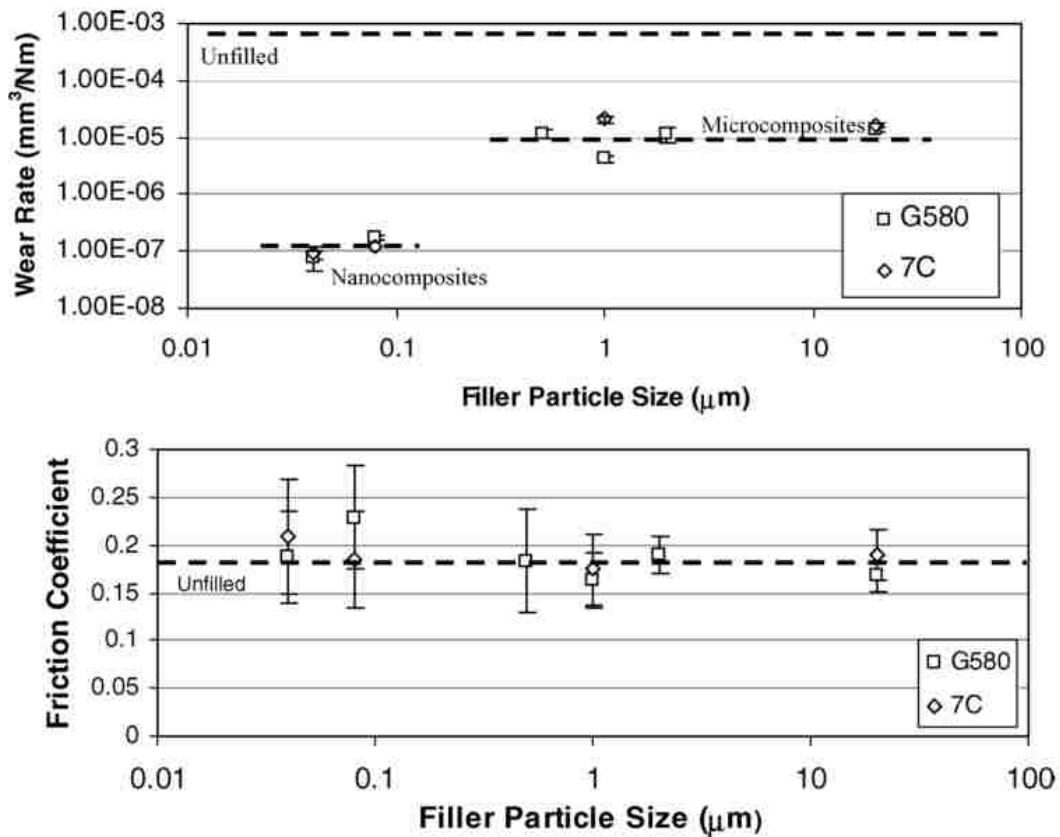


Figure 25: Wear rate of PTFE-Alumina composites was shown to drop by 100x for particles below 500nm threshold by Blanchet et al. The friction coefficient for both systems was found to be independent of particle size. Reprinted with permission from [41].

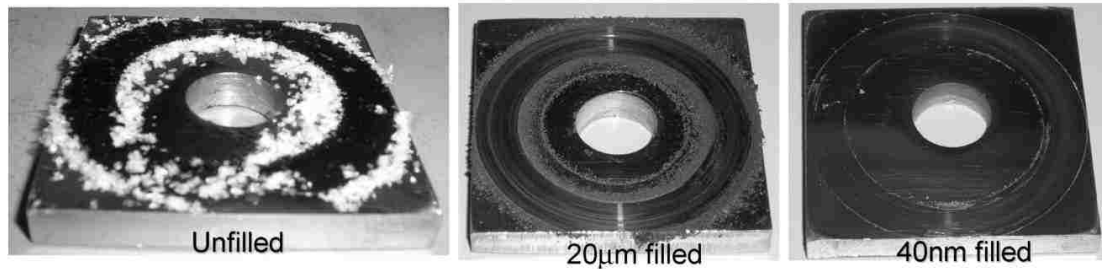


Figure 26: Difference observed in transfer films of PTFE composited with different size alumina fillers. Reprinted with permission from [41].

important characteristic of the metal-oxide particle in creating ultralow wear composites. In 2008, Blanchet *et al.* tested several types of alumina (Al_2O_3) particles ranging from 40 nm to $20\mu\text{m}$ in supplier designated size [41]. The authors determined that PTFE filled with alumina smaller than 500 nm achieved ultralow wear rates ($K \sim 8 \times 10^{-7} \text{ mm}^3/\text{Nm}$) while PTFE composites filled with alumina above the 100 nm threshold had more modest wear improvements ($K \sim 1 \times 10^{-5} \text{ mm}^3/\text{Nm}$) (Figure 25). The less abrasive nature of the nanoparticles compared to the microparticles was claimed to be the cause of the 100x difference in wear performance between the composites. These nanoparticle-alumina-filled PTFE composites also developed a thin, well-adhered brown transfer film on top of the surface of the steel counterface while no film developed for the microalumina PTFE composite materials (Figure 26).

A few years later, the theory that particle size was the critical factor in creating ultra-low wear PTFE alumina composites was challenged by Krick *et al.* [62]. Krick *et al.* performed a series of wear experiments that composited PTFE with many of the same particles of the study by Blanchet *et al.* and some additional new particles. During these experiments, one type of alumina particle (“alumina b”), highlighted in Figure 27, was

found to produce ultralow wear behavior that despite being reported as 500nm in diameter by the supplier (over the original 100nm threshold claimed by Blanchet *et al.*). Due to this discrepancy, the authors characterized each alumina particle using nitrogen gas adsorption to measure the total surface area of the particle (BET Method [63]) and by static light scattering (SLS [64]) to determine the true average particle size. From these analyses, the supplier designated particle sizes in many cases were found to be erroneous. The “alumina e” particle was reported to be 100x smaller (40 nm) than its actual measured size (~4 μm). Krick *et al.* concluded that the truly nanometer-sized particles (<100 nm) do not allow for ultralow wear behavior to occur but nanostructured (porous) micron-sized particles promoted ultralow wear PTFE composites. Increase in surface area to particle diameter ratio also corresponded to a reduction in wear rate PTFE composites. Small, dense (small particle diameter to surface area ratios) were found to have high wear with poor transfer film development. The large, porous particles (large particle diameter to surface area ratios) developed thin robust brown transfer films [62].

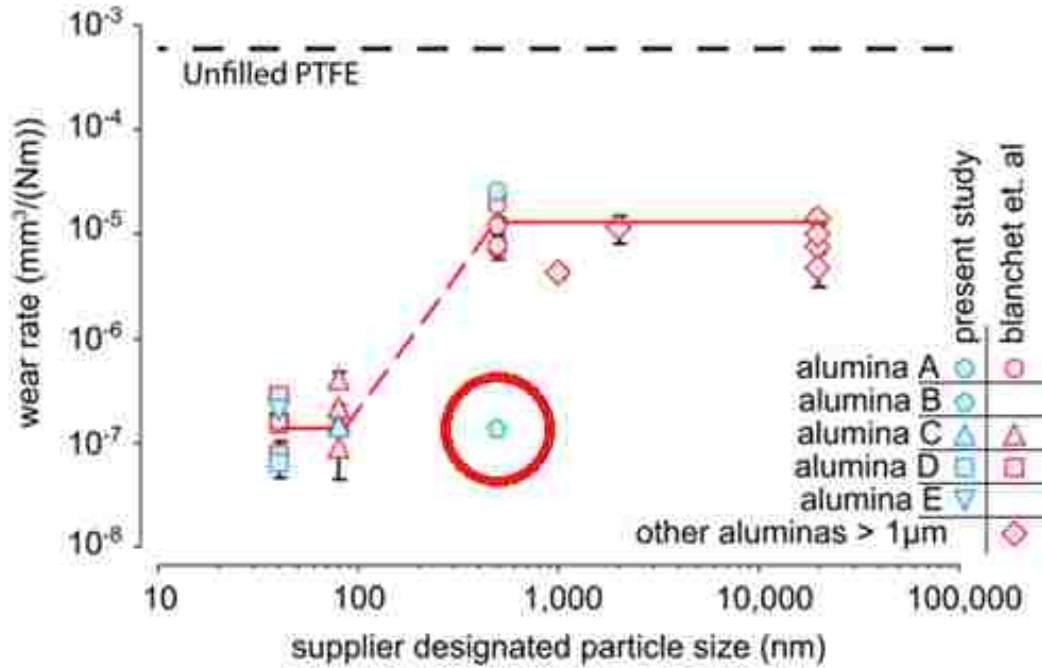


Figure 27: Summary of wear rate versus supplier designated particle size. The outlier particle in circled in red which is micro in size but still ultralow wear [62].

In the proceeding work, four different types of Chemours ® PTFE 7C-alumina (5 wt.%) composites (four different batches of alumina powder ranging between 4-15 µm) and one Chemours ® PTFE 7C-Ferro Blue oxide composite were slid for 25 km to evaluate their wear and friction properties. After sliding tests were completed, optical profilometry scans of the transfer films were completed to quantify any abrasive wear of the stainless steel counterfaces. Infrared spectroscopy of the running films of each polymer composite was used to determine any chemical differences between the running films of various PTFE-metal oxide composites. Lastly, in-situ nanoindentation was used to characterize the hardness of some of the alumina particles tested.

5.3 Hypothesis

The addition of porous metal-oxide particles will lead to ultralow wear composite surfaces with robust running and transfer films. The addition of dense alumina particles of 4, 8 and 15 microns in size will abrade the counterface and develop uneven transfer films, if any transfer films at all. Amongst the dense alumina particles, the smallest alumina particle will have the lowest wear rate while the largest alumina particle will have the highest wear rate. Due to the similarity in chemistry of all these particles, it is expected that the running film surfaces of all these composites have very similar infrared spectra. A strong trend between the mechanical properties of the particles and the wear rate of the system will occur with soft, compliant particles producing the lowest wear rates while the stiffer, harder particles will produce composites with high wear rates.

5.4 Materials and Methods

5.4.1 Materials and Material Preparation

All PTFE composites used Chemours PTFE 7C grade resin which has an average particle size of $\sim 30\mu\text{m}$. The resin was mixed with 5 wt. % of the porous $4\mu\text{m}$ α -phase Al_2O_3 particles, dense $4\mu\text{m}$ α - Al_2O_3 , dense $8\mu\text{m}$ α - Al_2O_3 particle, dense $15\mu\text{m}$ α -phase Al_2O_3 particles, and cobalt aluminate particles between 500 nm - $10\mu\text{m}$ in size (CoAl_2O_4). More information, including supplier, product #, Surface Area by N_2 gas adsorption, and

Table 3: Particle manufacturer and reported particle size of metal-oxide particles used in PTFE composites.

Particle Type		vendor reported
shorthand reference	Source	particle size μm
Porous 4 μm	Nanostructured & Amorphous Materials, Inc. (1015WW), Houston, TX	0.027-0.043
Dense 4 μm	Pace Technologies (ALR-1200-05), Tucson AZ	5
Dense 8 μm	Pace Technologies (ALR-1200-05), Tucson AZ	12
Dense 15 μm	Pace Technologies (ALR-2000-05), Tucson AZ	20
CoAl ₂ O ₄	Ferro Corporation (V-3285), King of Prussia, PA	1.5-2.0

Table 4: N₂ Gas adsorption (BET, specific surface area), and Static Light Scattering (SLS, true particle diameter) of metal-oxide particles composited with PTFE.

Particle Type shorthand reference	vendor reported particle size μm	BET		SLS		
		surface area m^2/g	D μm	D25 μm	D50 μm	D75 μm
Porous 4 μm	0.027-0.043	41.4	0.036	2.035	4.149	7.123
Dense 4 μm	5	2.3	0.660	2.637	4.396	6.331
Dense 8 μm	12	0.34	4.422	6.244	8.117	9.629
Dense 15 μm	20	0.12	12.658	11.917	15.362	18.631
CoAl ₂ O ₄	1.5-2.0	5.8	0.262	N/A	2	N/A

D₅₀ diameter size by Static Light Scattering are shown in Table 3 and Table 4. Additional sample preparation details may be found in §4.1.1.

5.4.2 Tribological Experiments

All tests were performed on a linear reciprocating tribometer. The testing conditions for all experiments were: applied load 250N (6.25MPa), sliding velocity 50 mm/s, and sliding stroke 25mm. Mass measurements were taken after 50, 100, 150, 200, 250, 500, 1,000, 1,500, 2,000, 2,500, 5,000, 10,000, 15,000, and 25,000m to determine

wear rate as a function of sliding distance and to better observe the changes in wear performance during the first 5000m of the experiment.

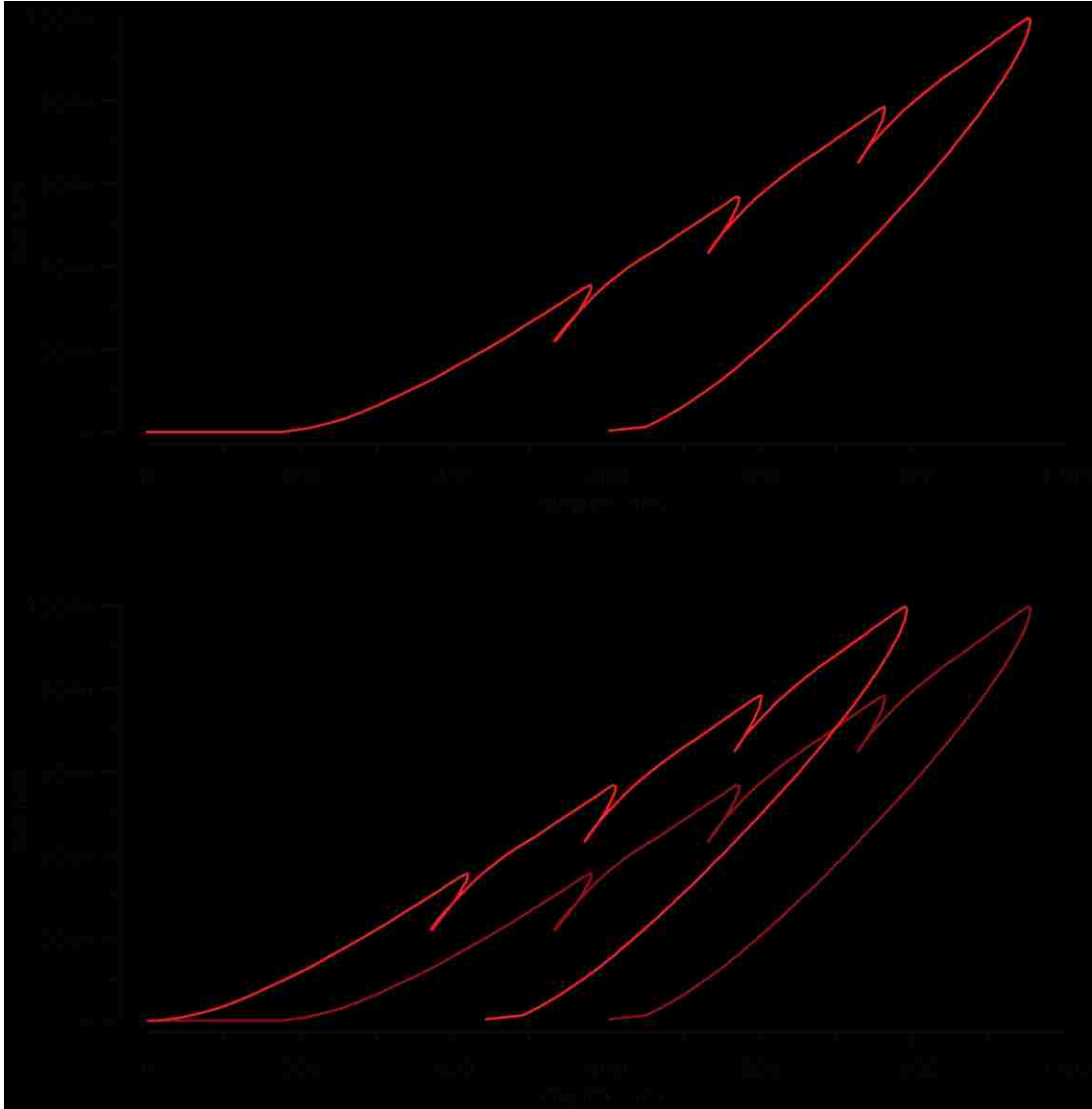


Figure 28: Indentation Data Analysis Procedure. (Top) Load does not begin immediately, as tip is still approaching the particle's surface, which may affect hardness and modulus calculations. (Bottom) Depth data is shifted so loading begins at zero contact depth.

5.4.3 In-Situ Nanoindentation Experiments

To prepare particles for nanoindentation experiments, a small amount (0.1 mg/ml) of each particle type was diluted with isopropanol then sonicated for 30 minutes to break up any loosely agglomerated particles. A pipette was then used to drop the isopropanol mixtures onto a sapphire substrate (0.5” diameter, .05” thick) that was mounted onto an aluminum scanning electron microscopy (SEM) mount. The samples were then carbon coated to prevent electron charging within the SEM.

All indentation experiments were performed on a Hysitron® PI-85 Picoindenter (Eden Prairie, MN) using a diamond cube corner tip geometry. The sharp point of the cube-corner geometry was chosen because it would induce the largest stress on the particles. All experiments were performed with intermediate unloading steps to allow for hardness to be calculated at multiple points during the indentation cycle. Before analyzing the load-displacement data to determine reduced modulus and hardness, the raw data was modified to ensure the first loading curve began at the origin (Figure 28). The first ten percent of each of the unloading curves was used to calculate the slope which is needed to calculate the depth of the contact periphery, h_c (Figure 29). Using the periphery contact depth, h_c , the contact area was calculated using the six-order area function of the cube corner diamond indenter. All dense particles were tested at three maximum loads (2000 μ N, 4000 μ N, and 10000 μ N (the load capacity of the nanoindenter)). The strong 4 μ m porous particle was tested using displacement control at a loading/unloading rate of 5 nm/s, while the “weak” porous particle was tested using load control at 4 μ N/s. The indentation rates for the dense particles were 20 μ N/s, 40 μ N/s, and 100 μ N/s, with a total indent time of 300s. Partial

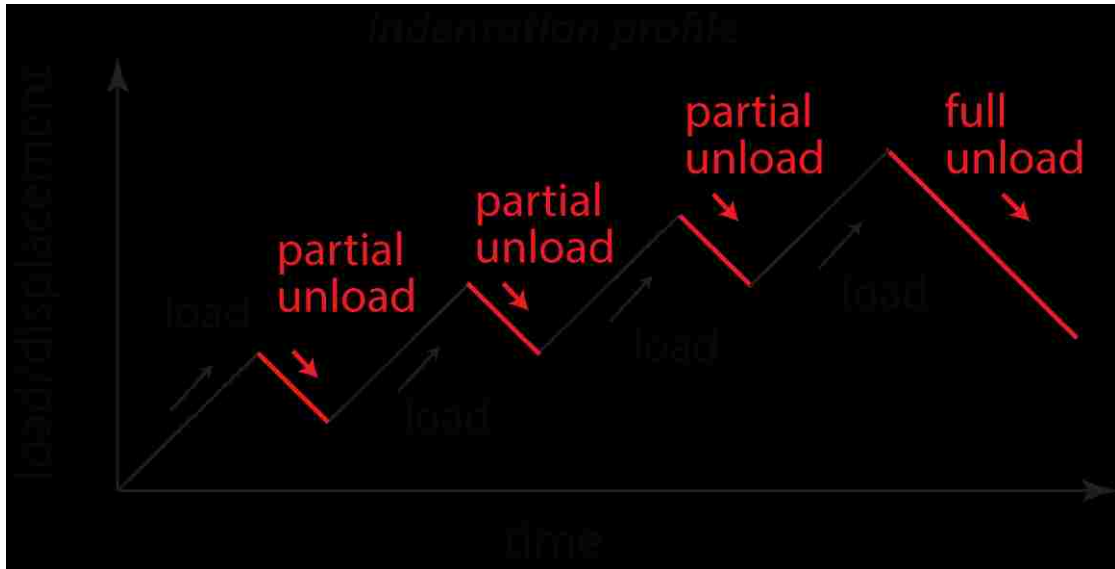


Figure 29: Schematic of load as a function of time for particle indents. The slope of the unloading curves was taken from the first 10% of the data.

unloads were reduced by a quarter of the magnitude of the max indent load (e.g. 500 μN for a 2000 μN max load).

5.5 Results & Discussion

5.5.1 Friction and Wear Results

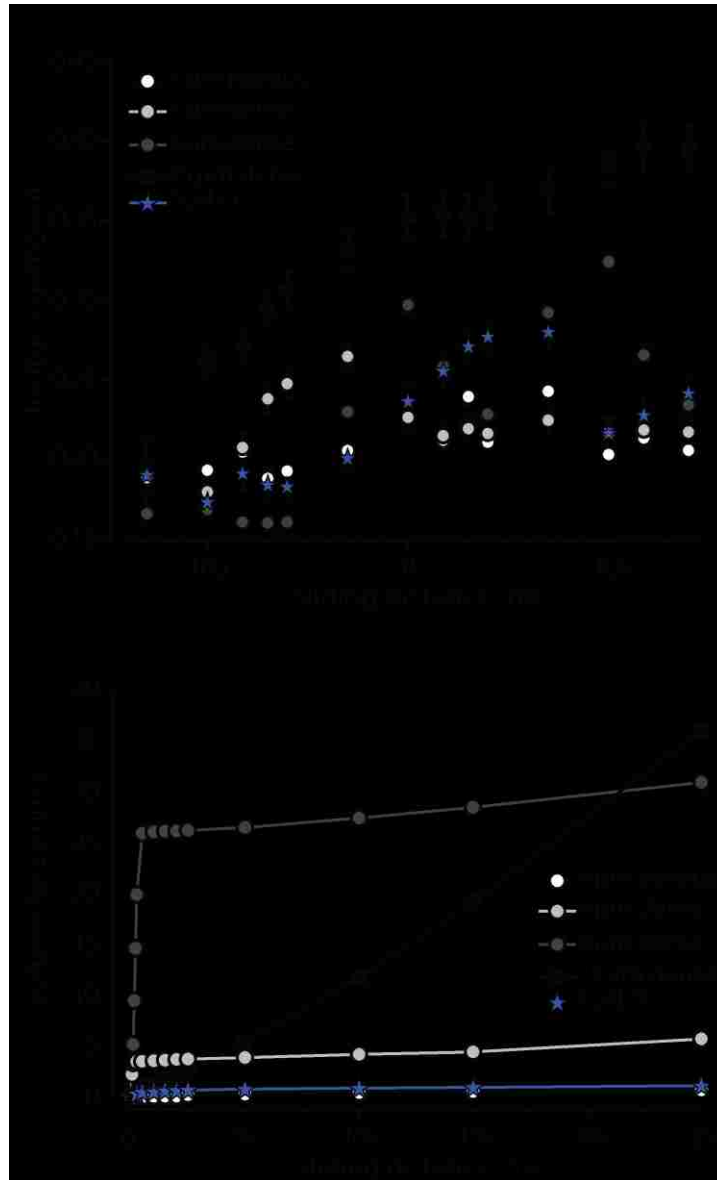


Figure 30: Tribological Results for alumina filled PTFE experiments. (a) friction coefficient as a function of sliding distance (note x-axis is logarithmic) (b) Volume lost vs sliding distance for all three PTFE Al_2O_3 composites tested. Slope of these curves corresponds to the wear rate (steep slope-higher wear, shallow slope-lower wear rate)

The friction and wear results are highlighted in Figure 30a, Table 5, and Table 6. Table 6: Wear rates for the five PTFE metal-oxide composite materials averaged over the first 10,000 cycles, 50,000 cycles, the entire experiment (500,000 cycles), and for the last 200,000 cycles. Friction coefficient for all composites was low over the first 1000 cycles ($\mu \sim 0.16-0.19$). The dense 15 μm alumina composite showed a rapid increase in friction coefficient to above 0.25 during the next 1000 cycle experiment. Friction coefficient for the dense 15 micron particle composite continued to increase during the entirety of the experiment reaching a final friction coefficient of 0.39 during the last 200k sliding cycles. The dense 8 μm particle composite showed low friction coefficient over the first 5000 cycles ($\mu < 0.18$) but gradually the friction increased during the duration of the experiment with some tests achieving friction coefficients above 0.3. Friction of the PTFE-dense 4 μm particle was initially high and then settled near 0.22 for most of the experiment. The CoAl_2O_4 oxide had slightly higher friction after low initial friction but settled down to a final friction coefficient of 0.24 over the last 200,000 cycles. The porous 4 μm alumina composite had the most consistent frictional performance of all the PTFE composites over the course of the 25 km experiment. PTFE- porous 4 μm composites exhibited a minimum friction coefficient of 0.19 and a maximum value of 0.24 for any single experiment.

Total volume loss as a function of sliding distance for all tests are represented in Figure 30b. The slope of this curve is representative of the wear rate for each experiment. During the first 10k cycles, the dense 8 micron Al_2O_3 composite exhibited very high wear near that of unfilled PTFE ($\sim 2 \times 10^{-4} \text{ mm}^3/\text{Nm}$). After this point, the wear decreased dramatically down to as low as $2 \times 10^{-7} \text{ mm}^3/\text{Nm}$ between 1.5-2.0 km. After this point the wear of the

material steadily increased until reaching a final wear rate of $1.0 \times 10^{-6} \text{ mm}^3/\text{Nm}$. The dense $15 \mu\text{m}$ alumina particle initially had very low wear that reached as low as $3.7 \times 10^{-7} \text{ mm}^3/\text{Nm}$ during the first 250 m of sliding. After this initial low run in period, the wear steadily increased in every subsequent experiment, leading to a final wear of nearly $7.3 \times 10^{-6} \text{ mm}^3/\text{Nm}$. The dense $4 \mu\text{m}$ particle performed fairly well over the course of the experiment, with a final wear rate of $5.13 \times 10^{-7} \text{ mm}^3/\text{Nm}$ over the last 200,000 cycles. PTFE- CoAl_2O_4 had a very short run-in period (low wear rate over the first 50k cycles $1.1 \times 10^{-6} \text{ mm}^3/\text{Nm}$) and reached a minimum wear rate of $7.0 \times 10^{-8} \text{ mm}^3/\text{Nm}$ over the last 10 km of sliding (200,000 cycles). The behavior for the porous $4 \mu\text{m}$ Al_2O_3 composite was consistently low and never reached a value higher than $6 \times 10^{-6} \text{ mm}^3/\text{Nm}$. The minimum wear rate of the composite was achieved during the longest experiment (200k cycles, 10 km sliding distance).

Table 5: Friction coefficient for the five PTFE metal-oxide composite materials averaged over the first 10,000 cycles, 50,000 cycles, the entire experiment (500,000 cycles), and for the last 200,000 cycles .

# Cycles	friction coefficient			
	10k	50k	500k	final 200k
Sample Name				
Porous 4 μm	0.20	0.22	0.21	0.21
Dense 4 μm	0.24	0.22	0.22	0.22
Dense 8 μm	0.20	0.24	0.27	0.23
Dense 15 μm	0.30	0.34	0.39	0.39
CoAl ₂ O ₄	0.19	0.25	0.24	0.24

Table 6: Wear rates for the five PTFE metal-oxide composite materials averaged over the first 10,000 cycles, 50,000 cycles, the entire experiment (500,000 cycles), and for the last 200,000 cycles .

# cycles	Wear Rates			
	10k	50k	500k	last 200k
Sample Name	mm ³ /Nm	mm ³ /Nm	mm ³ /Nm	mm ³ /Nm
Porous 4 μm	6.20E-07	4.40E-07	1.10E-07	5.80E-08
Dense 4 μm	2.70E-05	6.00E-06	9.20E-07	5.10E-07
Dense 8 μm	2.10E-04	4.30E-05	5.00E-06	1.00E-06
Dense 15 μm	8.50E-06	4.00E-06	6.20E-06	7.30E-06
CoAl ₂ O ₄	4.20E-06	1.10E-06	1.80E-07	7.00E-08

6.5.2 Running Film and Transfer Film Development

The differences in wear and friction performance can be better understood by investigating the evolution of the running and transfer films that developed on the surface of the polymer composite and stainless steel counterface respectively. Initially, all five running films developed a brown running film (Figure 33). This brown film has been

identified as carboxylic salts that develop in PTFE-alumina systems. During the duration of the experiment, the running films of the 8 μ m and 15 μ m alumina samples grew increasingly darker and eventually led to the formation of dark, grey inclusions that appear to be abraded particles of stainless steel from the counterface. This is obvious in the case of the 15 μ m Al₂O₃ PTFE composite, which is entirely covered in steel particulates after the experiment in complete (Figure 31). The dense 4 μ m Al₂O₃ running film remains a dark

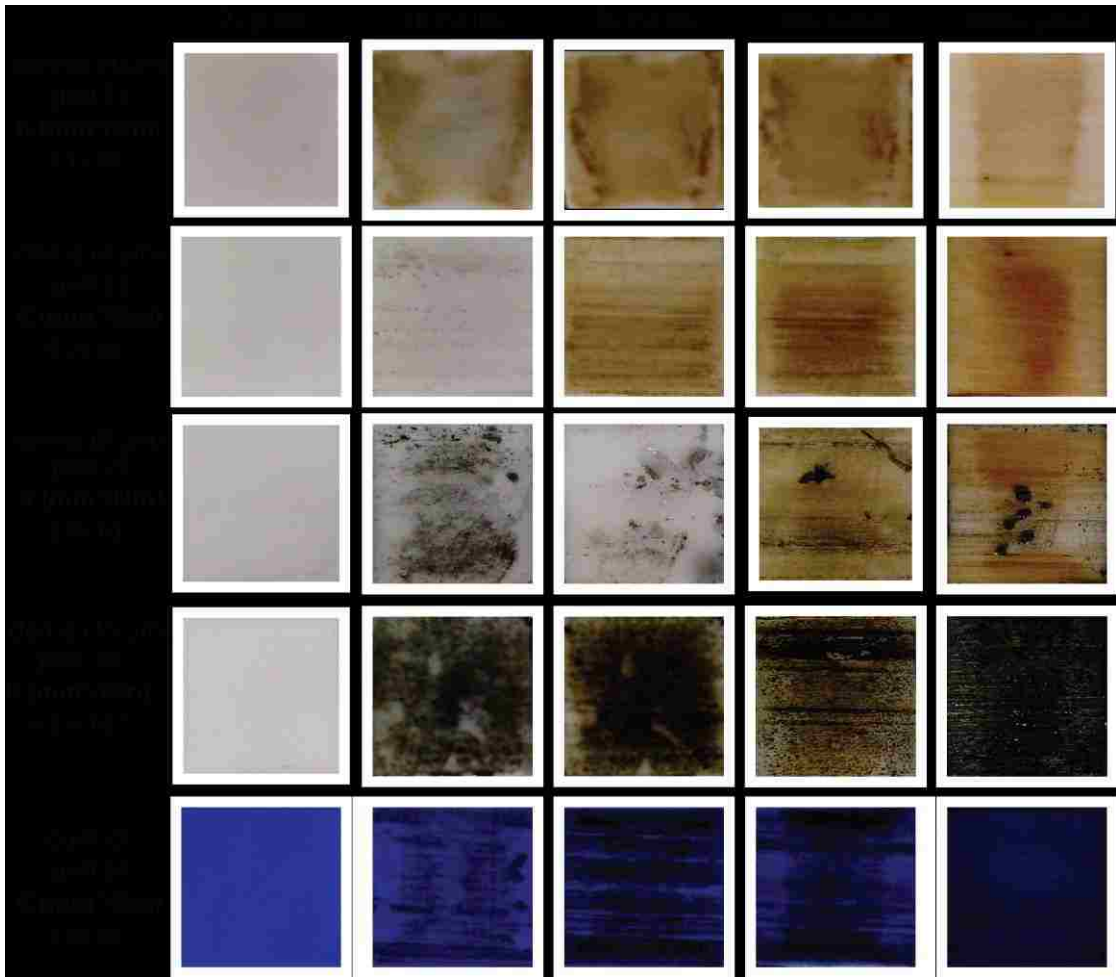


Figure 31: Photograph images of the worn surface of the five composite samples are highlighted before testing, after 1,000 cycles (50 m), after 5000 cycles (250 m), after 10,000 cycles (500 m), and after 500,000 cycles (25 km).

brown color even after 500,000 sliding cycles. The porous 4 μm Al_2O_3 and CoAl_2O_4 composite develop brown films very quickly and these films faded in color after 500,000 cycles were complete.

Transfer films that developed on each stainless steel counterface for each of these composites are very different in appearance (Figure 32). For the porous 4 μm alumina composite, the metal counterface developed a thin (~500 nm-1 μm thick) film that was slightly thicker near the ends of the wear track. PTFE- CoAl_2O_4 had a very even brown transfer film develop that was a few microns in thickness. The dense 4 μm Al_2O_3 -PTFE composite transfer film was thickest around the reversal points at the end of the wear track. There was some noticeable scratching of the metal countersurface in the middle of the wear

track which was evident in the profilometry scans. The wear track of the dense $8\mu\text{m Al}_2\text{O}_3$ composite material shows patches of brown transfer film but also shows significant abrasive scratches on the surface. This is highlighted by the Scanning White Light

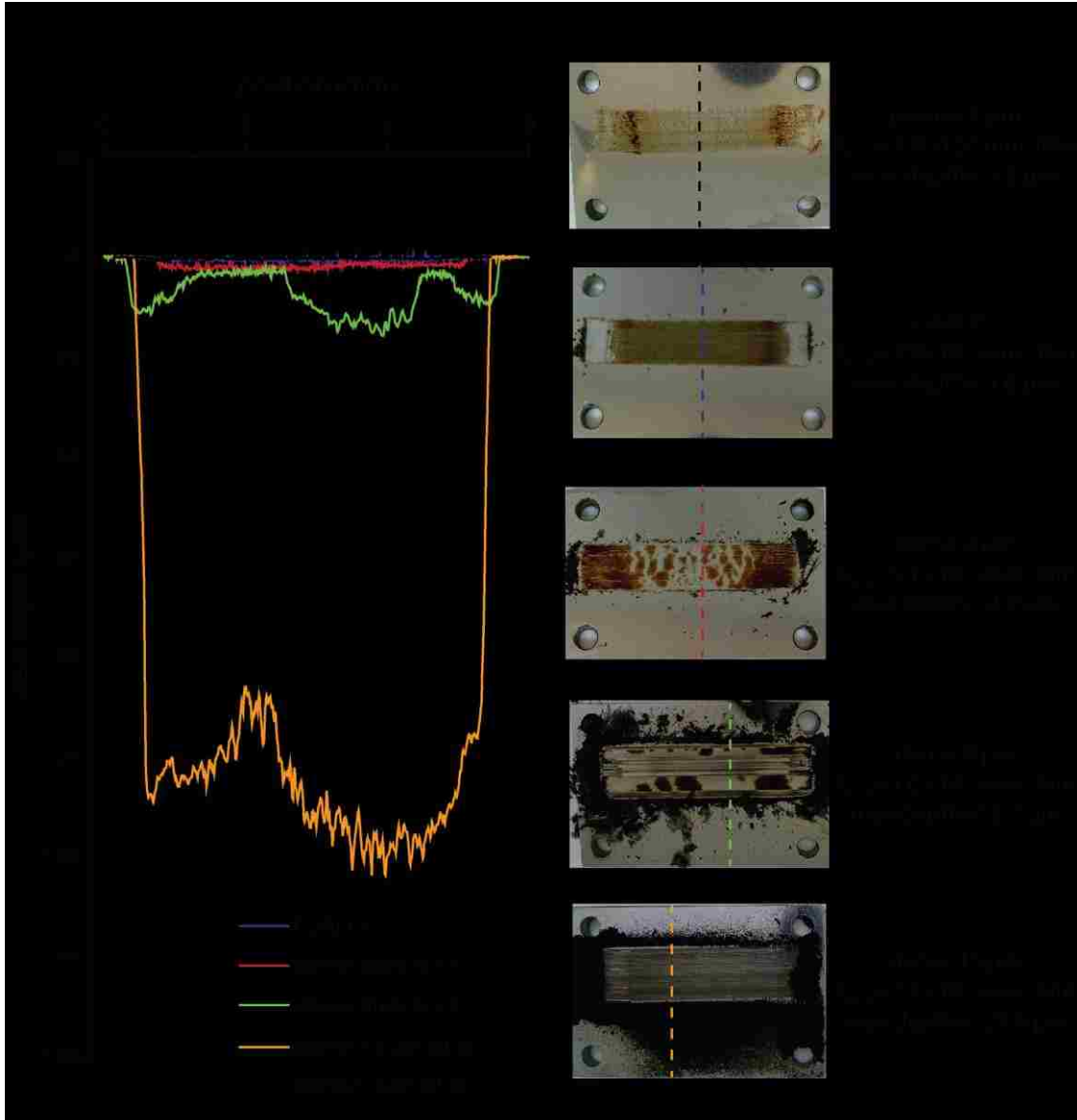


Figure 32: Scanning White Light Profilometry scans across the transfer film of the five types of PTFE-metal oxide composites. The maximum depth across each scan and wear rate over the last 10km of sliding (200k cycles) is highlighted on the right hand side of the figure.

Interferometry (SWLI) across the wear track (Figure 32). Certain areas of the counterface slid against the PTFE-8 μm Al_2O_3 composite were 16 μm below the original counterface surface. The PTFE-dense 15 μm alumina composite counterface had no transfer film and deep scratching of the counterface. SWLI scans across the wear track revealed abrasive wear of the countersurface up to 124 μm in depth. It is clear from the difference in the tribofilms that the abrasiveness of the filler particle plays a critical role in allowing the PTFE-alumina composite system achieve ultralow wear rates ($K < 5 \times 10^{-7} \text{ mm}^3/\text{Nm}$).

5.5.3 Infrared Spectroscopy of Running Films

Attenuated total reflectance infrared spectroscopy was performed on the bulk (unworn) composite surface and running film (worn surface) after all tests were completed (500k cycles, 25 km of sliding). The initial spectra of all five composites revealed two peaks at 1159 cm^{-1} and 1216 cm^{-1} corresponding to CF_2 bonds. The shoulder of the infrared spectra under 900 cm^{-1} revealed corresponds to metallic oxides, in this case likely alumina or cobalt aluminate. The porous 4 μm particle, dense 4 μm particle, and cobalt aluminate samples had stronger metal-oxide signals than the other alumina composite materials, suggesting a higher concentration near the running surface. The infrared spectra after sliding for all three

composites were similar in character. All three composites had strong absorbance peaks corresponding with carboxylic acids and an increase in the signal of within the metallic oxide region. The diminished signals for the PTFE-dense 15µm alumina spectra is due to poor signal from all the metallic wear debris embedded in the running film (worn surface).

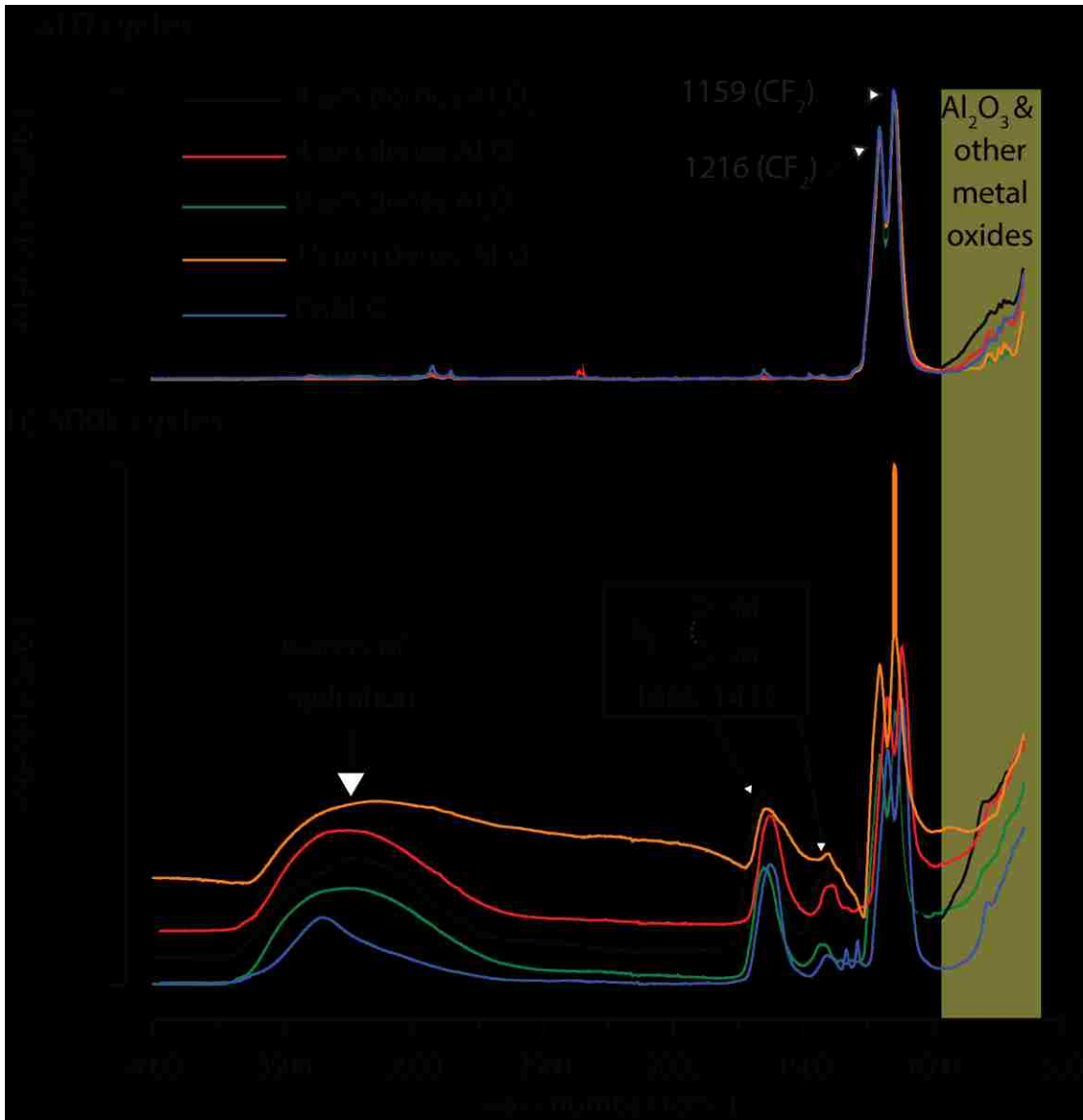


Figure 33: Attenuated total reflectance infrared spectra of various PTFE-Alumina particles before testing and after 500k sliding cycles (25km).

All tests showed that running films have similar chemical spectra attributed to ultralow wear PTFE alumina composites, mainly carboxylic salt endgroups (peaks at 1434 cm^{-1} and 1665 cm^{-1}) and waters of hydration (broad peak between $2900\text{-}3600\text{ cm}^{-1}$) [48]. Therefore, the chemical mechanism for formation of tribofilms found in ultralow wear PTFE-alumina systems requires more than just chemical composition. The mechanics of the particle itself play a critical role in preventing wear of these tribofilms, which will be highlighted in the following section .

5.5.4 Nanoindentation Results

The nanoindentation experimental setup is shown in Figure 34. Each prescribed loading curve included incremental unloading portions. This procedure was chosen to

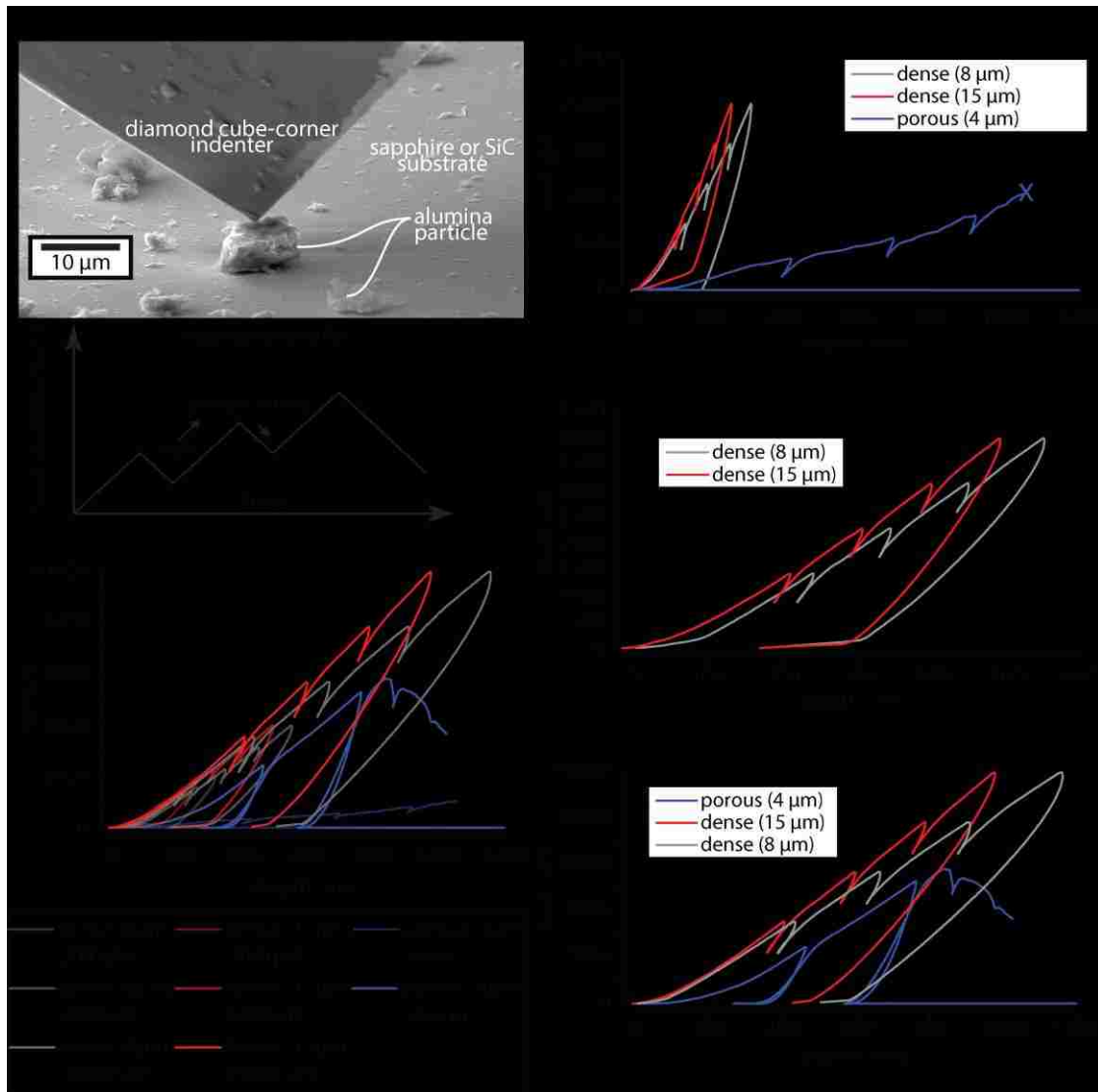


Figure 34: Summary of in-situ nanoindentation experiments. (a) experiment setup (b) all load vs displacement curves (c) load displacement curves for experiment with maximum load less than 2000 μN (d) all load indentation curves of experiments with less than 4000 μN maximum load (e) All loading curves for experiments with maximum loads of greater than 4000 μN .

allow for the hardness of the alumina particles to be evaluated as a function of depth. In the case of particle fracture, the incremental unloading curve would also serve to define the hardness of the particle before fracture [60]. It is clear from the force displacement curves, that the dense particles had steeper load and unload curves, signaling higher stiffness and modulus compared to the porous 4 μ m alumina particle. The compliance of the porous particles was quite extreme, especially in the “weak” porous particle which reached an indentation depth of over 1000 nm right before the particle fractured (Figure 34c). In comparison, the dense 8 and 15 μ m alumina particles were only at an indentation depth of 170 nm at the fracture load of the porous 4 μ m particle. The “strong” porous 4 μ m particle was significantly stiffer than the “weak” particle and not nearly as compliant. It was however still significantly more compliant than the dense 8 and 15 μ m alumina particles tested to the maximum 10,000 μ N load (Figure 34e). At the maximum load of the “strong” porous 4 μ m particle, the depth of indentation was at 800 nm, while the dense 8 μ m and 15 μ m alumina particles were at 700 and 600 nm of indentation depth respectively (Figure 34e). This decrease in stiffness of the porous 4 μ m particle clearly reinforces the hypothesis that particle porosity is critical in modifying the mechanical behavior of the alumina particles.

From the unloading sections of the force displacement curves, the hardness of each particle was determined, and these values are charted in Figure 35. The hardness of the dense 8 μ m particle ranged between 6-7 GPa, which is significantly lower than 100 percent dense alumina, which has a hardness of 25 GPa [65]. As the maximum force of the indent was increased on the 8 μ m dense alumina particle, the hardness values dropped compared

to the original 2,000 μ N maximum load indent. Similar observations were observed for the indents performed on the dense 15 μ m alumina particle with the maximum hardness values obtained corresponded to the 2,000 μ N experiment. The hardness of the 15 μ m alumina particles in this experiment ranged between 7-10 GPa. Hardness values for the porous 4

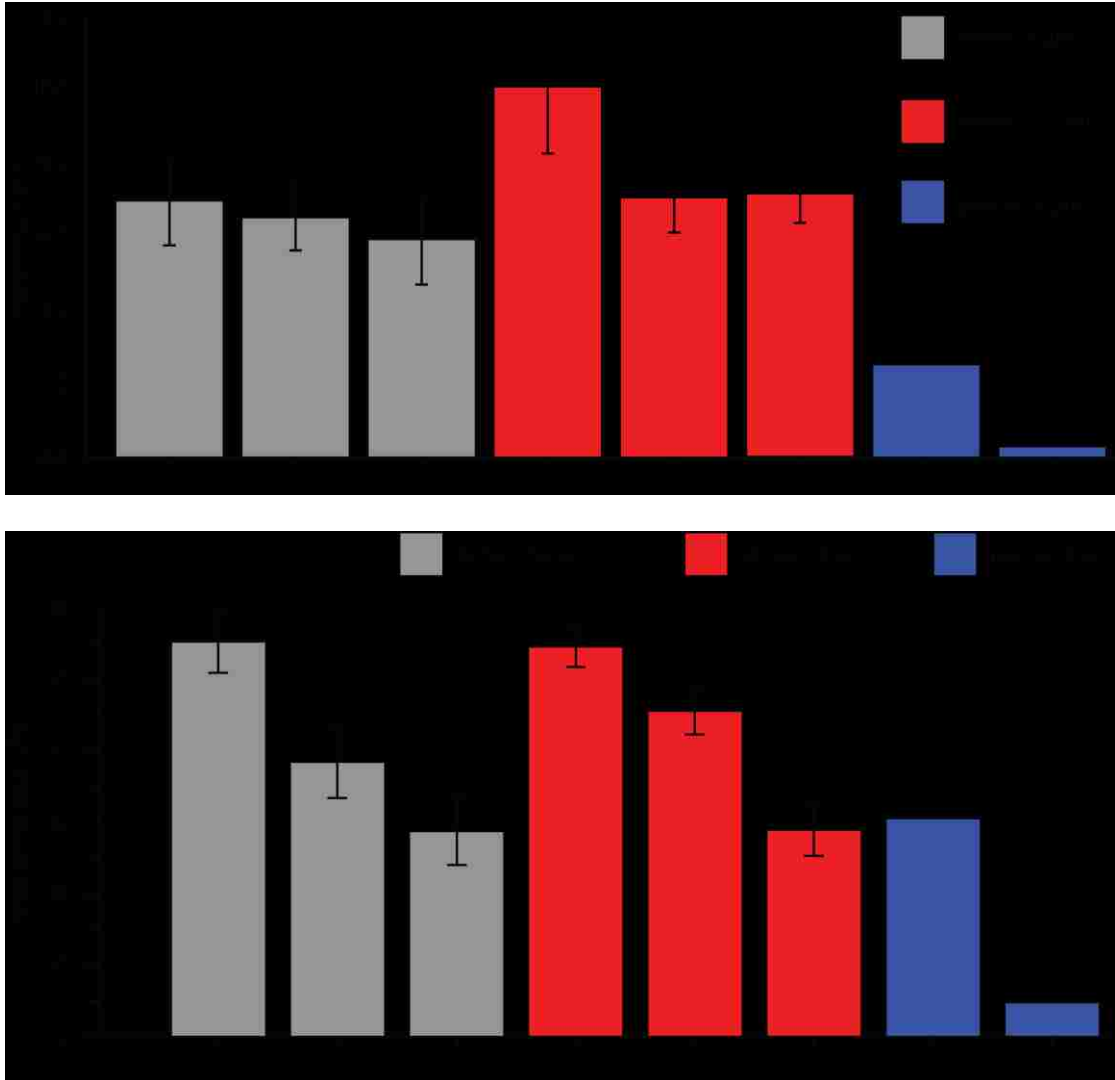


Figure 35: (Top) Hardness values for all indentation experiments. (Bottom) Reduced Modulus values for all indentation experiment. Error bars are due to the statistical scatter of the four unloading curves within each indent. The porous particles did not complete the prescribed loading cycle and the hardness values reported are just an average of the completed unloading curves.

μm alumina experiment were 0.31 GPa in the case of the “weak” 4 μm alumina particle and 2.5 GPa in the case of the “strong” porous 4 μm particle. These hardness values are well below the hardness values for the dense alumina particles. The porous 4 μm particle

hardnesses are close to the ~1 GPa hardness of the 304L SS countersample. The similarity or in some cases reduced hardness of the porous alumina filler particles compared to the countersurface would help prevent abrasive scratching and promote transfer film formation. Hardness of the alumina particles as a function of the maximum indentation depth is plotted in Figure 36. At higher indentation depths, the hardness is lower for all particles tested. The hardness of the porous 4 μ m strong particles are nearly 4 GPa less than the hardness values reported at similar indentation values. This indicates the greater amount of plastic strain these particles have withstood at that indentation depth.

Reduced modulus of the different alumina particles is shown in Figure 35. The reduced modulus of the “strong” alumina particle was similar (~30 GPa) with both the dense 8 μ m and 15 μ m alumina particles tested at 10,000 μ N load. The “weak” alumina particle was far softer, with a reduced modulus value ranging between 2.5-6 GPa. This stiffness is similar to the reported 2 GPa reduced modulus of the running film of the PTFE-porous 4 μ m composite [42]. It is likely that the mechanical properties of these filler particles likely follow a distribution and the density and size of each individual particle will vary. Metal-oxide particles with greater surface area to SLS particle size will likely have lower modulus and lower hardness values, and therefore be less abrasive than the dense, metal-oxide particles. The results of the nanoindentation study have confirmed this insight directly and supports the results of the tribological tests of the PTFE-metal-oxide composites.

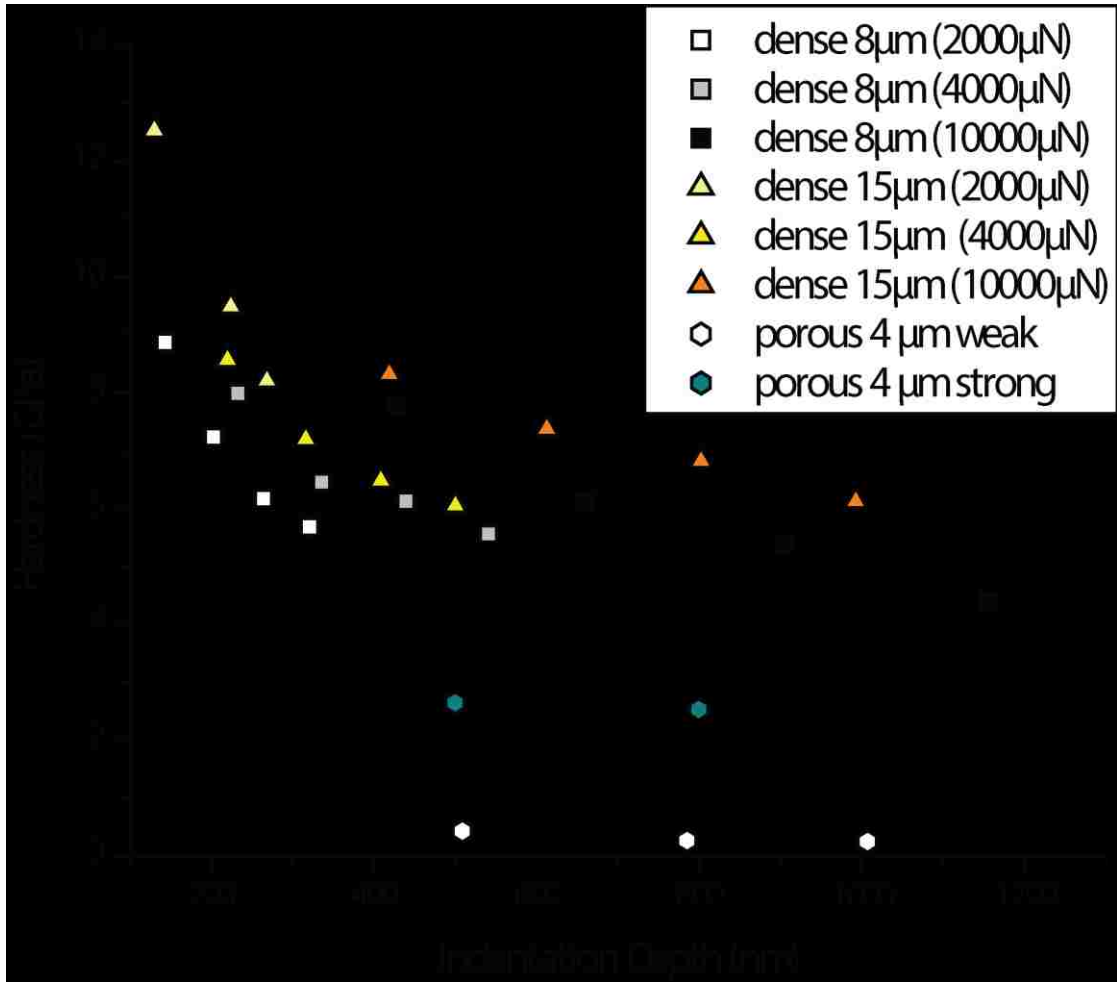


Figure 36: Alumina particle hardness as a function of maximum indentation depth. With increasing indentation depth, lower particle hardness was observed overall.

It is clear from the results of the tribological experiments with the indentation experiments that the mechanical behavior of the particle plays a large role in the tribological performance of the PTFE-alumina composite system. Porous alumina particles and cobalt aluminate particles composited with PTFE have shown consistently produced ultra-low wear rates ($K < 1 \times 10^{-7} \text{ mm}^3/\text{Nm}$) through the development of thin, robust

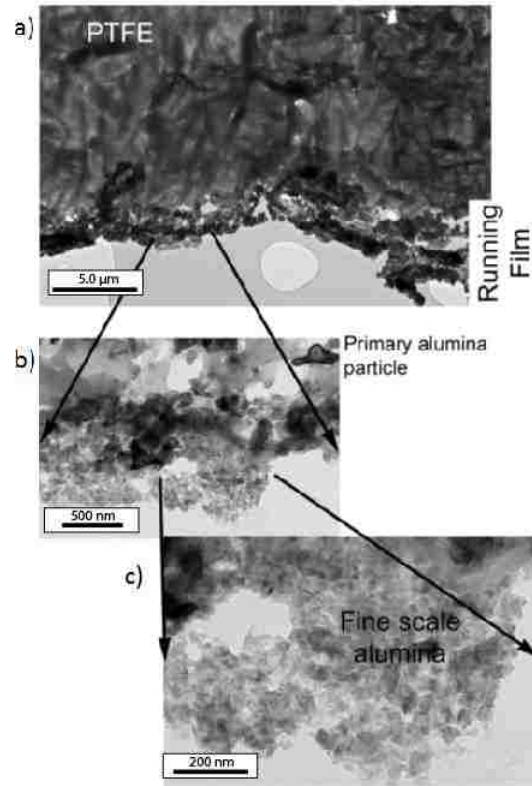


Figure 37 : TEM image of PTFE- Al_2O_3 composite surface (porous $4\ \mu\text{m}$). Reprinted with permission from [62]

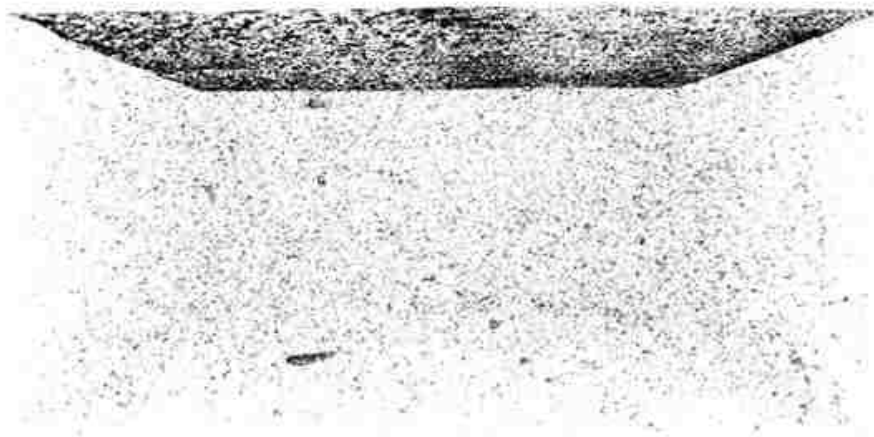


Figure 38: X-ray microtomography of PTFE- Al_2O_3 (porous $4\ \mu\text{m}$) micrograph after completion of all wear experiments. Reprinted with permission from [62].

tribofilms (Figure 32). In the 2016 study by Krick et. al, the authors investigated the effect

of particle size and surface area on wear of PTFE-alumina composite systems [62]. As part of this work, they prepared thin TEM sections of the PTFE-4 μ m porous alumina composite to evaluate the morphology of the running surface of the PTFE-alumina composite [62]. The near-surface region of the TEM specimen showed the build-up of nanometer sized alumina particles that are significantly smaller in size than the 4 micron average size estimated by static light scattering (Figure 37). From these results, the authors concluded that the stress near the sliding interface caused the larger porous particles to fracture into nano-sized fragments. Krick *et al.* also looked at the running film surface using an X-ray microtomography [62]. This technique can determine the distribution of alumina particles within the PTFE matrix. Near the sliding surface of the PTFE-alumina composites, there was a very high concentration of alumina particles compared to the bulk composite (Figure 38). From this observation along with TEM images, the authors concluded that the porous fillers likely break up under stress during the sliding and build up at the interface as additional sliding cycles are completed.

5.6 Conclusions

Through careful tribological, nanoindentation, and characterization methods the following conclusions about the PTFE-metal oxide composite system could be drawn:

1. The mechanical properties of the alumina particle directly correlate with the wear of the PTFE-alumina composite system, with softer alumina particles leading to wear rates as low as 5.8×10^{-8} mm³/Nm compared to the PTFE - dense

alumina composites which exhibited wear rates of $1.0\text{-}7.3 \times 10^{-8} \text{ mm}^3/\text{Nm}$ (Figure 30b).

2. Friction coefficient was lowest for the PTFE-4 μm porous alumina composites over the course of the experiment (Figure 30a).
3. The porous 4 μm alumina composites developed a smooth thin transfer film across the stainless steel countersurface while the PTFE-dense alumina composites exhibited patches of transfer film and deep abrasive scratches (Figure 32).
4. All three composite systems exhibited similar running film chemistry (carboxylic salts, waters of hydration, increased metal oxide signal) based of ATR-IR measurements despite distinct visual differences in appearance and large amounts of abraded stainless steel embedded into the PTFE-dense alumina composite materials (Figure 33).
5. Nanoindentation experiments revealed telling differences between the mechanical properties of the porous alumina particles compared to the dense particles. The hardness of the porous particle was similar in magnitude (0.3-2.5 GPa) to the stainless steel counterface (~ 1 GPa), while the dense alumina fillers were measured to have hardness values ranging between 6-10 GPa (Figure 35). This significant gap in hardness between the alumina filler and the steel counterface likely led to the abrasive scratches observed by scanning white light profilometry (Figure 32).

The role of the alumina filler particle in creating ultralow wear PTFE composite materials is visually summarized in Figure 39.

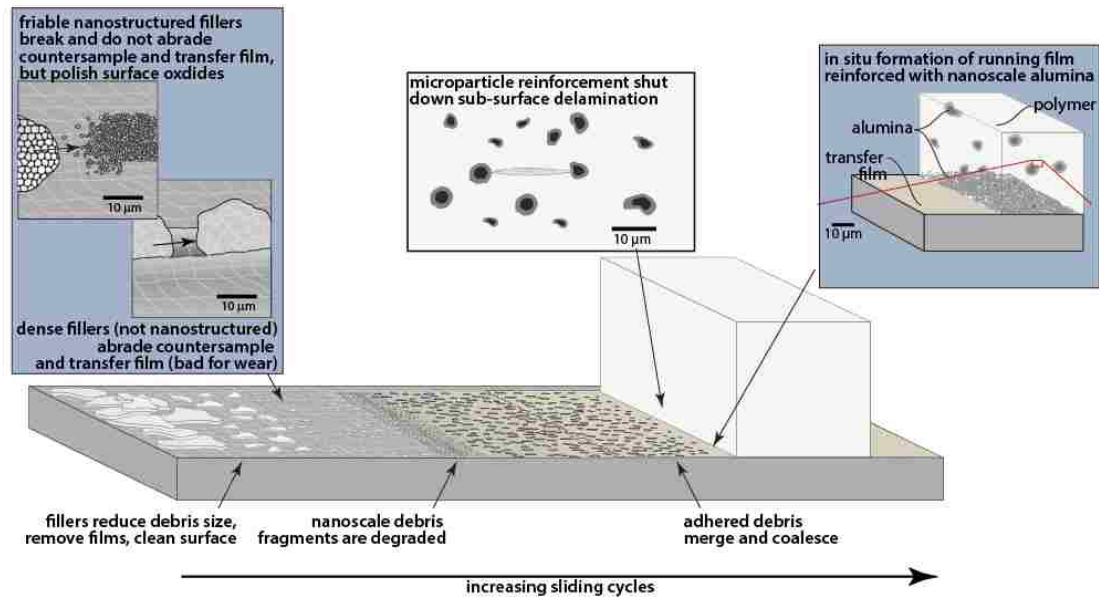


Figure 39: Visual framework for the role of alumina filler particles in reducing the wear of bulk PTFE and the formation of tribofilms.

Chapter 6: Ultralow Wear Melt Processible Fluoropolymer Alumina Composites

6.1 Overview

The addition of 1-10 wt. % of nanostructured alumina particles to PTFE has been repeatedly shown to reduce the wear of PTFE by four orders of magnitude. However, PTFE is limited by its near infinite melt viscosity, which prevents it from being melt processed like traditional thermoplastic materials. PFA, a random copolymer of tetrafluoroethylene and perfluorinated alkyl vinyl ether, shares a very similar chemical makeup to PTFE and maintains many of the desirable properties of PTFE (high temperature resistance, chemically inert, low friction). The great advantage of PFA over PTFE is its lower melt viscosity which allows it to be manufactured using screw injection molding. In this work, three grades of PFA were melt mixed with 5, 7.5, and 10 wt.% of nanostructured alumina particles and processed into plaques using a screw-injection molding apparatus. The wear and friction performance of PFA and PFA alumina composite systems was evaluated using a linear reciprocating tribometer at 6.25 MPa contact pressure, a sliding velocity of 50.8 mm/s, and a total sliding distance of 25.4 km. Results from the experiments showed a near four orders of magnitude decrease in wear rate of the PFA-alumina composite system from unfilled PFA with a reduction in friction coefficient compared to unfilled PFA. Friction and wear performance nearly matched that of PTFE-alumina composites during the final 200,000 cycles (~10km) of testing. Infrared spectroscopy revealed the presence of carboxylic salts on both the worn polymer composite surface and stainless steel

counterface. The tribochemical mechanism for the creation of protective tribofilms made of carboxylate salts that are responsible for the 10,000x reduction in wear is presented here.

6.2 Motivation

One of the great limitations of PTFE is its near infinite melt viscosity which limits the types of manufacturing methods that can be used. The near infinite melt viscosity of PTFE is due to its extremely high molecular weight, which can be lowered using a chain transfer agent [10]. However, at lower molecular weight, PTFE becomes incredibly crystalline which lowers the fatigue resistance PTFE drastically (§2.2). To counteract the limitations of low molecular weight PTFE, another class of fluoropolymers, perfluoroalkoxy polymers (PFAs) are commonly used. PFAs are a class of random comonomers of tetrafluoroethylene ($\text{CF}_2\text{-CF}_2$, TFE) and a minor quantity (typically less than 5 mol. %) of a perfluoroalkoxy vinyl ether (PAVE). Examples of typical PAVes used in PFA are methyl vinyl ether ($\text{CF}_2\text{-CFOCF}_3$), ethyl vinyl ether ($\text{CF}_2\text{-CF-OC}_2\text{F}_5$), and propyl vinyl ethers ($\text{CF}_2\text{-CFOC}_3\text{F}_7$). The molecular weight of PFA is controlled using a chain transfer agent, which improves its melt flow rate (MFR 14g/10min (PFA) vs 0g/10min (PTFE)), while the PAVE sidegroup prevents the highly crystalline state found in low molecular weight PTFEs that leads to poor fatigue failure resistance [11]. Though PFA has a larger friction coefficient than PTFE, its friction coefficient is still lower than many bulk polymers and has a very high operating temperature [21], [55].

PTFE- α -alumina composites have been shown to be 10,000x more wear resistant than virgin PTFE. The reasons for this massive wear reduction are highlighted in more

detail in §2.3.3. To quickly summarize, the reasons for the massive reduction in wear reduction are due to the following reasons:

- The tribochemical formation of robust transfer films and running films that improve mechanical properties at the interface [41], [43], [44], [46], [47], [50], [66].
- Properties of the alumina filler particle (size, shape, and dispersion) [39]–[41], [67].
- Countersurface roughness and directionality [41], [52].

In this chapter, the focus on formation and properties of tribofilms, which occur due to the breaking of the PTFE backbone during sliding [68], [69]. Once the PTFE backbone is broken, there is opportunity for tribochemical reactions to occur on the surface of the steel and polymer composite surface. Harris *et al.* provided a mechanistic hypothesis for these tribochemical reactions [48] (§2.3.3). Using infrared methods, Harris *et al.* identified carboxylic salt groups on the steel and PTFE composite Harris *et al.* claimed that during sliding the aforementioned chain scission provided opportunity for degradation of free radicals at the broken chain ends with O₂ and H₂O leading to carboxylic acid end groups. Carboxylic acid end groups like to chelate with metallic surfaces such as those found on the stainless steel counterface (Fe) and filler particles (Al). If similar ultralow wear in PFA-alumina composites occurs, PFA composites would serve as a melt processable viable alternative to PTFE alumina composites and would help these composites become more commercially viable.

6.3 Hypothesis

The chemical similarities of PTFE and PFA should also allow PFA with nanostructured α -alumina to establish similar reductions in wear rates as seen in PTFE- nanostructured α alumina composites. The tribochemical mechanisms outlined by Harris *et al.* would likely occur due to similar mechanical stress causing chain scission in PFA. The exposed carbon radicals would likely decompose in a similar way to PTFE with decomposition of reactions with O₂ and H₂O to form carboxylic acids, which would then bond to available metallic surfaces to form tribofilms. To evaluate this hypothesis, three grades PFA (340, 345, and 440) was composited with varying weight percentages of α -Alumina (0, 5, 7.5, and 10 wt.%). In the interest of brevity, the discussion will mostly focus PFA 340- α alumina composites.

6.4 Materials and Methods

6.4.1 Materials Tested and Sample Preparation

Compositions of all fluoropolymer alumina composites tested in this experiment are shown in Table 7. The relative differences between the various PFA resins used may be found in

Table 8. All PTFE samples were prepared using the methodology described in §4.1.1 and all PTFE samples were prepared using techniques described in section §4.1.2.

Table 7: List of PTFE and PFA resin types, alumina filler used, and amount of filler used in fluoropolymer composites experiments run in this chapter.

Matrix Type	Filler Type	Filler Percentages
Chemours Teflon® PTFE 7C	α -alumina, Nanostructured & Amorphous Materials (#1015WW)	Unfilled, 5 wt. %
Chemours Teflon® PFA 340	“”	Unfilled, 5, 7.5, and 10 wt. %
Chemours Teflon® PFA 345	“”	“”
Chemours Teflon® PFA 440	“”	“”

Table 8: Differences between the grades of Chemours ® PFA are listed in the table below:

Type of Chemours Teflon® PFA	Description	Pros	Cons
340	Standard PFA	High melt flow rate (easy to injection mold)	Lower fatigue reistance than PFA 345
345	High molecular weight (MW) vs 340 grade	Higher MW leads to added fatigue resistances	Melt flow rate is low, parts are harder to produce
440 HP	High purity PFA 340	Less reactive endgroups present	Purification of 340 resin increases cost

6.4.2 Tribometer

A linear reciprocating tribometer [70] (see §4.2.1) was used to evaluate wear and friction coefficient of the unfilled PTFE, unfilled PFA, PTFE-alumina, and PFA-alumina composite materials. All data acquisition and tribometer control was done through LabVIEW software (National Instruments, Austin Texas). All friction coefficient measurements reported here have uncertainties less than 0.005 [70]. During testing, the environment temperature and relative humidity were recorded. Normal and frictional forces applied to the polymer pin during sliding were measured using a six-axis load cell (AMTI MC3A-1000, Watertown MA).

6.4.3 Wear Rate Measurements

Wear rate measurements were performed using incremental mass measurements. The lost mass was converted to volume lost using the tested materials density (nominally 2.15g/cm^3). This volume loss was then divided by the average normal load and total sliding distance during the test duration to determine the wear rate. Further details on the methodology of wear rate measurements can be found in §4.2.3.

6.4.4 Experiment Conditions

All samples were tested at an applied load of either 50 or 250 N, which corresponds to contact pressures of 1.25 and 6.25 MPa respectively. The sliding velocity and stroke lengths were 50.8 mm/s and 25.4 mm respectively for all tests, which matches many past studies performed on PTFE and PTFE composite systems [43]–[45], [48]–[50], [54], [66], [71]. Tests were run until either the polymer pin failed due to excessive wear (Volume loss > 50 mm^3) or the sample slid for 25.4 km (500,000 cycles).

6.4.5 Infrared Spectroscopy

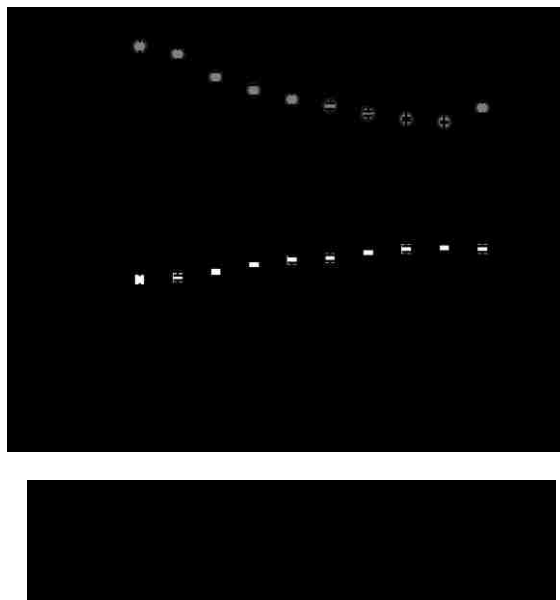
The importance of tribofilm chemistry in ultralow wear ($K < 5 \times 10^{-7} \text{mm}^3/\text{Nm}$) polymer composite systems has been recently highlighted by many authors [44], [48], [54], [72]. Two types of infrared (IR) spectroscopy were used in this study. Additional information on infrared spectroscopy may be found in §4.3.3.

- 1) Attenuated total reflectance IR- (Golden Gate (Specac) horizontal diamond ATR).
Used to characterize the surface of unworn and worn polymer composites.
- 2) Infrared Microscope- (Thermo Scientific Nicolet Continuum) – Used to measure the chemical composition of transfer films.

6.5 Results & Discussion

6.5.1 Tribological behavior

Unfilled PFA had significantly higher friction initially and on average (0.25 vs 0.14) than unfilled PTFE (Figure 40). This is likely due to the microstructural differences caused



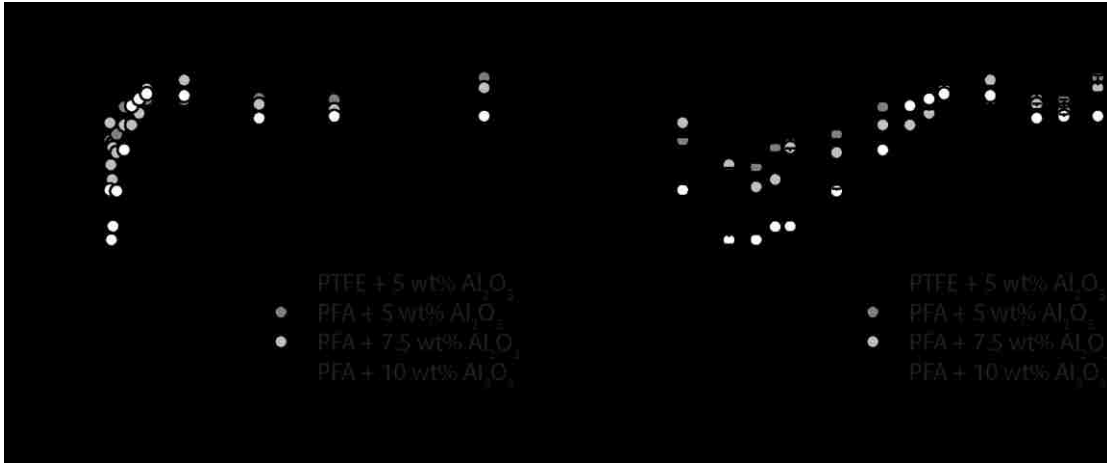


Figure 41: Friction coefficient versus sliding distance of PFA 340 with 5.0, 7.5, and 10.0 wt. % alumina, and PTFE with 5 wt. % alumina on linear (a) and semi-log (b) scales.

by the $-\text{OC}_3\text{F}_7$ sidegroup disrupting the smooth linear molecular profile and crystallization behavior of the polymer. Friction of filled PTFE and PFA α alumina composites is exhibited in Figure 41. Initial friction coefficient of filled PFA ranged between 0.2-0.24 compared to filled PTFE (0.16-0.18) during the first 250 m of sliding. Both PTFE and PFA composites exhibited a rise in friction coefficient during testing to a steady state value ranging between 0.23 and 0.26. This is truly surprising considering how widely different the friction coefficients of the unfilled PTFE & PFA samples tested were. This further supports our hypothesis that the running film and transfer film generated by both PTFE and PFA alumina composites are very similar.

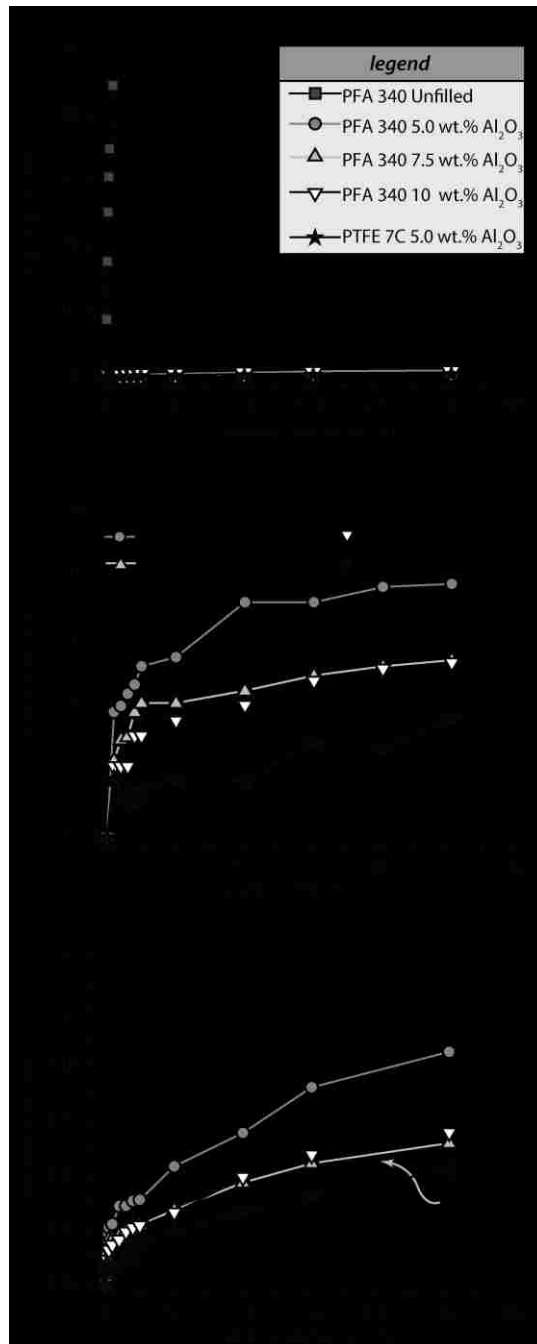
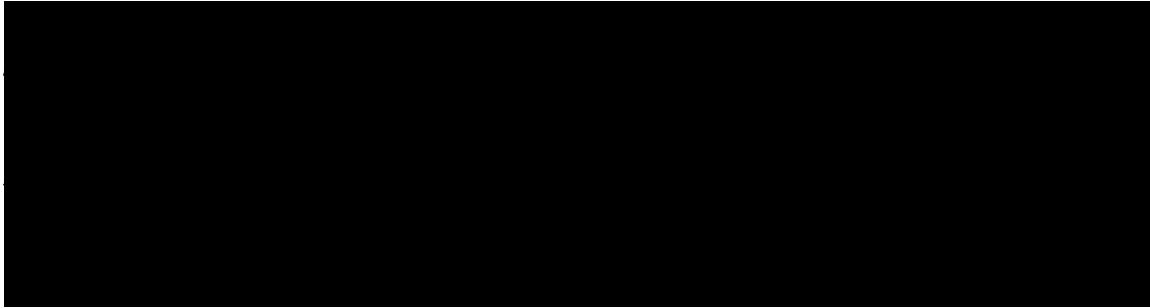


Figure 42: (a) Volume lost versus sliding distance for PFA 340 and PFA 340 Al₂O₃ composites. (b) Volume lost versus sliding distance for first 50,000 sliding cycles. (c) Volume lost versus sliding distance for entire 500,000 sliding cycle experiment [73].

The wear of unfilled PFA and PTFE composites is shown in Figure 42a. The wear of unfilled PTFE and PFA is drastically higher than the filled polymer systems tested. During the first 50m of sliding, (Figure 42b), the initial wear rates of the polymer composites were very high ($\sim 1 \times 10^{-5} \text{ mm}^3/\text{Nm}$) and reduced down to $\sim 5-10 \times 10^{-8} \text{ mm}^3/\text{Nm}$ after $\sim 2500\text{m}$. During the last 200,000 sliding cycles ($\sim 10\text{km}$), the wear rates of the PFA composites ranged between $4-7 \times 10^{-8} \text{ mm}^3/\text{Nm}$, which agrees with the reported range of PTFE- α -alumina composites [46], [50]. The wear rate and friction coefficient values for this study are tabulated below (Table 9).



wt. % Al ₂ O ₃	K _{initial} (mm ³ /Nm)	K _{final} (mm ³ /Nm)	μ _{initial}	μ _{final}	Relative Humidity (%)
Unfilled PFA 1	3.40E-04	6.70E-04	0.20	0.32	52.0
Unfilled PFA 2	6.60E-04	1.40E-04	0.29	0.24	25.7
5 (PTFE)	6.90E-06	4.40E-08	0.17	0.26	18.5
5.0	1.70E-05	6.80E-08	0.23	0.27	27.7
7.5	1.00E-05	4.00E-08	0.24	0.27	12.6
10	9.40E-06	4.30E-08	0.20	0.25	11.7

6.5.2 Effect of pressure, PFA grade, and filler percentage of unfilled versus filled PFA

During preliminary testing, two contact pressures of 1.25 MPa (Fn=50 N) and 6.25 MPa (Fn=250 N) were evaluated for every grade (e.g. 340, 345, and 440HP) and filler concentration (e.g. 0, 5, 7.5, 10 wt.%) of PFA-α Al₂O₃ composites (Figure 43). Unfilled

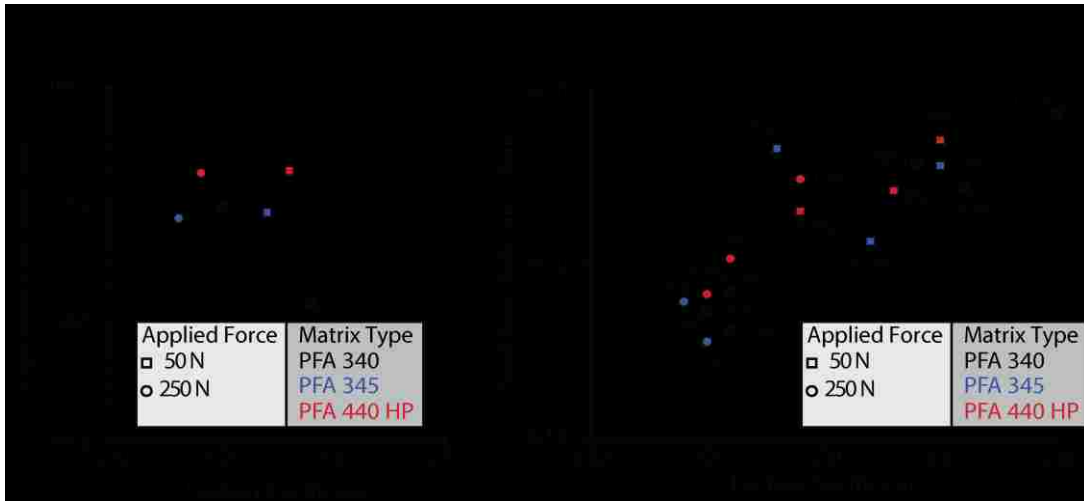


Figure 43: Effect of pressure, PFA grade, and filler weight percentage on friction and wear.

PFA tested at lower pressure had higher a higher average friction coefficient than PFA tested at higher pressure. Unfilled PTFE also exhibits the trend of decreasing friction coefficient with increasing contact pressure [16], [19], [30]. Filled PFA also showed a similar trend of increasing friction at lower contact pressure. On average, the addition of filler particles did lead to increased friction coefficient at both contact pressures, which is also seen in most PTFE composites [18], [23], [29], [36], but the relative increase compared to unfilled PFA is smaller than the increase exhibited in PTFE-alumina composites.

The effect of PFA grade is harder to discern than the trend in contact pressure. PFA 345 and PFA 345 Al₂O₃ composites had the lowest wear and friction coefficient at the higher contact pressure of any of the to the grades (340 & 440). It should be noted that while the PFA 345 samples outperformed the PFA 340 and 440 samples, all the grades of PFA showed a nearly four order of magnitude improvement at the 6.25 MPa pressure and at least a 1,000x improvement at the 1.25 contact pressure. The amount of filler added (5, 7.5, or 10 wt. %) to each PFA grade showed no clear trend in friction coefficient or wear rate.

6.5.3 Tribofilm morphology

Ultralow wear PFA- α Al₂O₃ composite running films and transfer films show many similar characteristics compared to ultralow wear PTFE- α Al₂O₃ composites. First, all alumina filled PFA samples showed no signs of large wear debris exhibited by both unfilled PTFE and PFA (Figure 44). Both PTFE and PFA alumina composites exhibit a brown discoloration on both the countersample and polymer test surface (Figure 44) [50]. Over the length of the experiment, the discoloration of these films dull in color. The transfer film

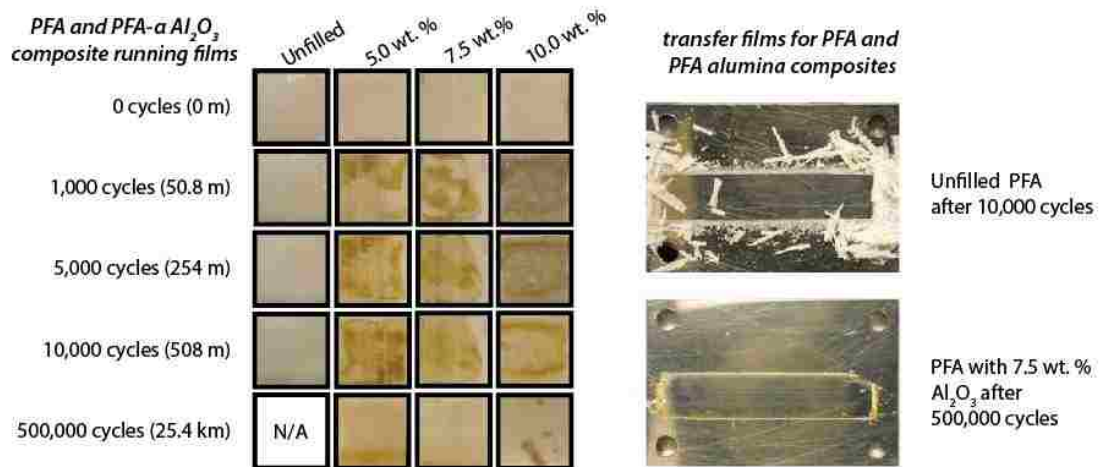


Figure 44: Tribofilms of PFA 340 and PFA 340 with Al_2O_3 [73].

developed on the metallic counterface was typically very thin (optically clear) with small, thicker patches of brown film. Wear debris at the end of the filled composites sliding stroke were significantly smaller in size than the unfilled samples (Figure 44). It should be emphasized that the wear debris accumulation for unfilled PFA shown in Figure 44, is only after 10,000 cycles while the wear debris shown for the PFA-7.5 wt.% Al_2O_3 sample was over 500,000 cycles. The drastic amount of additional wear debris present in the unfilled case despite sliding for fifty times less distance illustrates the near 10,000x in wear performance of these composites compared to the unfilled materials.

6.5.4 Tribofilm characterization (Infrared Spectroscopy)

There were significant differences in the infrared spectra of the worn tribofilms on the polymer composite (running film) (Figure 45a) and stainless-steel counterface (transfer films) after the tests were completed compared to the untested surfaces. Unfilled PFAs had nearly identical chemical spectra for worn and unworn surfaces (Figure 45a). The primary

peaks on the spectra were associated with CF_2 (1148 and 1204 cm^{-1}) and the CF_3 group part of the PAVE sidegroup (993 cm^{-1}). The unworn PFA Alumina composite shown similar chemical spectra to the unfilled PFAs except it also had a broad shoulder under 900 cm^{-1} corresponding to the metallic oxide region (likely the alumina filler). The worn surface of the PFA-Alumina composites showed peaks representing new chemical species. The most obvious peaks correspond to the two C-O stretches of pefluorocarboxylate salts (1434 and 1665 cm^{-1}) and the broad -OH stretches that correspond to waters of hydration between 3000 and 3500 cm^{-1} .

FTIR microscopy (in reflectance mode) of the countersurface of the 10 wt. % alumina PFA composite showed similar chemical spectra to that of the filled PFA composite testing surface (Figure 45b). The infrared bands corresponding to PFA (CF_2 -1148 and 1204 cm^{-1} , CF_3 -993 cm^{-1}), alumina (below 900 cm^{-1}), carboxylic salts (1434 and 1665 cm^{-1}), and waters of hydration are all present. This supports the hypothesis that wear debris from the PFA can bond to the surface of the metal countersample as well!

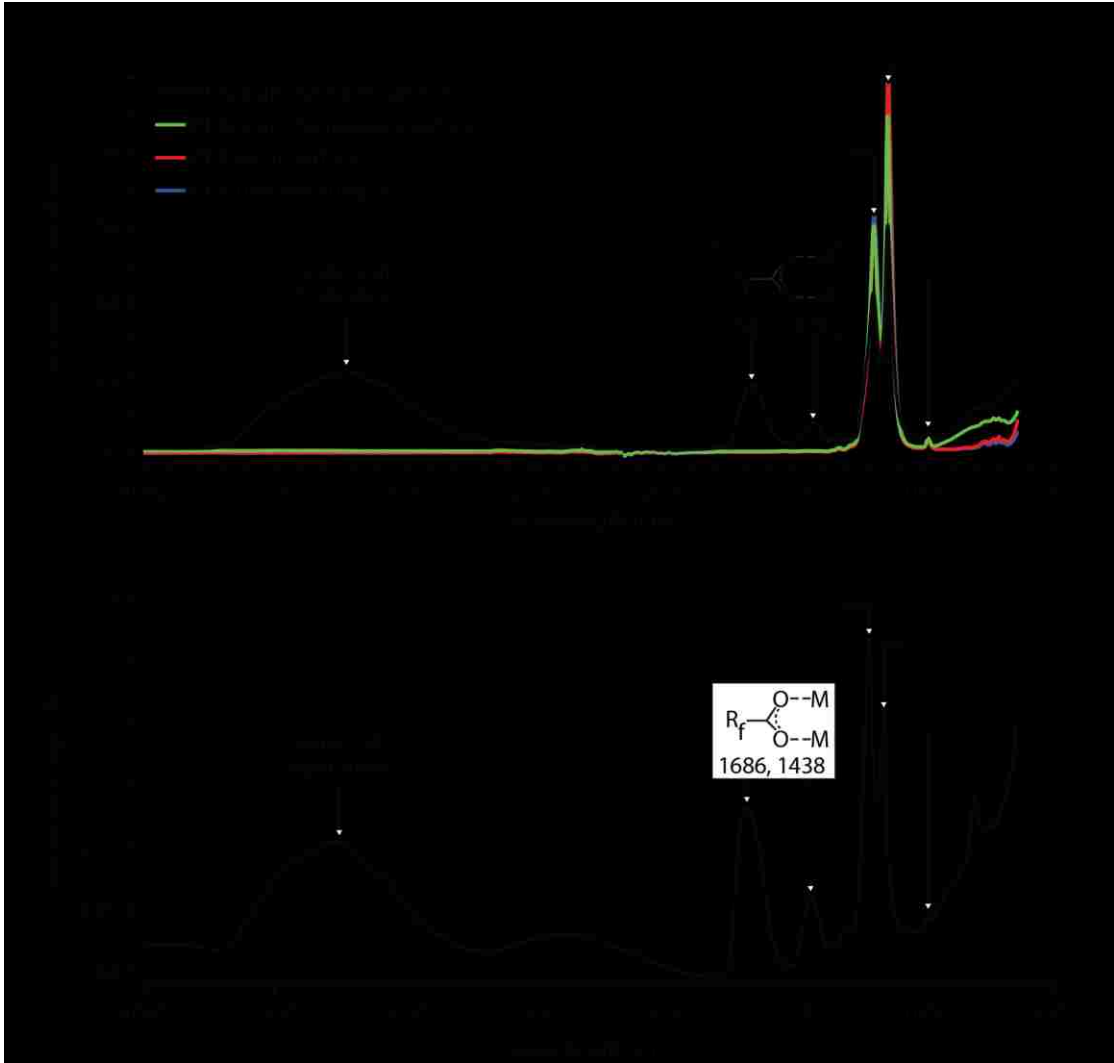


Figure 45: (a) ATR spectra of bulk and worn surfaces of PFA unfilled and PFA with 10 wt% Al_2O_3 . Note that the chemical differences are only truly noticeable between the worn PFA composite surface. All other surfaces tested have nearly identical chemical spectra. (b) FTIR spectrum of transfer film formed from sliding PFA with 10 wt. % Al_2O_3 on 304L stainless steel countersample [73].

6.5.5 Mechanistic Discussion

Due to the similar observance in frictional behavior (Figure 41), wear performance (Figure 42), tribofilms (Figure 44), and chemical spectra (Figure 45), the author is

confident the mechanism that reduces the wear rate in ultralow wear PTFE- α Al_2O_3 composites also applies to PFA- α Al_2O_3 composite tribosystems. This wear reduction and formation of tribofilms is a result of the tribochemical mechanism first outlined by Harris et al. in 2015 [48] and is outlined for PFA in Figure 46. This mechanism can be described as follows: 1) PFA undergoes chain scission during sliding and form perfluoroalkyl radicals at the chain ends, 2) These radicals react with O_2 from the atmosphere to form acyl fluoride end groups, 3) the acyl fluoride end groups hydrolyze in ambient humidity to form carboxylic acids 4) the perfluorinated carboxylic acids chelate to available metal surfaces (Fe in the counterface and Al in the composite). These bonds create a reinforced polymer network near the surface of the running film and transfer film that has exhibited improved mechanical properties [50], [53].

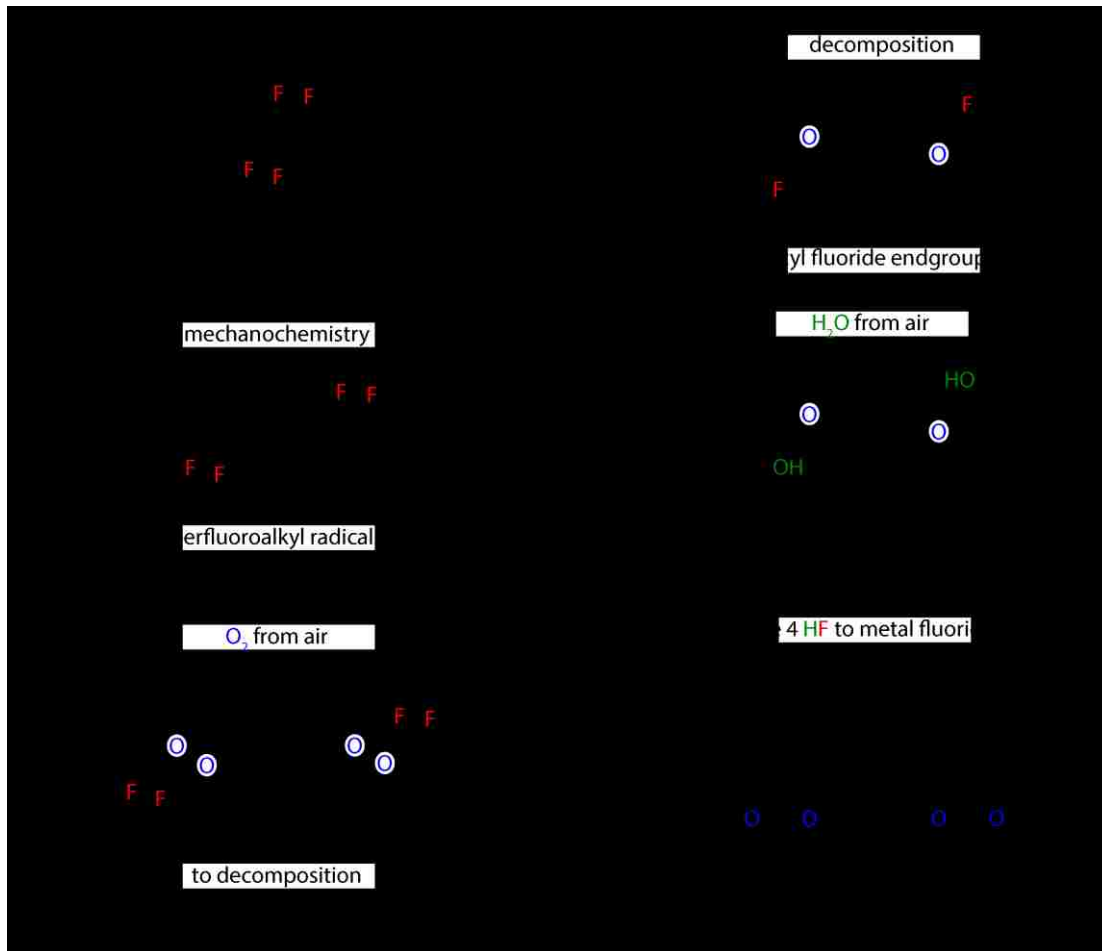


Figure 46: Tribochemical mechanism for formation of perfluorocarboxylate salts in PFA- α Alumina composites. R_f is the fluorinated end of the perfluorinated alkyl vinyl ether side group.

6.6 Conclusions

The addition of 4 μm porous α -alumina particles in concentrations ranging between 5-10 wt. % to PFA greatly reduced wear between 1,000-10,000x (Figure 42). Friction coefficient and wear rate steady state was surprisingly similar for PFA- α -alumina composites compared to PTFE- α -alumina composites, suggesting the surface chemistry is

similar for both (Figure 41, Figure 42). At lower contact pressures, the friction coefficient for unfilled and PFA α -alumina composites was larger (Figure 43). This agrees with similar trends seen in PTFE literature. Robust, persistent tribofilms developed on the surface of the polymer pin and metallic countersample in filled composites. PFA alumina composite wear debris was found to be significantly smaller in size than unfilled PFA (Figure 44). IR Spectroscopy confirmed presence of carboxylic salts and waters of hydration on both the running film and transfer film of PFA- α Al_2O_3 that are nearly identical to the tribofilms of PTFE- α Al_2O_3 (Figure 45). The above findings confirm that the tribochemical mechanism outlined by Harris *et al.* is valid for PFA- α alumina systems (Figure 46) and these tribofilms lead to tribological performance rivaling that of PTFE- α alumina with the improved melt processability of PFA!

Chapter 7: Effect of Sliding on Microstructure of PFA

7.1 Overview

The effects of sliding on the microstructure and chemistry of PFA are unknown. Coupled tribological experiments with differential scanning calorimetry (DSC), x-ray diffraction (XRD), and infrared spectroscopy characterization of bulk PFA and PFA wear debris were performed. The wear debris was found to transition from a triclinic to hexagonal crystalline structure at lower temperature and had increased crystallinity compared to the bulk material through DSC and XRD experiments. The increased crystallinity was likely due to alignment of molecules within the microstructure of PFA. Infrared spectroscopy revealed free carboxylic acid endgroups formed within the wear debris during sliding and chain scission was more prominent within the amorphous region. The presence of free carboxylic acid endgroups in the wear debris confirmed that stress during sliding reduced the molecular weight of PFA, which explained the improved crystallinity of the wear debris during the second melting endotherm. The reduction in molecular weight and increased crystallinity of the PFA wear debris are also found for unfilled PTFE and support the tribochemically driven mechanism for ultralow wear PFA- α alumina composites covered in §6.5.5.

7.2 Motivation

PFA has barely been studied in tribological applications [56], [73], which is odd considering how similar it is to PTFE in mechanical, thermal, and chemical properties. The most likely reason for the lack of tribological research on PFA is its relatively high cost

compared to PTFE (PFA is ~3x more expensive than PTFE). Recent experiments have shown that through the addition of certain 5-10 wt. % α -Al₂O₃ filler particles the wear of PFA nearly improved by 10,000x [73]. This massive improvement in wear performance highlights the need for better comprehension of how shear stress during sliding may affect the chemistry and microstructure of PFA. No previous studies on the effects of sliding on the microstructure of PFA have been reported to the best of the authors knowledge. Differential scanning calorimetry (DSC), infrared spectroscopy (IR), and X-ray diffraction (XRD) methods were used to characterize the running film, bulk, and wear debris of unfilled PFA. To evaluate the effects of comonomer type and concentration on melt behavior and chemistry of the wear debris, three grades of PFA were selected [Chemours ® PFA 440 HP (1.5 mol.% PPVE, melt flow rate (MFR)=16 g/10 min), Chemours ® PFA 416 HP (1.9 mol.% PPVE, MFR=42 g/10 min), Chemours ® PFA 950 HP Plus (3.4 mol.% PEVE, MFR=2 g/10 min)]. To provide the reader context on the microstructure and melt behavior of PFA, a brief summary of the literature will be provided in the following section.

7.2.1 Microstructure and Melt Behavior

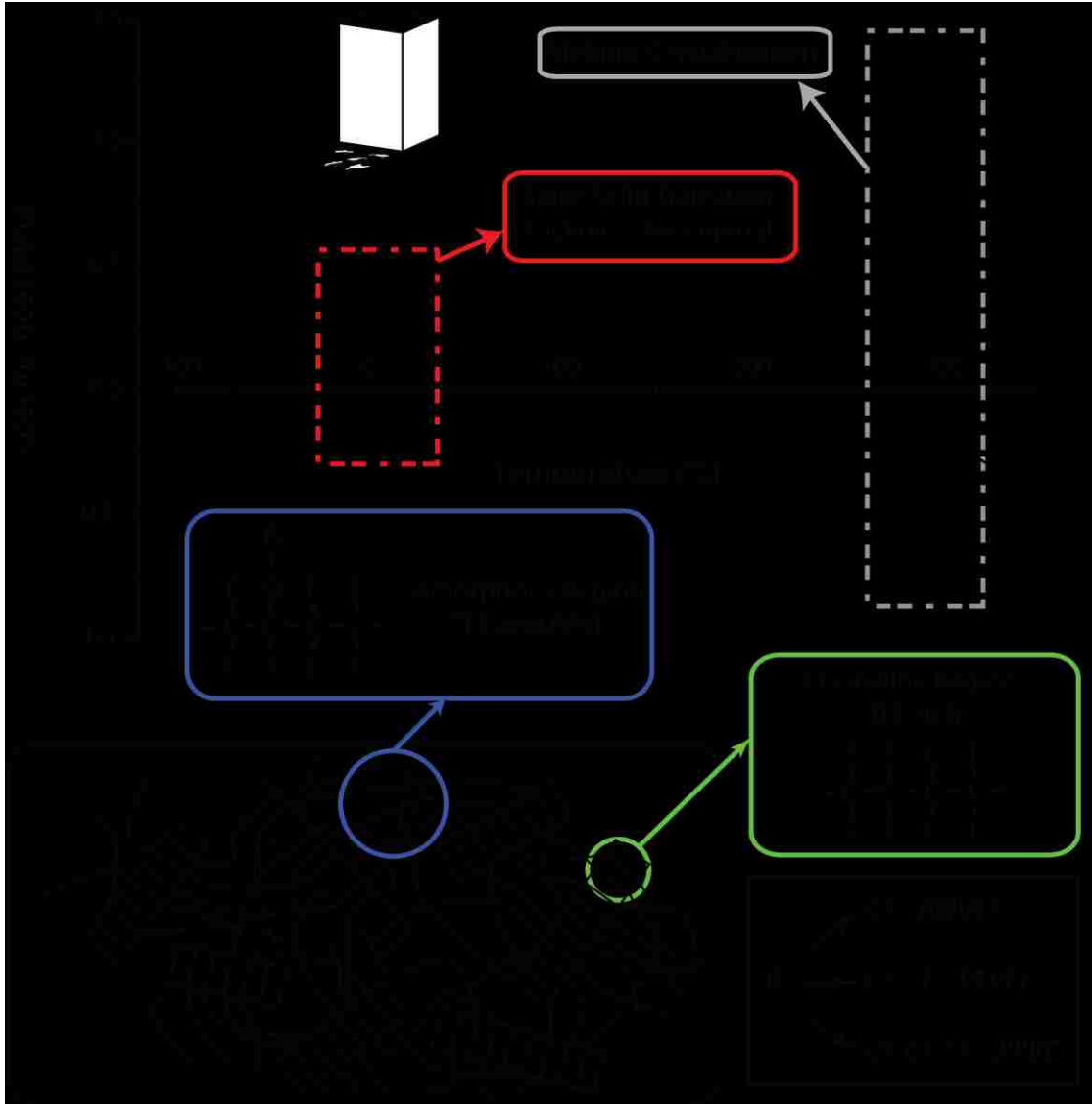


Figure 47: Typical DSC curves of PFA and microstructure schematic. The sub-ambient solid-solid transition is associated with the transition of PFA crystallites from a triclinic crystalline structure to a hexagonal crystalline structure at higher temperatures. Crystalline portions of PFA are composed of TFE rich sections and are represented in the DSC curves in the large melting endotherms in the high temperature region.

Like most polymers, PFA contains both amorphous and crystalline regions. The crystalline region of PFA's microstructure contains long, continuous runs of TFE portions with smaller sections of PAVE present. There is a statistical distribution of PAVEs that create a distribution of crystallite sizes based off the length of uninterrupted TFE runs. These crystalline regions form a similar crystalline arrangement to PTFE, which forms hexagonal, lamellar crystallites when cooling from the melt [13]. A study by *Puccariello* evaluated the melt behavior of PFA polymers with different amounts/types of PAVE [74]. PFA crystallites melt between 280-328°C [74] (Figure 47). The enthalpy of this melting peak may be used to determine the crystallinity of PFA. The enthalpy of the primary melting peak is very dependent on comonomer concentration as high concentrations lower crystallinity significantly (2 mol.% PAVE=27% crystalline, 10 mol.% 2.6 %) [74]. At higher PAVE concentration, the main melting temperature decreased (308 °C 2 mol. % PMVE, 224°C, 10 mol.% PMVE) [74]. The length of the PAVE sidechain had little effect on crystalline behavior as PMVE, PEVE, and PPVE comonomers at 2 mol% had nearly identical melt and crystallization temperatures. In the main melting peak there is often an observed secondary melt at higher temperatures. This is associated with a small fraction of crystallites with longer runs of TFE present [75].

The amorphous region within PFA has been reported to have small "interlamellar" crystals (short runs of aligned TFE) by *Fujimori et al.* [13]. The sub-ambient peak in DSC endotherms is typically observed between -10-10 °C. This peak represents the solid-solid transition of the PFA crystallite from a triclinic crystalline structure below this peak to a hexagonal crystallite structure above it [76]–[78]. With increasing concentration of

comonomer, this transition is reduced in magnitude and melt temperature. This sub-ambient melt is barely observed in the PAVE concentrations greater than 4 mol. % (2 mol. % -5°C, 4 mol. % -7.1 °C, 6,8,10 mol. % PAVE= peak not observed) [74]. Many studies have reported the melting behavior of PFA but very few authors comment, measure, or even mention the existence of this sub-ambient melt [13], [75], [79]–[83].

7.3 Hypothesis

Though the effects of sliding on PFA are relatively unknown, the effects of sliding on unfilled PTFE have been widely studied [18]–[20], [23], [84], [85]. There are two major phenomenon that occur within microstructure of PTFE during sliding. The first observed change in PTFE's microstructure during sliding is the increase in crystallinity of the wear debris. In a paper written by *Khedkar et al.*, the enthalpy of PTFE wear debris increased from 18.0 J/g in the bulk sample to 39.5 J/g for ejected wear debris [86]. The second consequence of shear stress is the chain scission of the polymer backbone leading to reduced molecular weight of the wear debris. *Arkles and Schireson* estimated the molecular weight of PTFE from greater than 1×10^8 g/mol in bulk PTFE to 2.8×10^5 g/mol in the wear debris of unfilled PTFE and less than 10,000 g/mol in filled PTFE composites [87]. Similar behavior (reduction in molecular weight and increased crystallinity of the wear debris) is expected in unfilled PFA during wear.

7.4 Materials and Methods

7.4.1 Materials Used

Three grades of PFA were selected for use in this study. All were prepared using the conditions mention in §4.1.2. Relevant properties for each of the PFA resins used is presented in Table 10.

Table 10: Different grades of PFA used for tribological tests. PPVE= $CF_2CFOC_3F_7$, PEVE= $CF_2CFOC_2F_5$. Melt flow rate is a crude approximation for molecular weight (lower molecular weight fluoropolymer flow easier and typically crystallize easier than high molecular weight fluoropolymers).

PFA Grade	Comonomer	Mol. % Comonomer	Melt Flow Rate (g/10 min)[88]
416 HP	PPVE	1.9	42
440 HP	PPVE	1.5	16
950 HP Plus	PEVE	3.4	2

7.4.2 Tribological Testing

Testing was performed on a linear reciprocating tribometer. Two contact pressures (1.25 MPa and 6.25 MPA) and one sliding velocity (50.8 mm/s) were used. The counterface material was a lapped 304L stainless steel coupon. All experiments were performed in laboratory air. Friction coefficients and wear rates of PFA will not be reported here but may be found in the literature [55], [73], [89]. More details on tribological testing are outlined in §4.2 and in methods papers by *Schmitz et al.* and *Burris et al.* [57], [70].

7.4.3 Differential Scanning Calorimetry

A Q1000 Differential Scanning Calorimeter (TA Instrument, New Castle DE) was used to evaluate melt behavior of the bulk polymer and wear debris. The DSC cycle followed this procedure: 1) samples were chilled to -50°C at $10^{\circ}\text{C}/\text{min}$ and held at -50°C for three minutes. 2) Specimens were then heated at $10^{\circ}\text{C}/\text{min}$ up to 350°C . 3) Once reaching 350°C , the samples were held for three minutes and then cooled to -50°C at $10^{\circ}\text{C}/\text{min}$. 4) After another three-minute hold at -50°C the samples were again heated to 350°C at a rate of 10°C to complete testing. To calculate the percent crystallinity, the enthalpy of the high temperature melting peak was divided by the heat of fusion for 100% crystalline PTFE, 82 J/g [13], [83] (Equation 4).

$$\text{Equation 4: \% Crystallinity} = \frac{\Delta H_{exp}}{\Delta H_{ideal}} \times 100\%$$

7.4.4 X-Ray Diffraction

1.5 mol.% PPVE PFA samples from both bulk polymer and wear debris were evaluated. A PANalytical (Almelo, Netherlands) X'pert θ - θ diffractometer in reflection geometry was used with $\text{Cu K}\alpha$ radiation. A mirror with Pixcel detector set to a one degree window, a $1/8^{\circ}$ anti-scatter slit, a $1/16^{\circ}$ defining slit, and a pulse height discriminator were used for these measurements. A silicon wafer that was cut off axis to minimize scattering effects was used to mount the samples. The mounted wafer was spun at 2 rev/s about the vertical axis during measurement. The range of data collection was from 2θ 5° - 30° in steps of 0.025° and each scan lasted for three hours. Bragg's Law (Equation 5: $d = \frac{n\lambda}{2 \sin \theta}$) and the Scherrer's Formula (Equation 6) were used to determine the interatomic

spacing (d) and mean crystallite size (D) of the two samples. ($\lambda=0.154$ nm, θ = maximum peak height location in radians, B = Full-Width-Half-Maximum (FWHM) of peak, in radians, n =integer, typically 1).

$$\text{Equation 5: } d = \frac{n\lambda}{2 \sin \theta}$$

$$\text{Equation 6: } D = \frac{K\lambda}{B \sin \theta}$$

7.4.5 Transmission Infrared Spectroscopy

Wear debris and bulk samples of 1.5 mol.% PPVE were evaluated using a Nicolet is10 Infrared Spectrometer (Thermo Fisher Scientific, Waltham MA) that was scanned from 400-4000 cm^{-1} . Each spectrum was an average of 32 scans. The bulk sample was made by cutting a thin slice ($\sim 830\mu\text{m}$) of the unworn edge of the test specimen using a water-cooled diamond saw. Wear debris ejected from the sample during sliding was collected and formed into a thin disc ($\sim 430\mu\text{m}$) using a bolt press.

7.4.6 Attenuated Total Reflectance Infrared (ATR-IR)

A Spectrum 1000 Infrared Spectrometer (Perkin Elmer, Waltham, MA) was used to evaluate wear debris, running film, and bulk PFA 1.5 mol.% PPVE samples. Three spectra were recorded for each sample type (bulk, wear debris, and running film) to reduce scattering error (# scans/spectra=16). The absorbance peaks associated with CF_2 (1075-1300 cm^{-1} , present in TFE and PAVE) and CF_3 (950-1025 cm^{-1} , PAVE only) were numerically integrated using Trapezoidal Rule. The ratio between the CF_2 and CF_3 peaks was calculated to determine the relative amounts of TFE and PAVE in each sample. A

Table 11: DSC data for the solid-solid transition for all PFA grades tested (bulk and wear debris) for the primary melt.

		1.5 mol.% PPVE		1.9 mol. % PPVE		3.4 mol. % PEVE	
		Bulk	Wear Debris	Bulk	Wear Debris	Bulk	Wear Debris
1st Heat	Peak (FWHM), (°)	2.5 (10.2)	-25.5 (31.9)	0.3 (10.3)	-26.7 (21.6)	-6.2 (14.5)	-29.7 (34.6)
	Enthalpy (J/g)	3.8	1.6	2.64	0.94	2.05	2.97
Cooling	Peak (FWHM), (°)	0.7 (9.5)	2.1 (12.5)	0.41 (6.4)	0.38 (11.9)	-7.5 (16.5)	-7 (15.3)
	Enthalpy (J/g)	4.6	5.4	4.28	3.68	2.22	2.44
2nd Heat	Peak (FWHM), (°)	5.3 (8.1)	7.6 (12.2)	4.5 (7.4)	5.1 (12.5)	-3.3 (17.5)	-2.8 (17.3)
	Enthalpy (J/g)	4.7	4.7	4.59	4.4	2.67	3.26

higher amount of TFE present would correspond to a higher CF₂/CF₃ ratio while a small CF₂/CF₃ ratio would indicate a larger amount of PAVE.

7.5 Results and Discussion

The first melting endotherms for bulk and wear debris samples of PFA (1.5 mol. % PPVE) are shown in Figure 48a (DSC results are shown in Table 12 and Table 11 as well). The wear debris peak in the sub -ambient region is at significantly lower temperature (-25.5 °C vs 2.5°C) than the bulk sample. The wear debris peak at sub-ambient temperature is also significantly broader than the bulk PFA peak (FWHM 31.9 °C vs 10.2°C). The lower melt point and broader curve of the PFA wear debris implies that the crystal structure

Table 12: DSC data for all PFA grades tested (bulk and wear debris) for the primary melt.

		1.5 mol.% PPVE		1.9 mol. % PPVE		3.4 mol. % PEVE	
		Bulk	Wear Debris	Bulk	Wear Debris	Bulk	Wear Debris
1st Heat	Peak (FWHM), (°)	307.8 (10.2)	311.7 (9.1)	308.9 (20.6)	310.6 (16.4)	299.2 (43.5)	305.1 (20.9)
	Enthalpy (J/g)	37.3	44.9	58.7	60.1	47.1	61.7
	% Crystallinity	45.5	54.8	71.6	73.3	57.4	75.2
Cooling	Peak (FWHM), (°)	286.5 (3.1)	290 (4.5)	289.4 (4.0)	289.4 (4.9)	277.2 (4.7)	276.9 (5.2)
	Enthalpy (J/g)	41	42.9	46	63.1	54.1	55.6
2nd Heat	Peak (FWHM), (°)	308.7 (7.8)	310 (10.0)	312(15.3)	311.9 (16.3)	303.5 (75.6)	303.4 (113.4)
	Enthalpy (J/g)	38.5	42.4	54.3	62.5	54.9	61.3
	% Crystallinity	46.95	51.71	66.22	76.22	66.95	74.76

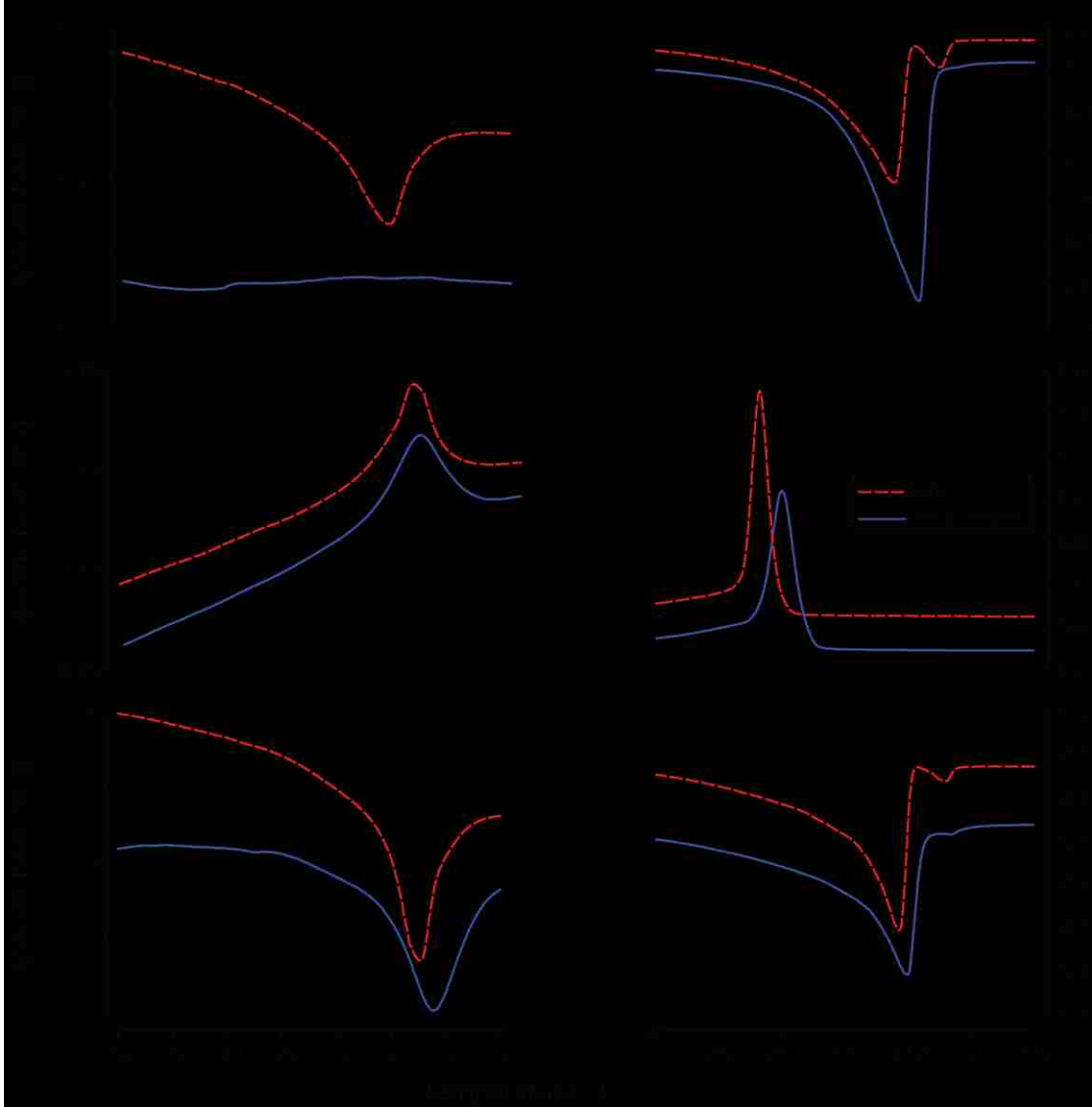


Figure 48: DSC curves of the first, heat, crystallization and second heat of PFA 440 (1.5 mol.% PPVE) and its wear debris.

favors the hexagonal state. For the primary melt, the bulk endotherm is smaller than the wear debris melting endotherm (44.9 J/g vs 37.3 J/g), which implies increased crystallization within the wear debris. These crystallites were likely larger in size as well which was shown by the main melting peak temperature exhibiting an increase in

temperature in the wear debris versus the bulk sample (311.7°C and 307.8°C) . The secondary melting peak in the primary melt of the wear debris has merged with the main melting peak, which is clearly exhibited by PFAs with 1.9 mol.% PPVE (Figure 49a) and 3.4 mol.% PEVE (Figure 50a). This is due to a shift in the size of the PFA crystallites in the wear debris. All tested grades showed an increase in crystallinity (2.4-31%) in the wear debris compared to the bulk sample (Table 12).

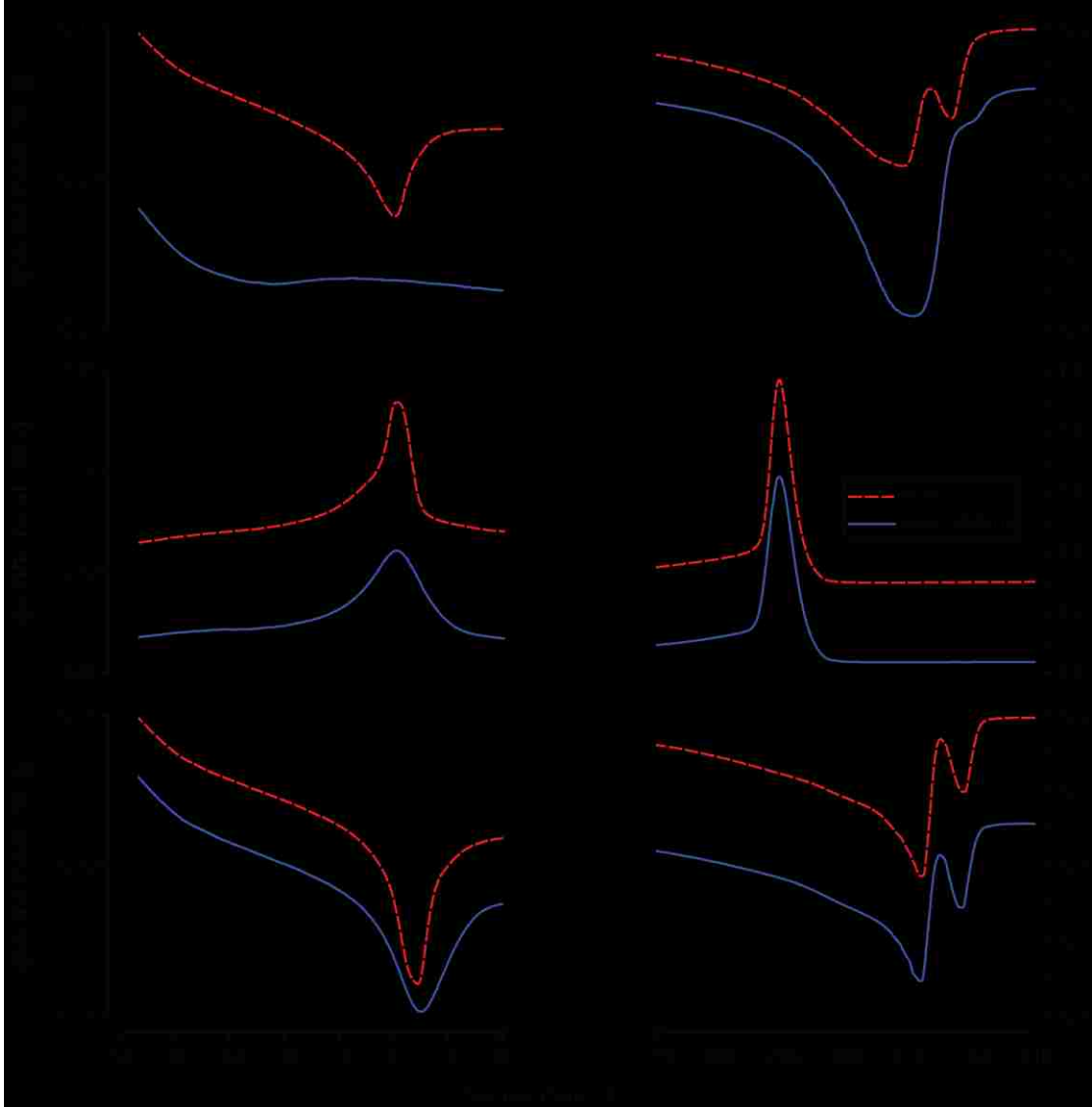


Figure 49: DSC curves of the first, heat, crystallization and second heat of PFA 416 (1.9 mol.% PPVE) and its wear debris.

These changes in the melt behavior of PFA point to structural changes in the microstructure of PFA during sliding. Two phenomena are possible reasons for these observed changes in the wear debris compared to the bulk. Frictional heating is one mode for significant change of microstructure the wear debris. A large thermal flux driving the

changes of the microstructure of PFA is unlikely to occur in this case because the sliding velocity is low and the conductive path out of the contact zone is very beneficial due to a large conductive heat sink underneath the stainless-steel counterface. It is estimated that the temperature rise at this interface would be less than 1°C [48], [90]. Since the

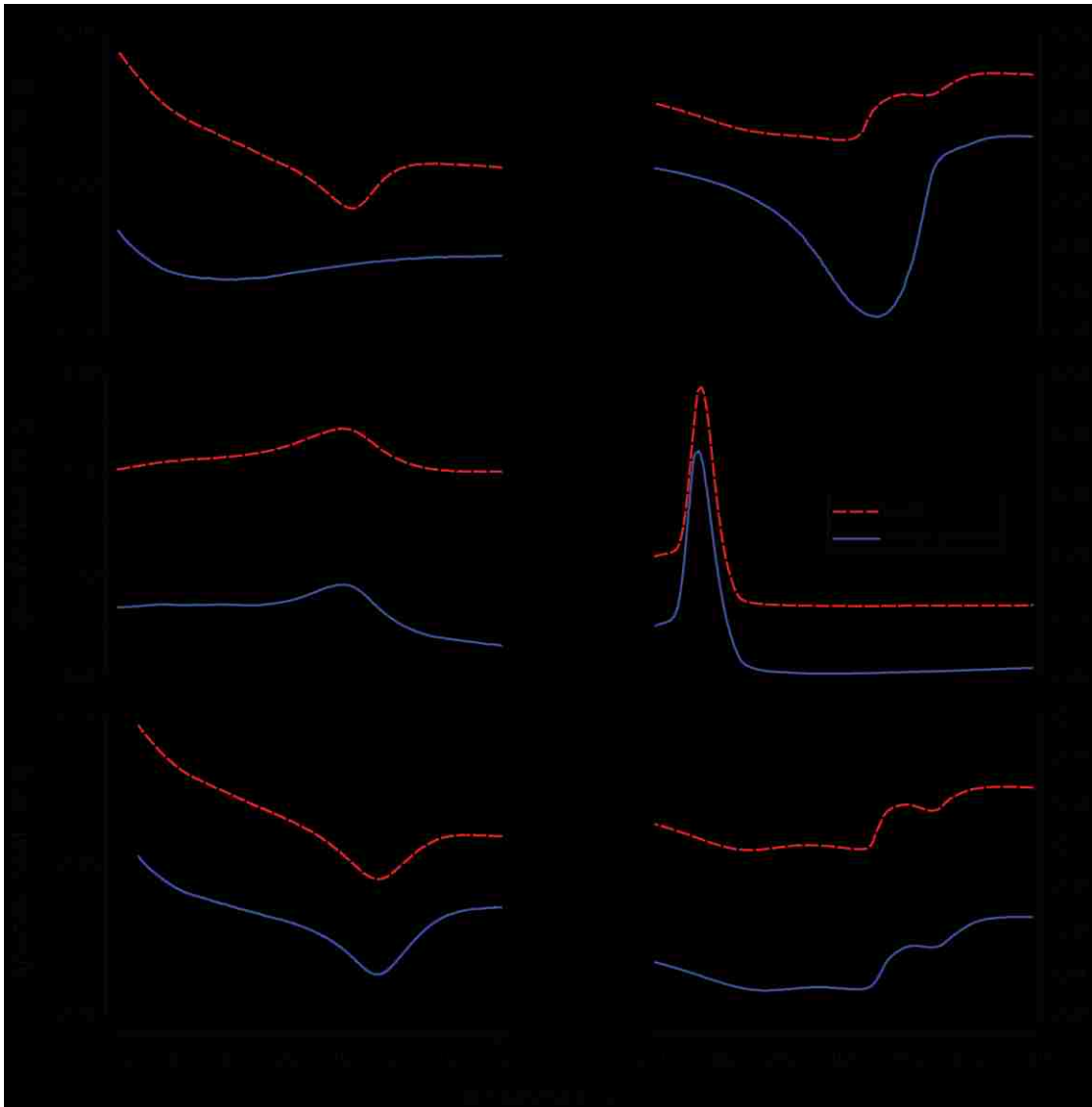


Figure 50: DSC curves of the first, heat, crystallization and second heat of PFA 950 (3.4 mol.% PEVE) and its wear debris.

temperature rise is minimal at the interface, the more likely cause of the observed changes in DSC endotherms is strain-induced crystallization an rearrangement of the microstructure. The shift and broadening of the low temperature endotherms signals that the PFA microstructure resists the phase transition from the hexagonal phase to the triclinic phat that typically occurs near 0°C (Figure 48a, Figure 49a, Figure 50a).

The mechanism behind strain-induced crystallization is due to molecular rearrangement within the microstructure of PFA. This causes the longer runs of TFE to align, which increases crystallinity exhibited by the increase in temperature and enthalpy of the main melting peak (Table 11). The increase in average crystallite size may also contribute to the merge of the main and secondary melting peaks (Figure 48b, Figure 49b, Figure 50b). The study on melt behavior of PFA by *Pucciariello* noted that as comonomer content increases, the lower melting temperature and main melting peak was suppressed [74]. This is due to the shortened length of TFE runs in the comonomer backbone inhibits crystallization [74]. This is not the case observed in the wear debris because the length of TFE segments between comonomer groups is set during polymerization and cannot be changed due to stress. The only way the concentration of comonomer could increase is due to preferential breakage near the comonomer in the PFA backbone. Even if this occurs, this would affect both the first and second sub-ambient solid- solid transitions since the shear stress was applied to PFA before both DSC endotherms were evaluated. Therefore, the reduction of the sub-ambient solid-solid phase transition cannot be due to increase in comonomer content and is likely due to the microstructural rearrangement of the PFA crystallites.

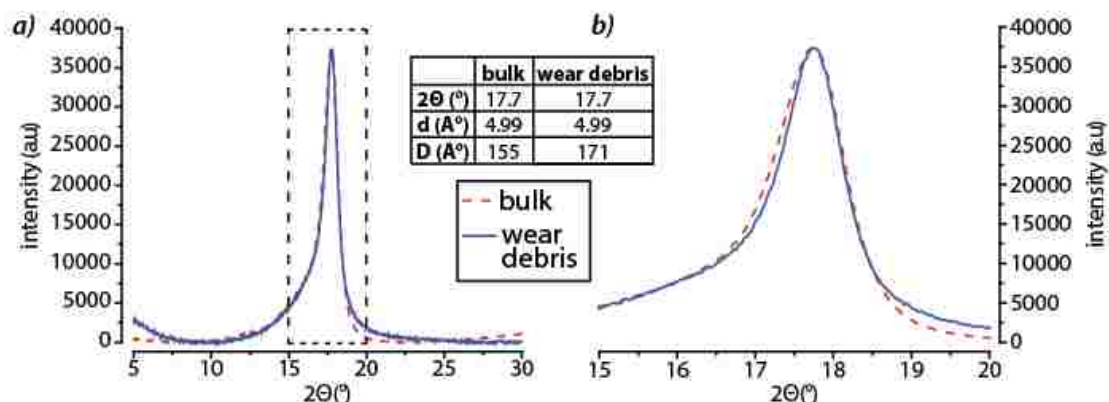


Figure 51: XRD data for PFA (1.5 mol. % PPVE) bulk and wear debris. Reduced FWHM of the wear debris sample correlates with a larger apparent crystallite size (D).

Wide Angle X-ray Scattering (WAXS) was used to independently confirm crystallographic changes observed by DSC for 1.5 mol. % PPVE wear debris and bulk (Figure 51). The maximum intensity for both wear debris and bulk samples near $2\theta=17.7^\circ$, which agrees well with XRD measurements by *Fujimori et al.* [13]. Interatomic spacing for both samples was found to be (4.99 Å, Equation 5). The Scherrer's formula (Equation 6) may be used to determine the apparent crystallite size of both samples. The FWHM of the wear debris peak was smaller than the bulk material (Figure 51), which corresponds to a larger crystallite size (wear debris 171 Å, Bulk 155 Å). The increased crystallite size observed by WAXS agrees with the increase in melting temperature for the wear debris (Figure 48b, Figure 49b, Figure 50b).

Mechanical stress has been shown previously to increase the crystallinity of PFA by *Runt et al.* and *Fujimori et al.* [83], [91]. In both studies, PFA films (PEVE=Fujimori, PPVE=Runt) were drawn to nine times their original length at elevated temperatures

(Runt=140°C, 200°C, Fujimori= 280°C). In the work by *Runt et al.* the increase in crystallites was observed at stress levels near 6.5 MPa, which is the contact stress used in these sliding experiments (6.25 MPa). During sliding there are locations of higher local stress due to asperities on the surface the stainless steel countersample. These local areas of higher stress would cause additional strain induced crystallization. Local, higher contact stresses at the sliding surface is supported by DSC results of wear debris tested at 1.25 MPa exhibiting higher enthalpy compared to the bulk material. Increased crystallinity and crystalline alignment were observed by both *Fujimori et al.* and *Runt et al.* through X-ray diffraction measurements. The reason for increased crystallinity was attributed to the alignment of PFA chains within the amorphous region creating additional crystallite formation. Unfortunately, neither author included any DSC data for the sub-ambient solid-solid transition so there is no historical DSC comparison for the lowered solid-solid phase transition of the wear debris during the first heat (Figure 48a, Figure 49a, Figure 50a). However, *Runt et al.* performed dynamic mechanical analysis (DMA) on PFA films at various draw ratios at temperatures ranging between -150 to 200°C [83]. The β peak near -5°C was suppressed at high strains which is similar to the observed shifted and broadened sub-ambient solid-solid transition in the DSC endotherms of PFA wear debris shown here. Those PFA films tested by Runt were tested at 140 and 200°C, which is well above the β relaxation of the material. This relaxation of the β peak found by *Runt et al.* supports the DSC results (Figure 48a, Figure 49a, Figure 50a) of when mechanical stress is applied to PFA can affect the solid-solid phase transition of PFA near 0°C.

The crystallization behavior of the bulk and wear debris should be the same if the observed differences in the first melt were only due to differences in thermal history (i.e. frictional heating). However, there are distinct differences in the crystallization curves of the bulk and wear debris for all three tested grades (Figure 48c-d, Figure 49c-d, and Figure 50c-d). In the 1.5 mol. % PPVE sample the wear debris crystallizes at higher temperature in both the sub-ambient and high temperature regions (Bulk: 0.7°C, 286.5°C, Wear Debris: 2.1°C, 290.0°C). Similar crystallization temperatures were observed for the 1.9 mol.% PPVE (Wear Debris: 0.4°C, 289.4°C, Bulk: 0.4°C, 289.4°C) and 3.4 mol.% PEVE (Wear Debris: -7.0°C, 277.2°C; Bulk: -7.5°C, 276.9°C) samples. Each of the PPVE samples showed broadened exotherms at the sub-ambient, solid-solid transition (FWHM, 1.5 mol.% : WD=12.5°C, Bulk 9.5°C| 1.9 mol.% WD=12.5°C, Bulk=7.4°C) while the PEVE sample showed a sharper peak (FWHM, WD=15.3°C, Bulk=16.5°C). All three wear debris samples showed increased enthalpy and FWHM compared to bulk samples (Table 11) which shows there is a higher crystallinity and wider distribution of crystallite sizes in the wear debris compared to the bulk.

The second melt (Figure 48e, Figure 49e, and Figure 50e) shows the sub-ambient solid-solid transition in the wear debris sample has shifted to a much higher temperature (1.5 mol% PPVE, 1st melt= -25.5°C, 2nd melt= 7.6°C) and the melting peak is tighter (1.5 mol.% PPVE, FWHM 1st melt= 31.9°C, 2nd Melt= 12.2°C). The wear debris solid-solid transition peak is now shifted to higher temperature than the bulk material (1.5 mol.% PPVE, WD= 7.0°C, Bulk= 5.3°C). The differences between the solid-solid transitions in the first and second melt in the bulk sample (1st melt= 2.5°C, 2nd melt= 5.3°C for 1.5 mol.% PPVE) is most likely due to thermal differences between the injection molding process and the DSC cooling cycle. The wear debris showed higher crystallinity for all three grades than the bulk sample (Table 11). The secondary melting peaks have returned, similar to the bulk samples, for the wear debris (Figure 48c, Figure 49c, and Figure 50c). The changes in polymer structure, as evidenced by differences in crystallization and second melt of the

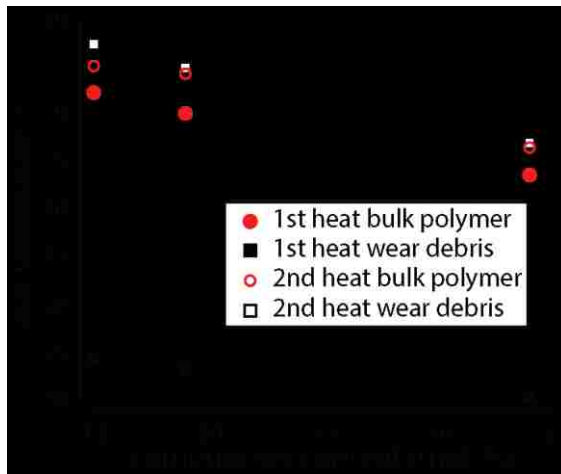


Figure 52: Sub-ambient solid-solid transition temperature for wear debris and bulk PFA of various comonomer concentrations. It should be noted that the high mol. % comonomer sample is PEVE and the two smaller comonomer concentrations are PPVE.

DSC curves of bulk and wear debris, are permanent and are likely due to chemical changes in PFA caused by sliding.

Results of the DSC of the sub-ambient transition show that, increased comonomer content decreases the sub-ambient transition (Figure 52). (1.5 mol.% PPVE 2.5°C, 1.9 mol.% PPVE 0.3°C, 3.4 mol.% PEVE -6.2°C). This agrees with a standard melting point depression, which was previously observed by Puccariello for PFA with PMVE comonomer [74]. An increase of 33°C for the solid-solid transition for the 1.5 mol.% PPVE sample was observed between the first and second heats in the wear debris sample. This is an enormous change, especially in contrast to the bulk sample which only increases 2.8°C under the same thermal cycle. For the 2nd heat, all the wear debris samples had higher sub-ambient solid-solid transitions than their bulk counterparts (Figure 52). This higher sub-ambient solid-solid transition temperature during the second melt signals a larger amount of energy is required for the polymer to transition from the triclinic to the hexagonal crystal structure. Higher crystallinity in fluoropolymers is typically an indicator of reduced molecular weight, which may be caused by shear-driven chain scission. Shear stress likely effects the microstructure of the PFA crystallites and may cause the reduction and broadening of the sub-ambient solid-solid transition during the first melt. Only after melting and recrystallization, can the improved mobility within the microstructure of PFA allow for transition from the hexagonal to triclinic structure at higher temperature (Figure 48f, Figure 49f, Figure 50f). Previous reports on sliding of PTFE and PTFE composites showed reduced molecular weight in wear debris during sliding [87] (Bulk unfilled PTFE: $>1 \times 10^8$ g/mol, unfilled PTFE wear debris: 2.8×10^5 g/mol).

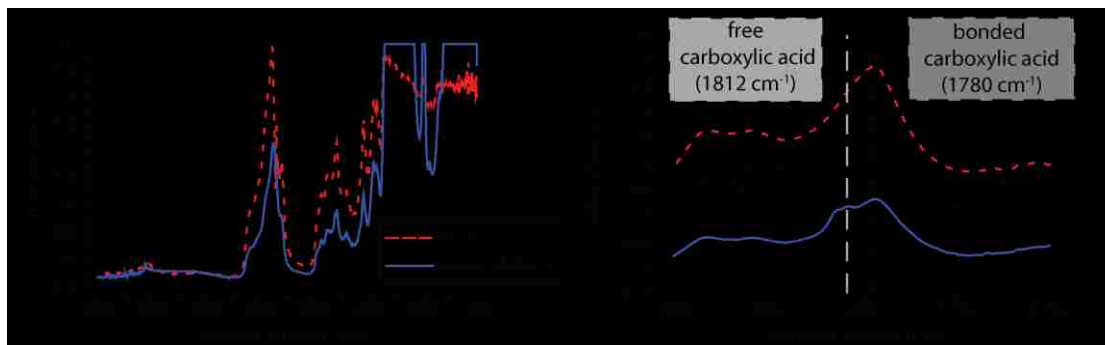


Figure 53: a) Transmission infrared spectra of PFA (1.5 mol. % PPVE) bulk and wear debris. b) Inset of carboxylic acid region of ATR spectra highlighting the free carboxylic acids only present in the bulk sample, which are formed after chain scission of the PFA backbone occurs during sliding.

By evaluating the type of endgroups present in the wear debris and bulk polymer, one may determine if any chain scission has occurred. Transmission infrared spectra may be used to identify endgroups in fluoropolymers [92], [93]. Infrared spectra for bulk and wear debris of 1.5 mol.% PPVE PFA is shown in Figure 53a. The primary difference between the two spectra can be found between 1700-1900 wavenumber (Figure 53b). Bulk PFA only exhibits a peak at 1780 cm^{-1} , which corresponds to bonded carboxylic acids (1780 cm^{-1}). Bonded carboxylic acids are common endgroups that form in PFA during crystallization from melt. When crystallizing, these polar endgroups are likely to bond to another polar group, which reduces the wavelength of the carboxylic acid mode from the unbonded state (1812 cm^{-1}). In contrast, the wear debris spectrum exhibits both free (1812 cm^{-1}) and bonded carboxylic acids (1780 cm^{-1}). Chain scission during sliding is the most likely cause of the formation of the free carboxylic acids in the wear debris [48]. These carboxylic acids remain in the unbonded state due to the lack of mobility available at low temperature for these endgroups to find a polar partner. Evidence of chain scission (reduced molecular

weight) explains the increased enthalpy observed during the second melt in the sub-ambient solid-solid transition and primary melts.

To further understand where in the microstructure (crystalline/amorphous region) this chain scission occurred, attenuated total reflectance infrared spectra (ATR-IR) were taken of the bulk, wear debris, and running film (PFA still attached to bulk that was slid against stainless steel counterface). This was done for three PFA 1.5 mol.% samples (Figure 54).

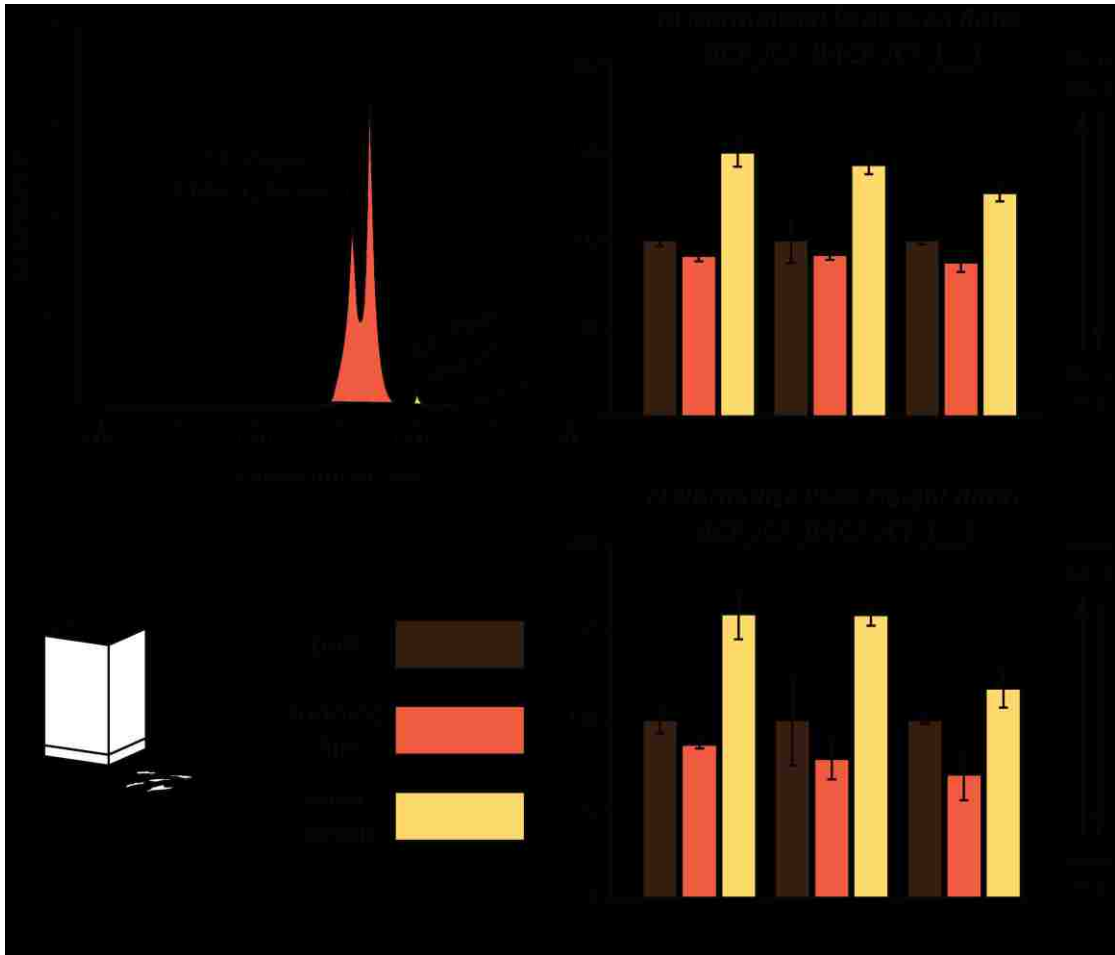


Figure 54: ATR-IR results for three samples of PFA (1.5 mol.% PPVE). The Ratio of relative absorbance of CF₂ and CF₃ curves using area integration (b) and maximum peak values(c) for the bulk, wear debris, and running film show an increase in comonomer is present in the wear debris.

From the CF_3/CF_2 area ratios, the wear debris exhibits higher comonomer (CF_3) than both the running film and bulk of the polymer (Figure 54b). From the ratios of maximum intensity within the spectra, the running film has more CF_2 (TFE) than the bulk (Figure 54c). From both metrics, the wear debris has a higher concentration of CF_3 (therefore PAVE) than the bulk material.

From the ATR-IR results and the results of the first heat, one could conclude that the increased comonomer concentration is the reason for the loss of enthalpy and shifted solid-solid transition peak, as shown by Pucciariello [74]. This is not the case however as the crystallinity of the main melt in the Pucciariello study went down significantly as well compared to the wear debris samples which all exhibit increased enthalpy in the first melt (Table 11). The reduction of the sub-ambient melt with a simultaneous increase in the enthalpy of the main melting peak is due to improved crystallite alignment which promotes higher crystallinity and promotes the hexagonal state at lower temperatures (Figure 48a-b, Figure 49a-b, Figure 50a-b). The same stress causes strain crystallization of the primary melt exhibited by increased crystallinity (Table 11), slight higher melt temperature (Table 11), and greater crystallite size (Figure 51).

Lee et al. investigated the effect of structure within the amorphous region on fatigue life of the polymer [75]. PFA blend with different comonomer amounts and types [PPVE & PEVE] were blended to see if they would co-crystallize together and how this would affect fatigue life via the MIT Flex Life experiment [94]. Flex life tests continuously bend a thin film (typically a polymer) repeatedly back and forth until the specimen fails [94]. These experiments showed that the blended PFAs (PPVE & PEVE) had significantly

improved flex life over the only PPVE PFAs. The authors concluded that the improved structure within the amorphous region (where PAVE (CF₃ rich) groups is highly concentrated) was the cause of the increased lifetime. The repeated stress on the polymer structure during the MIT flex life tests are similar to those completed in tribological tests near the interface. The role the amorphous region plays in fatigue life behavior supports our hypothesis that stress propagates preferentially through the amorphous region of the polymer during microstructural realignment. This stress would likely promote the sub-ambient solid-solid transition from the triclinic to hexagonal state earlier occurring during the first melt in the PFA wear debris, which explains the suppressed sub-ambient solid-solid transition in Figure 48a, Figure 49a, and Figure 50a. Crack propagation through the amorphous region may cause preferential chain scission near comonomer groups which may explain the high concentration of CF₃ attributed in the ATR-IR results (Figure 54b & Figure 54c).

7.6 Conclusion

PFA is composed of crystalline (TFE rich) and amorphous regions (higher concentration of PAVE). During sliding there are multiple structural and chemical changes to PFA including (Figure 55):

1. PFA wear debris exhibit increased crystallite size and overall crystallinity. This is supported by:
 - a. Increase in enthalpy of DSC melting endotherms (Figure 48b, Figure 49b, and Figure 50b)

- b. Increase in the main melt temperature during the first heat (Figure 48b, Figure 49b, and Figure 50b)
 - c. Increased crystallite size of wear debris by XRD methods (Figure 51)
- 2. Alignment of crystallites within wear debris promotes formation of hexagonal crystallite structure at lower temperatures.
 - a. Broadened and shifted solid-solid transition at sub-ambient temperatures during the first heat (Figure 48a, Figure 49a, and Figure 50a)
- 3. Wear debris has reduced molecular weight compared to bulk material.
 - a. Increased concentration of free carboxylic endgroups (Figure 53).
 - b. Higher sub-ambient solid-solid transition temperature and improved crystallinity of wear debris compared to bulk samples in second heat (Figure 48e, Figure 49e, and Figure 50e, Table 11)
- 4. Cracks propagate preferentially through amorphous region during wear
 - a. Increased CF_3/CF_2 ratio of wear debris versus bulk samples (ATR-IR, Figure 54)

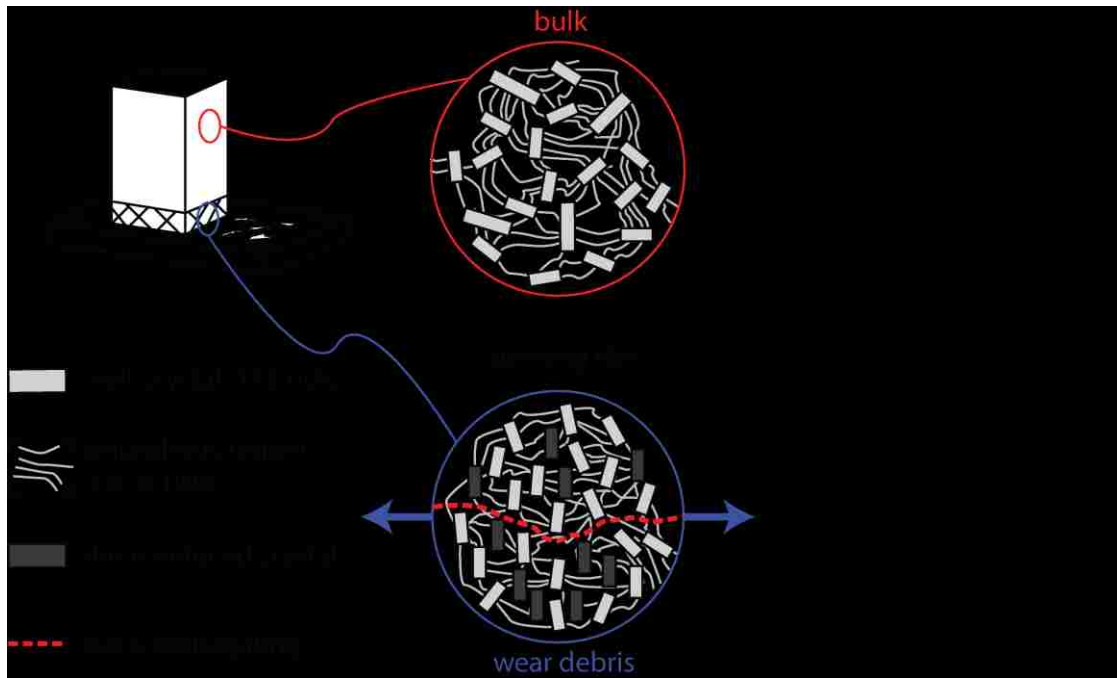


Figure 55: Effects of sliding on PFA microstructure and chemistry

Chapter 8: Environmental effects on tribological performance of PFA and PFA alumina composites

8.1 Overview

Past studies have shown that the removal of atmospheric oxygen and water can lead to ~ 100x higher wear in PTFE-alumina composite materials but no such study has been performed on perfluoroalkyl vinyl ether-alumina (PAVE) composites. The effects of atmospheric water and oxygen on friction and wear of PFA-alumina composites was evaluated using linear reciprocating tribology experiments. Wear rate was determined to be strongly depended on water content in PFA alumina composites with the final wear rate of PFA-alumina tested in dry nitrogen (<2.5 ppm O₂ & H₂O) was found to be 100x worse than PFA-alumina tested in 30% relative humidity air. Attenuated Total Reflectance Infrared Spectroscopy of the polymer-alumina films determined that PFA tested in dry nitrogen had very weak spectra peaks corresponding to carboxylic metallic salts, which were prominent in the samples tested in 15%, 30% and 45% relative humidity air. The formation of these carboxylic salts requires significant oxygen and water content in the environment and is directly related to the wear of the PFA- α alumina composites. These results are similar to the tribological performance of PTFE- α alumina systems tested in dry and vacuum environments.

8.2 Motivation

The effect of environmental constituents on friction and wear of PTFE- α alumina composites has been well established (100x higher wear in dry (<2.5 parts per million (ppm) O₂ and H₂O) or vacuum environments compared to humid air) [44], [45], [49], but no work on environmental tribological testing of PFA or PFA α -alumina has been performed. Preliminary testing on PFA- α alumina in lab air showed a significant relationship between relative humidity, wear rate and friction coefficient, but this data included all three grades of PFA (Chemours® 340, 345, and 440) and three different weight percentages of alumina filler (5%, 7.5%, and 10%) . More details on the effect of humidity are detailed in § 8.2.1). To help eliminate any effects from alumina particle filler concentration or PFA grade (e.g. 340, 345, 440 HP), a more controlled study of PFA- α and PFA- α in environment was performed.

8.2.1 Preliminary Experiments: Effect of relative humidity on wear, friction and tribofilm formation

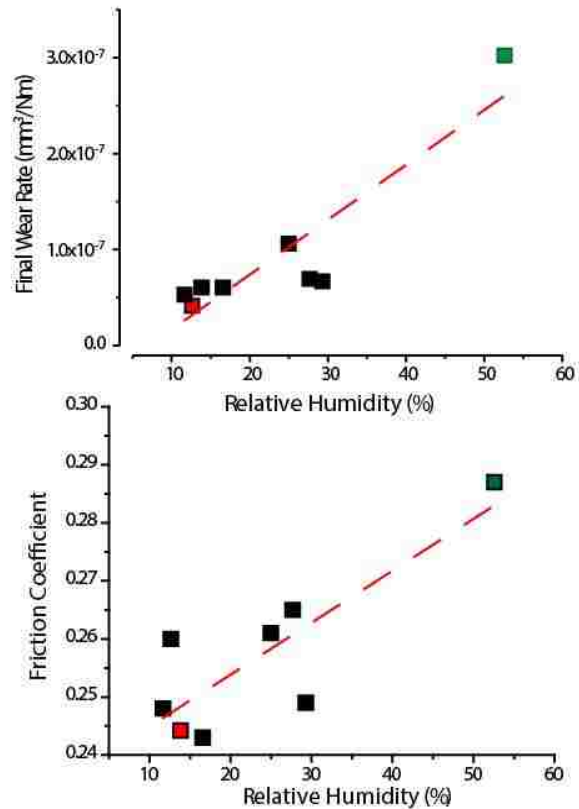
The relative humidity in the tribology lab at Lehigh University changes from nearly 10% from December to March to over 50% during June through August. During each test performed, temperature and relative humidity of the air was monitored, as the tribological performance of PTFE α -Al₂O₃ composites is known to be very sensitive to environmental conditions. Results of the experiments showed that even with different grades of PFA and different weight percentages of filler particles, there was a clear trend of increasing wear rate during the last 200,000 sliding cycles (10km) and friction coefficient with increasing



PFA 345 with 7.5 wt.% Al₂O₃ (250N)
Average RH=13.8%
 $\mu=0.24$
 $K_{final}=6.1 \times 10^{-8} \text{mm}^3/\text{Nm}$



PFA 440 HP with 10 wt.% Al₂O₃ (250N)
Average RH=52.6%
 $\mu=0.29$
 $K_{final}=3.0 \times 10^{-7} \text{mm}^3/\text{Nm}$



relative humidity (Figure 56). Photographs of the transfer films of PFA composite with low friction and wear (top left-hand corner of Figure 56) and relatively high friction and high wear (bottom left-hand corner of Figure 56) show that samples with low friction and wear have a very thin, almost clear tribofilm. The PFA-alumina sample had high friction and wear developed a very dark, thick brown transfer film across nearly the entire wear track.

8.3 Hypothesis

Environmental water and oxygen will not create any drastic effect (>10x difference) on the wear of unfilled PFA as the environmental constituents alone will not prevent subsurface cracking, leading to delamination of unfilled PFA. For the alumina filled PFA, the lowest coefficient of friction for the filled polymers will be in either the dry N₂ environment or the 15% relative humidity environment, based on the preliminary testing. Wear should be the highest in the dry N₂ case, since the lack of oxygen and water vapor will prevent formation of protective tribofilms at the surface of the polymer surface or metallic counterface. The 15 % RH, 30% RH, and 45% RH cases should all produce tribofilms low wear, however the 45% case should develop these films faster than the lower humidity cases causing initially lower wear but leading to higher wear rates once thicker tribofilms form across the steel counterface.

8.4 Materials and Procedure

Samples of unfilled PFA 340 and PFA 340 with 5 wt. % of Al₂O₃ were machined and prepared for testing in controlled environments using the techniques outlined in §4.1.2. The tests will be standard linear reciprocating wear tests (flat on flat geometry) at 6.25 MPa

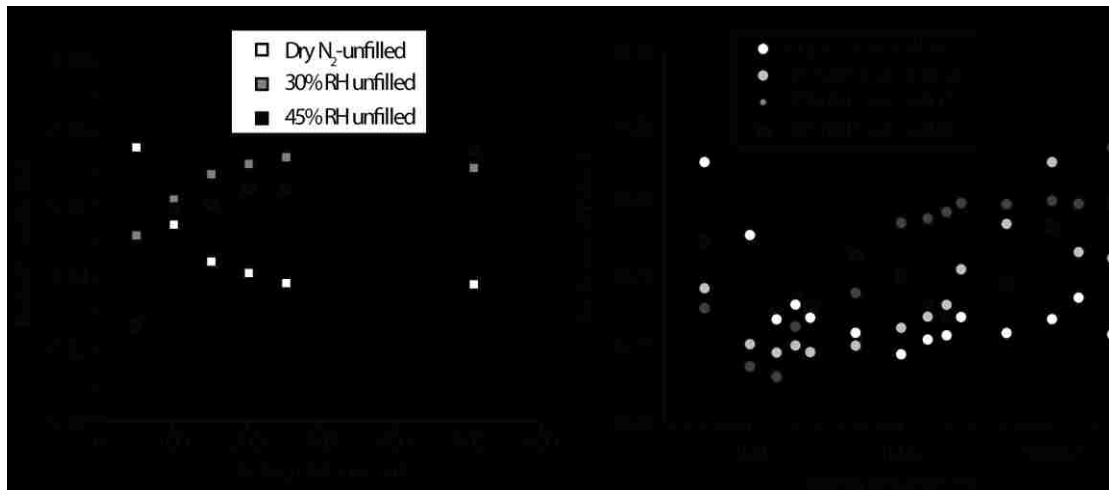


Figure 57: Friction coefficient vs. sliding distance. (left) unfilled PFA in dry nitrogen, 30% RH Air, and 45% RH Air. (Right) PFA-Al₂O₃ (5 wt.%) in dry nitrogen, 30% RH, and 45 RH environments.

contact pressure (250 N normal load). Sliding velocity, sliding stroke, and number of cycles tested will be kept at 50.8 mm/s, 25.4 mm, and 500,000 (10,000 cycles for unfilled samples) to match previous testing conditions on PFA and PFA α -alumina composites [73]. Both unfilled and filled samples will be tested in dry N₂ (<2.5 ppm O₂ and H₂O), 15% RH air ([only PFA -5 wt. % Al₂O₃ test was completed at this humidity level] @20 °C= 3,060 ppm H₂O and 209,500 O₂), 30% RH air (@ 20 °C= 6,970 ppm H₂O and 209,500 O₂), and 45% RH (@20 °C= 10,590 ppm H₂O and 209,500 O₂) air for a total of eight tests. The wear rate, friction coefficient and the tribofilms to be monitored over duration of the experiments. In addition to the tribological testing, ATR-FTIR will be performed on all running films to observe any chemical differences between the samples.

8.5 Results & Discussion

8.5.1 Friction performance as a function of relative humidity

Friction of unfilled PFA composites as a function of relative humidity (RH) is shown in Figure 57a. Initially the friction coefficient was lowest for the 45 % RH, followed by the 30% RH sample, while the dry N₂ sample exhibited the highest friction. Throughout the remaining tests, the dry N₂ unfilled sample dropped from almost 0.28 initially down to near 0.24 for the last ~250 m of sliding. Both the 30% and 45% RH tests exhibited increases in friction coefficient with increased sliding distance, with final friction coefficient values of ~0.27.

Friction behavior for PFA-alumina composites in dry nitrogen, 15% RH, 30 % RH, and 45% RH is shown in Figure 57b (please note the semi-log scale for the sliding distance axis). Initially the dry N₂ has the highest friction coefficient, but it quickly drops between

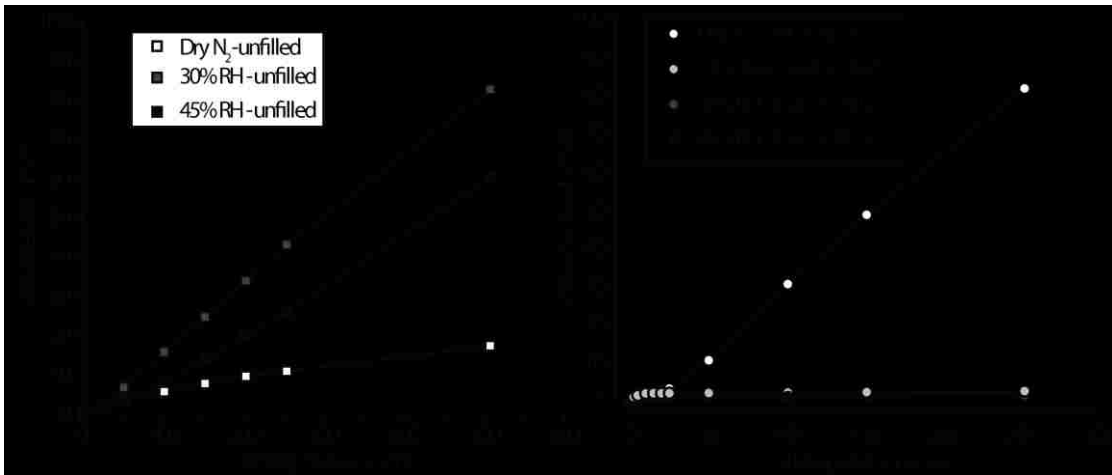


Figure 58: Volume lost vs. sliding distance. (left) unfilled PFA in dry nitrogen, 30% RH Air, and 45% RH Air over 508 m. (Right) PFA-Al₂O₃ (5 wt.%) in dry nitrogen, 30% RH, and 45 RH environments over 25.4 km.

0.22-0.23 after 100m of sliding. PFA-alumina at 15% RH conditions had a friction coefficient of 0.23 or less during the first 1000m of sliding and which rose to a maximum of 0.26 and then reduced slightly to 0.24 over the last 200k cycles. PFA-alumina tested in 30% RH air exhibited initially low friction ($\mu < 0.24$) during the first 500m of sliding (10k cycles) but then had steadily increasing friction coefficient with a final friction coefficient of nearly 0.28. The PFA-alumina sample tested in the most humid environment (45% RH) was initially at 0.25 during the first 2,000 sliding cycles (100 m). The friction then varied between 0.23 and 0.25 until the first 5,000m of sliding were completed. For 100k cycles the friction coefficient jumped up to 0.255, then dropped down to 0.235 for the next 100k cycles (5,080 m), and then increased again back to 0.26 for the final 200k sliding cycles (10,160 m). Samples tested in dry nitrogen were found to have lower friction coefficients in both unfilled PFA and alumina filled PFA compared to the 15%, 30% and 45% humidity cases. The 45% RH sample had significantly lower friction than the 30% RH sample for PFA-alumina composites, which did not match the expected preliminary trend.

8.5.2 Wear rate as a function of relative humidity

Volume lost vs sliding distance graphs for unfilled PFA and PFA alumina composites are shown in Figure 59a and Figure 59b respectively. Slope of the volume lost vs sliding distance curves is representative of wear rate (steeper slopes correspond to higher wear rates and shallower slopes correspond to lower wear rates). Wear rates are provided for all experiments in Table 13. Unfilled PFA had the lowest wear rate in the dry nitrogen environment ($K=1.3 \times 10^{-4} \text{ mm}^3/\text{Nm}$) compared to the 30% ($K=6.4 \times 10^{-4} \text{ mm}^3/\text{Nm}$) and 45% RH tests ($K=4.8 \times 10^{-4} \text{ mm}^3/\text{Nm}$).

Wear for the PFA-alumina composites in different environments was more nuanced. Initially (over the first 1000 cycles), the PFA- α Al₂O₃ sample tested in dry nitrogen had the lowest wear rate (1.1×10^{-6} mm³/Nm) which was more than ten times less than the 15% RH, 30% RH and 45% RH experiments over the first 1000 cycles (Table 13). After 5000 sliding cycles, the wear rate for the dry N₂ tested sample increased to 4.28×10^{-6} mm³/Nm, while both the 15%, 30% and 45% RH experiments showed a significant drop in wear rate. This trend continued after the next 5000 sliding cycle experiment, with wear rate of the dry nitrogen experiment increasing while the wear of the humid environment experiments continued to decrease. After 50,000 cycles, the total wear rate of the 45% RH experiment has reached an order of magnitude less (3.9×10^{-7} mm³/Nm) than the dry N₂ tested sample (4.4×10^{-6} mm³/Nm). These differences are exacerbated after the entire experiment is completed, as the total wear rate of PFA- α Al₂O₃ in dry N₂ increases to 1.26×10^{-5} mm³/Nm while the wear of the filled PFA composites reduces to 1.8×10^{-7} mm³/Nm and 3.0×10^{-7} mm³/Nm over the entire test. The massive increase in wear of the PFA- α Al₂O₃ composite

in the dry nitrogen environment is highlighted by the increase in slope of its volume lost vs sliding distance curve (Figure 59b).

8.5.3 Tribofilms

Photographs of running films and transfer films of the PFA-alumina composites in dry nitrogen, 15% RH, 30% RH, and 45% relative humidity environments are shown in Figure 60. The running film of the sample tested in dry nitrogen initially showed some brown discoloration similar to what was observed in humid environments. As the dry nitrogen experiment continued, the brown patches on running film were no longer present and black, fibrous wear debris began to develop and build up at the edge of the wear track (Figure 60). This corresponds with the increase in the wear rate for the dry nitrogen case after 2500m (Figure 59, Table 13). In contrast, the samples tested in humid experiments were able to maintain brown running films and developed brown colored transfer films, with the

Table 13: Wear rates as a function of relative humidity for unfilled and 5 wt. % PFA-Alumina composites. The number of cycles within the parenthesis represents the number of cycles tested when the total wear rate (total volume lost divided by total sliding distance and average applied force) was calculated. K_{final} is the wear rate during the last 200k sliding cycles.

	RH %	K (1k) mm ³ /Nm	K(5k) mm ³ /Nm	K(10k) mm ³ /Nm	K(50k) mm ³ /Nm	K(500k) mm ³ /Nm	K _{final} mm ³ /Nm
Unfilled PFA	0	0.000319	0.000172	0.000136	N/A	N/A	N/A
	30	0.000526	0.000658	0.00064	N/A	N/A	N/A
	45	0.000268	0.000408	0.000475	N/A	N/A	N/A
PFA-5 wt. % Al ₂ O ₃	0	1.09E-06	4.28E-06	4.56E-06	4.37E-06	1.26E-05	1.27E-05
	15	1.50E-05	9.42E-06	7.84E-06	2.42E-06	3.22E-07	9.93E-08
	30	1.74E-05	4.52E-06	2.37E-06	1.55E-06	1.82E-07	6.95E-08
	45	1.28E-05	2.85E-06	1.44E-06	3.92E-07	3.03E-07	3.09E-07

45% RH sample producing a significantly thicker and even transfer film than the 15% and 30% cases (Figure 60).

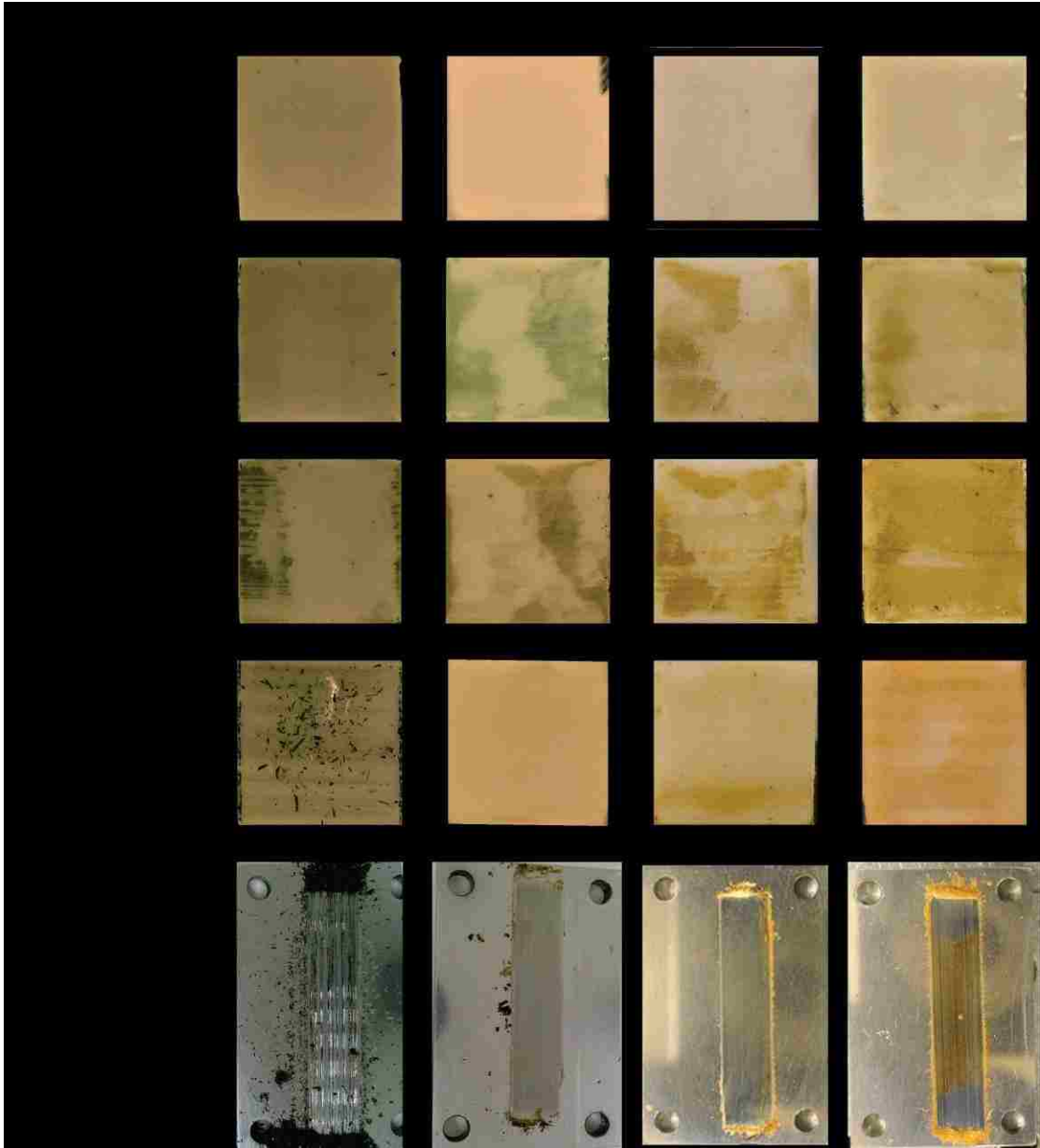


Figure 60: Tribofilms as a function of sliding distance and relative humidity.

8.5.4 ATR-IR Results

Attenuated Total Reflectance Infrared spectra of the bulk specimens and running films of the various PFA- α Al_2O_3 composites tested are shown in Figure 61 and Figure 62

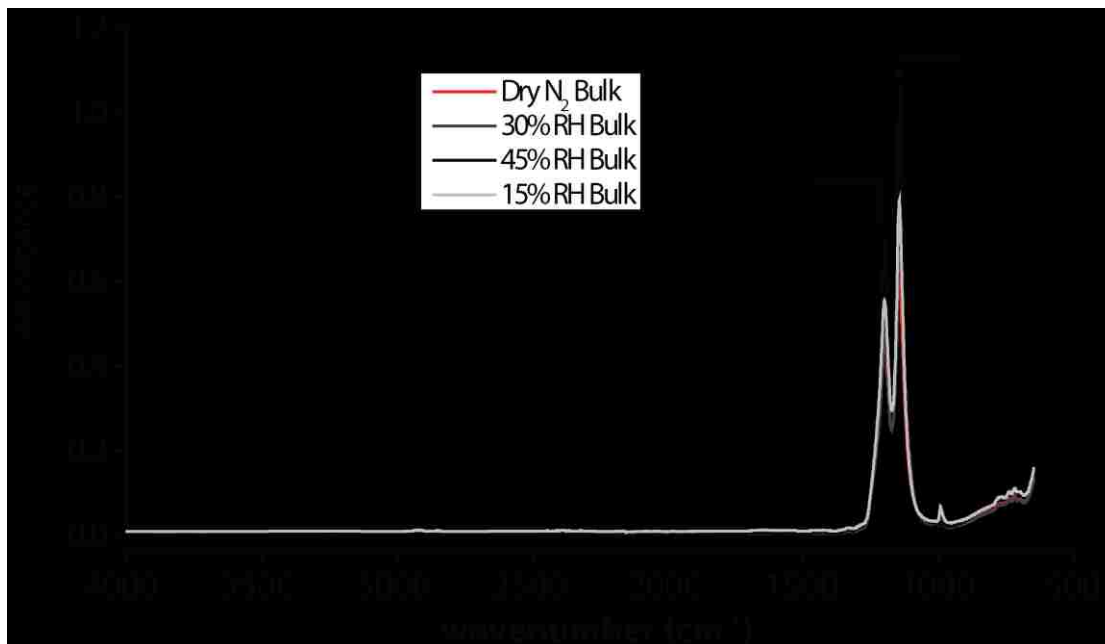


Figure 61: Attenuated Total Reflectance Infrared Spectra of PFA-Alumina bulk (untested) surfaces

respectively. The infrared spectra of the bulk PFA-alumina composites are nearly identical and include two peaks that represent CF_2 bonds at 1159 cm^{-1} and 1216 cm^{-1} , one peak at 993 cm^{-1} that represents CF_3 bonds in the perfluorinated alkyl vinyl ether, and a broad peak under 900 cm^{-1} that represents aluminum oxide (Figure 61). The PFA-alumina wear surfaces tested in humid environments showed similar peaks as the bulk samples with the addition of two peaks at 1434 and 1665 cm^{-1} that represent carboxylic salt groups and a broad peak that extends from 2800 cm^{-1} to 3700 cm^{-1} (Figure 61). The PFA-alumina composite tested in the dry nitrogen environment only exhibits very small absorbance peaks for carboxylic salts and waters of hydration. All worn samples exhibited higher intensities within the metal oxide region (broad peak under 900 cm^{-1}) compared to the bulk, which corresponds to an increase in concentration of alumina particles at the composite

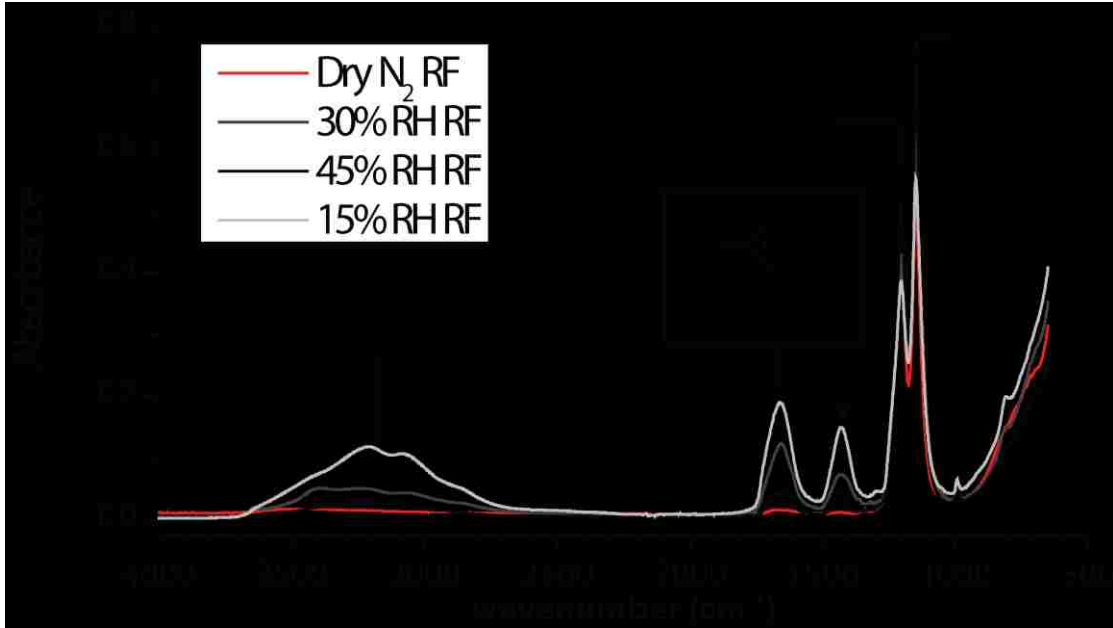


Figure 62: Attenuated Total Reflectance Infrared Spectra of PFA-Alumina running films (tested surface).

surface. Increased concentration of alumina particles at the worn surface was also observed through x-ray microtomography and transmission electron microscopy by *Krick et al.* in 2016 (Figure 38) [62]. The relative intensity of the carboxylic salt peaks in the ATR-spectra did not directly correspond with with the wear rates of the composite samples over the last 200,000 sliding cycles (Figure 62).

8.6 Conclusions

After controlled tribological experiments in four environments (Dry nitrogen (< 2.5ppm O₂ and H₂O), 15% RH, 30% RH, and 45% RH) of unfilled PFA and PFA-alumina (5 wt. %) composites, along with attenuated total reflectance infrared spectroscopy of the running films, the following conclusions could be drawn:

1. Friction of unfilled PFA and PFA-alumina composites were lowest in dry nitrogen environments (Figure 57).
2. Wear rate of the unfilled PFA samples was lowest in the dry nitrogen environment (Figure 59).
3. The wear rate of the PFA-alumina composite samples tested in dry nitrogen was nearly 100x greater than the sample tested in 30% RH (Table 13).
4. Brown tribofilms initially developed on the PFA alumina composite surfaces in all four environments. In the dry nitrogen case, there may still have been some adsorbed water on the surface of the polymer composite that was not removed during transfer to the dry environment. The tribofilms wore away for the PFA-alumina composite tested in dry nitrogen and large, black fibrous wear debris developed on the ends of the wear track on the countersample. The sample tested in 15% and 30% RH environments developed a very thin transfer film while the sample tested in 45% RH developed a thick transfer film across the metallic counterface (Figure 60).
5. Infrared spectra of the running film surfaces revealed the presence of carboxylic salts in the three samples tested in humid environments. Very weak carboxylic salt peaks were observed in the dry nitrogen tested sample compared to the samples tested in humid environments (Figure 62).

Chapter 9: Conclusions

The conclusions of this dissertation are summarized in Figure 64 and are listed below:

1. **Role of Alumina Particle Hardness**- Through coupled tribology and in-situ nanoindentation experiments, the importance of compliant, friable metal-oxide particles with similar hardness to the stainless steel counterface in promoting protective tribofilms that enable ultralow wear fluoropolymer metal-oxide composites was confirmed.
2. **Ultralow wear PFA-Alumina is a melt processible alternative to PTFE**- Screw injection molded PFA-nanostructured alumina composite samples exhibited ultralow wear rates ($K < 5 \times 10^{-7} \text{ mm}^3/\text{Nm}$) similar to those found in PTFE-nanostructured alumina composite materials. Infrared spectroscopy

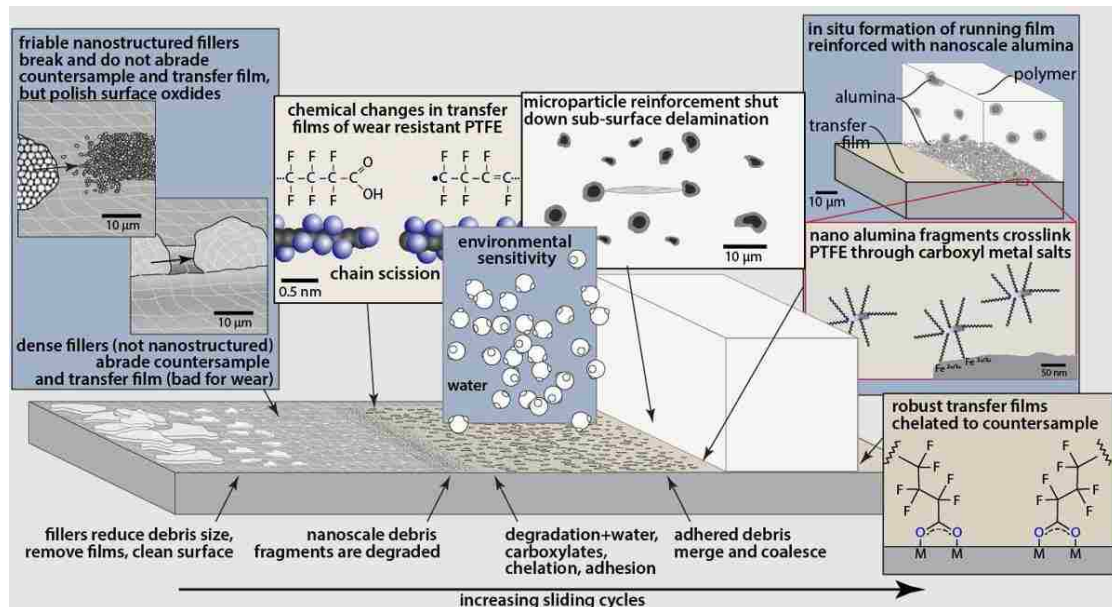


Figure 64: Summary of the tribochemical mechanism that promotes ultralow wear in fluoropolymer alumina composite materials.

confirmed the formation of carboxylic salts on the PFA composite and the stainless steel counterface. These carboxylic salts have been previously found in ultralow wear PTFE- α Al_2O_3 composites and confirm the tribochemical mechanism persists for ultralow wear PFA- α Al_2O_3 composites.

3. **Sliding causes changes microstructure and chemistry in unfilled PFA-**

Wear debris of PFA samples was found to have increased crystallinity and increased crystallite alignment after sliding. Additionally, chain scission of unfilled PFA was confirmed by the formation of free carboxylic acid endgroups found by transmission infrared measurements. These chain scission events were proposed to be more likely occur within the amorphous region of the polymer due to increased comonomer concentration found in the wear debris by attenuated total reflectance infrared measurements.

4. **Wear of PFA alumina composites is dependent on H_2O and O_2 -** Tests of

PFA-alumina composites in dry N_2 (<2.5 ppm O_2 and H_2O), 15% RH, 30% RH air, and 45% RH air revealed a 100x higher wear rates in the dry nitrogen environment compared to humid environments. Attenuated total reflectance infrared measurements of the worn PFA-alumina composite surfaces revealed only a minor amount of carboxylic salts present on the sample tested in dry nitrogen. This agrees with the proposed tribochemical mechanism that requires broken PFA chains to bond with atmospheric H_2O and O_2 to form tribofilms on the PFA composite and stainless steel counterface surfaces.

References

- [1] P. H. Jost, "Lubrication: Tribology; Education and Research; Report on the Present Position and Industry's Needs," 1966.
- [2] Y. Yamaguchi, "Application to Sliding Machine parts," in *Tribology of Plastic Materials*, 1990, pp. 203–347.
- [3] F. J. Clauss, *Solid Lubricants and Self-Lubricating Solids*. New York: Academic Press, 1972.
- [4] R. Carpick, A. Jackson, P. Lee, N. Argibay, A. Pachon Garcia, W. G. Sawyer, and K. Bennet, "Tribology Opportunities for Enhancing America's Energy Efficiency," 2017.
- [5] J. Wisniak, "Guillaume Amontons," *Rev. CENIC. Ciencias Quim.*, vol. 36, no. 3, pp. 187–195, 2005.
- [6] G. Amontons, "De la resistance causee dans les machines," *Mem. Acad Roy. Sci.*, pp. 206–227, 1699.
- [7] E. McCurdy, *The Notebooks of Leonardo da Vinci, Vol. 1*. New York: Reynal and Hitchcock, 1938.
- [8] J. F. Archard and W. Hirst, "The Wear of Metals under Unlubricated Conditions," *Proc. R. Soc. A Math. Phys. Eng. Sci.*, vol. 236, no. 1206, pp. 397–410, 1956.
- [9] -Roy J. Plunkett, "TETRAFLUOROETHYLENE POLYMERS," 2,230,654, 1941.
- [10] S. Ebnesajjad, *FLUOROPLASTICS Volume 1: Non-Melt Processible Fluoropolymers - The Definitive User's Guide and Data Book*, 2nd ed. New York: Elsevier, 2015.
- [11] S. Ebnesajjad, *FLUOROPLASTICS Volume 2: Melt Processible Fluoropolymers - The Definitive User's Guide and Data Book*. New York: Elsevier, 2015.
- [12] L. . Sperling, *Physical Polymer Science*. 2006.
- [13] A. Fujimori, M. Hasegawa, and T. Masuku, "Spherulitic structures of poly [tetrafluoroethylene-co-(perfluoroalkyl vinyl ether)]," *Polym. Int.*, vol. 56, pp. 1281–1287, 2007.
- [14] B. S. Unlu, E. Atik, and S. Koksal, "Tribological properties of polymer-based journal bearings," *Mater. Des.*, vol. 30, no. 7, pp. 2618–2622, 2009.
- [15] T. Tevrüz, "Tribological behaviours of bronze-filled polytetrafluoroethylene dry journal bearings," *Wear*, vol. 221, no. 1, pp. 61–68, 1998.
- [16] S. K. Biswas and K. Vijayan, "Changes to near-surface region of PTFE during dry sliding against

- steel,” *J. Mater. Sci.*, vol. 23, no. 5, pp. 1877–1885, 1988.
- [17] K. G. McLaren and D. Tabor, “Visco-elastic properties and the friction of solids: Friction of polymers: Influence of speed and temperature,” *Nature*, vol. 197, no. 4870, pp. 856–858, 1963.
- [18] K. Tanaka and S. Kawakami, “Effect of various fillers on the friction and wear of polytetrafluoroethylene-based composites,” *Wear*, vol. 79, no. 2, pp. 221–234, 1982.
- [19] Y. Uchiyama and K. Tanaka, “Wear laws for polytetrafluoroethylene,” *Wear*, vol. 58, no. 2, pp. 223–235, 1980.
- [20] K. Tanaka, Y. Uchiyama, and S. Tooyooka, “The mechanism of wear of polytetrafluoroethylene,” *Wear*, vol. 23, pp. 153–172, 1973.
- [21] T. A. Blanchet, “Friction, Wear, and PV Limits of Polymers and Their Composites,” in *Tribology Data Handbook*, E. R. Booser, Ed. New York: CRC Press, 1997, pp. 547–562.
- [22] C. Pooley and D. Tabor, “Friction and molecular structure: the behaviour of some thermoplastics,” *Proc. R. Soc. London Ser. A*, pp. 251–274, 1972.
- [23] T. A. Blanchet and F. E. Kennedy, “Sliding wear mechanism of polytetrafluoroethylene (PTFE) and PTFE composites,” *Wear*, vol. 153, no. 1, pp. 229–243, 1992.
- [24] G. De-Li, Z. Bing, X. Qun-Ji, and W. Hong-Li, “Effect of tribochemical reaction of polytetrafluoroethylene transferred film with substrates on its wear behaviour,” *Wear*, vol. 137, no. 2, pp. 267–273, 1990.
- [25] D. L. Burris, S. Zhao, R. Duncan, J. Lowitz, S. S. Perry, L. S. Schadler, and W. G. Sawyer, “A route to wear resistant PTFE via trace loadings of functionalized nanofillers,” *Wear*, vol. 267, no. 1–4, pp. 653–660, 2009.
- [26] B. J. Briscoe, A. K. Pogosian, and D. Tabor, “The friction and wear of high density polythene: The action of lead oxide and copper oxide fillers,” *Wear*, vol. 27, no. 1, pp. 19–34, 1974.
- [27] M. Clerico and V. Patierno, “Sliding wear of polymeric composites,” *Wear*, vol. 53, no. 2, pp. 279–301, 1979.
- [28] S. Nak-Ho and N. P. Suh, “Effect of fiber orientation on friction and wear of fiber reinforced

- polymeric composites,” *Wear*, vol. 53, no. 1, pp. 129–141, 1979.
- [29] S. Bahadur and D. Tabor, “The wear of filled polytetrafluoroethylene,” *Wear*, vol. 98, pp. 1–13, 1984.
- [30] B. J. Briscoe, Lin Heng Yao, and T. a. Stolarski, “The friction and wear of poly(tetrafluoroethylene)-poly (etheretherketone) composites: An initial appraisal of the optimum composition,” *Wear*, vol. 108, no. 4, pp. 357–374, 1986.
- [31] F. Li, K. A. Hu, J. L. Li, and B. Y. Zhao, “The friction and wear characteristics of nanometer ZnO filled polytetrafluoroethylene,” *Wear*, vol. 249, no. 10–11, pp. 877–882, 2001.
- [32] W. X. Chen, F. Li, G. Han, J. B. Xia, L. Y. Wang, J. P. Tu, and Z. D. Xu, “Tribological behavior of carbon-nanotube-filled PTFE composites,” *Tribol. Lett.*, vol. 15, no. 3, pp. 275–278, 2003.
- [33] W. G. Sawyer, K. D. Freudenberg, P. Bhimaraj, and L. S. Schadler, “A study on the friction and wear behavior of PTFE filled with alumina nanoparticles,” *Wear*, vol. 254, no. 5–6, pp. 573–580, 2003.
- [34] J. K. Lancaster, “Polymer-based Bearing Materials: The Rule of Fillers and Fiber Reinforcement,” *Tribol. Int.*, vol. 5, no. December, pp. 249–255, 1972.
- [35] T. A. Blanchet and F. E. Kennedy, “A model for polymer composite wear behavior including preferential load support and surface accumulation of filler particulates,” *Tribol. Trans.*, vol. 38, no. 4, pp. 821–828, 1995.
- [36] J. K. Lancaster, “The effect of carbon fibre reinforcement on the friction and wear of polymers,” *J. Phys. D. Appl. Phys.*, vol. 1, no. 5, pp. 549–560, 1968.
- [37] J. K. K. Lancaster, “Polymer-based bearing materials: The role of fillers and fibre reinforcement J.,” *Tribology*, vol. 5, no. 6, pp. 249–255, 1972.
- [38] B. Arkles, J. Theberge, and M. Schireson, “Wear Behavior of Thermoplastic Polymer- Filled PTFE composites,” *Lubr. Eng.*, vol. 33, no. 1, pp. 33–38, 1977.
- [39] D. L. Burris and W. G. Sawyer, “Improved wear resistance in alumina-PTFE nanocomposites with irregular shaped nanoparticles,” *Wear*, vol. 260, no. 7–8, pp. 915–918, 2006.
- [40] S. E. McElwain, T. A. Blanchet, L. S. Schadler, and W. G. Sawyer, “Effect of Particle Size on the

- Wear Resistance of Alumina-Filled PTFE Micro- and Nanocomposites,” *Tribol. Trans.*, vol. 51, no. 3, pp. 247–253, 2008.
- [41] T. A. Blanchet, S. S. Kandanur, and L. S. Schadler, “Coupled effect of filler content and countersurface roughness on PTFE nanocomposite wear resistance,” *Tribol. Lett.*, vol. 40, no. 1, pp. 11–21, 2010.
- [42] B. A. Krick, J. J. Ewin, and E. J. McCumiskey, “Tribofilm Formation and Run-In Behavior in Ultra-Low Wearing Polytetrafluoroethylene (PTFE) and Alumina Nanocomposites,” *Tribol. Trans.*, no. August 2014, pp. 00–00, 2014.
- [43] J. Ye, H. S. Khare, and D. L. Burris, “Quantitative characterization of solid lubricant transfer film quality,” *Wear*, vol. 316, no. 1–2, pp. 133–143, 2014.
- [44] B. A. Krick, J. J. Ewin, G. S. Blackman, C. P. Junk, and W. G. Sawyer, “Environmental dependence of ultra-low wear behavior of polytetrafluoroethylene (PTFE) and alumina composites suggests tribochemical mechanisms,” *Tribol. Int.*, vol. 51, no. July 2015, pp. 42–46, 2012.
- [45] H. S. Khare, A. C. Moore, D. R. Haidar, L. Gong, J. Ye, J. F. Rabolt, and D. L. Burris, “Interrelated Effects of Temperature and Environment on Wear and Tribochemistry of an Ultralow Wear PTFE Composite,” *J. Phys. Chem. C*, vol. 119, no. 29, pp. 16518–16527, 2015.
- [46] D. L. Burris, B. Boesl, G. R. Bourne, and W. G. Sawyer, “Polymeric nanocomposites for tribological applications,” *Macromol. Mater. Eng.*, vol. 292, no. 4, pp. 387–402, 2007.
- [47] W. G. Sawyer, N. Argibay, D. L. Burris, and B. A. Krick, “Mechanistic Studies in Friction and Wear of Bulk Materials,” *Annu. Rev. Mater. Res.*, vol. 44, no. 1, pp. 395–427, 2014.
- [48] K. L. Harris, A. A. Pitenis, W. G. Sawyer, B. A. Krick, G. S. Blackman, D. J. Kasprzak, and C. P. Junk, “PTFE Tribology and the Role of Mechanochemistry in the Development of Protective Surface Films,” *Macromolecules*, p. 150526153713007, 2015.
- [49] A. A. Pitenis, J. J. Ewin, K. L. Harris, W. G. Sawyer, and B. A. Krick, “In vacuo tribological behavior of polytetrafluoroethylene (ptfe) and alumina nanocomposites: The importance of water for ultralow wear,” *Tribol. Lett.*, vol. 53, no. 1, pp. 189–197, 2014.

- [50] B. A. Krick, J. J. Ewin, and E. J. McCumiskey, "Tribofilm Formation and Run-In Behavior in Ultra-Low Wearing Polytetrafluoroethylene (PTFE) and Alumina Nanocomposites," *Tribol. Trans.*, p. 0, 2014.
- [51] J. Ye, D. Burris, and T. Xie, "A Review of Transfer Films and Their Role in Ultra-Low-Wear Sliding of Polymers," *Lubricants*, vol. 4, no. 1, p. 4, 2016.
- [52] D. L. Burris and W. G. Sawyer, "Tribological Sensitivity of PTFE/Alumina Nanocomposites to a Range of Traditional Surface Finishes," *Tribol. Trans.*, vol. 48, no. 2, pp. 147–153, 2005.
- [53] J. Ye, "CHARACTERIZING PTFE TRANSFER FILM PROPERTIES TO ELUCIDATE TRANSFER FILM ' S ROLE IN ULTRA -LOW WEAR SLIDING OF POLYMER NANOCOMPOSITES," University of Delaware, 2014.
- [54] J. Ye, A. C. Moore, and D. L. Burris, "Transfer Film Tenacity: A Case Study Using Ultra-Low-Wear Alumina–PTFE," *Tribol. Lett.*, vol. 59, no. 3, p. 50, 2015.
- [55] R. C. Bowers and W. A. Zisman, "Frictional Properties of Tetrafluoroethylene-Perfluoro(propyl vinyl ether) Copolymers," vol. 13, no. 2, pp. 115–118, 1974.
- [56] J. E. Crosby, J M , Theberge and K. L. Talley, "Melt Processible Fluoropolymer Composites," *J. Elastomers Plast.*, vol. 13, no. July, pp. 149–155, 1981.
- [57] D. L. Burris and W. G. Sawyer, "Addressing practical challenges of low friction coefficient measurements," *Tribol. Lett.*, vol. 35, no. 1, pp. 17–23, 2009.
- [58] T. V. Vorburger, H. G. Rhee, T. B. Renegar, J. F. Song, and A. Zheng, "Comparison of optical and stylus methods for measurement of surface texture," *Int. J. Adv. Manuf. Technol.*, vol. 33, no. 1–2, pp. 110–118, 2007.
- [59] R. Leach, X. J. Leigh Brown, R. Blunt, and D. M. Mike Conroy, "Guide for the Measurement of Smooth Surface Topography using Coherence Scanning Interferometry," 2008.
- [60] W. C. Oliver and G. M. Pharr, "Measurement of hardness and elastic modulus by instrumented indentation: Advances in understanding and refinements to methodology," *J. Mater. Res.*, vol. 19, no. 1, pp. 3–20, 2004.

- [61] G. R. Strobl and M. Schneider, "Direct evaluation of the electron density correlation function of partially crystalline polymers," *J. Polym. Sci. Polym. Phys. Ed.*, vol. 18, no. 6, pp. 1343–1359, 1980.
- [62] B. A. Krick, A. A. Pitenis, K. L. Harris, C. P. Junk, W. G. Sawyer, S. C. Brown, H. D. Rosenfeld, D. J. Kasprzak, R. S. Johnson, C. D. Chan, and G. S. Blackman, "Ultralow wear fluoropolymer composites: Nanoscale functionality from microscale fillers," *Tribol. Int.*, vol. 95, pp. 245–255, Nov. 2016.
- [63] S. Brunauer, P. H. Emmett, and E. Teller, "Adsorption of Gases in Multimolecular Layers," *J. Am. Chem. Soc.*, vol. 407, no. 1, pp. 309–319, 1936.
- [64] D. W. Hahn, "Light Scattering Theory," *Dep. Aerosp. Eng. Univ. Florida*, vol. 27, no. July, pp. 1–13, 2009.
- [65] J. Wang, Y.-H. Yu, S. . Lee, and Y.-W. Chung, "Tribological and optical properties of crystalline and amorphous alumina thin films grown by low-temperature reactive magnetron sputter-deposition," *Surf. Coatings Technol.*, vol. 146–147, pp. 189–194, 2001.
- [66] J. Ye, H. S. Khare, and D. L. Burris, "Transfer film evolution and its role in promoting ultra-low wear of a PTFE nanocomposite," *Wear*, vol. 297, no. 1–2, pp. 1095–1102, 2013.
- [67] L. S. Schadler, L. C. Brinson, and W. G. Sawyer, "Polymer nanocomposites: A small part of the story," *JOM*, vol. 59, no. 3, pp. 53–60, 2007.
- [68] W. A. Brainard and D. H. Buckley, "Adhesion and friction of PTFE in contact with metals as studied by Auger spectroscopy, field ion and scanning electron microscopy," *Wear*, vol. 26, no. 1, pp. 75–93, 1973.
- [69] B. A. Krick, D. W. Hahn, and W. G. Sawyer, "Plasmonic Diagnostics for Tribology: In Situ Observations Using Surface Plasmon Resonance in Combination with Surface-Enhanced Raman Spectroscopy," *Tribol. Lett.*, vol. 49, no. 1, pp. 95–102, 2013.
- [70] T. L. Schmitz, J. E. Action, D. L. Burris, J. C. Ziegert, and W. G. Sawyer, "Wear-Rate Uncertainty Analysis," *J. Tribol.*, vol. 126, no. 4, p. 802, 2004.
- [71] J. M. Urueña, A. A. Pitenis, K. L. Harris, and W. G. Sawyer, "Evolution and Wear of Fluoropolymer

- Transfer Films,” *Tribol. Lett.*, vol. 57, no. 2, 2015.
- [72] T. Onodera, K. Kawasaki, T. Nakakawaji, Y. Higuchi, N. Ozawa, K. Kurihara, and M. Kubo, “Chemical reaction mechanism of polytetrafluoroethylene on aluminum surface under friction condition,” *J. Phys. Chem. C*, vol. 118, no. 10, pp. 5390–5396, 2014.
- [73] M. A. Sidebottom, A. A. Pitenis, C. P. Junk, D. J. Kasprzak, G. S. Blackman, H. E. Burch, K. L. Harris, W. G. Sawyer, and B. A. Krick, “Ultralow wear Perfluoroalkoxy (PFA) and alumina composites,” *Wear*, vol. 362–363, pp. 179–185, 2016.
- [74] R. Pucciariello, “Thermal characterization of tetrafluoroethylene-perfluoroalkylvinylether copolymers: Melting behavior and low-temperature transitions,” *J. Polym. Sci. Part B Polym. Phys.*, vol. 32, no. 10, pp. 1771–1776, 1994.
- [75] J. C. Lee, S. Namura, S. Kondo, and A. Abe, “Miscibility and cocrystallization behavior of two melt-processable random copolymers of tetrafluoroethylene and perfluoroalkylvinylether,” *Polymer (Guildf)*, vol. 42, no. 12, pp. 5453–5461, 2001.
- [76] J. J. Weeks, I. C. Sanchez, R. K. Eby, and C. I. Poser, “Order disorder transitions in polytetrafluoroethylene,” *Polymer (Guildf)*, vol. 21, pp. 325–331, 1980.
- [77] J. Runt, L. Jin, S. Talibuddin, and C. R. Davis, “Crystalline Homopolymer-Copolymer Blends: Poly(tetrafluoroethylene)-Poly(tetrafluoroethylene-co-perfluoroalkylvinyl ether),” *Macromolecules*, vol. 28, no. 8, pp. 2781–2786, 1995.
- [78] J. J. Weeks, R. K. Eby, and E. S. Clark, “Disorder in the crystal structures of phases 1 and 2 of copolymers of tetrafluoroethylene and hexafluoroprophylyene.pdf,” pp. 0–3, 1981.
- [79] G. Guerra, V. Venditto, C. Natale, P. Rizzo, and C. De Rosa, “Structural variations in random copolymers of tetrafluoroethylene with kind and content of comonomer units,” *Polymer (Guildf)*, vol. 39, no. 14, pp. 3205–3209, 1998.
- [80] T. R. Dargaville, G. A. George, D. J. T. Hill, and A. K. Whittaker, “An investigation of the thermal and tensile properties of PFA following ??-radiolysis,” *Macromolecules*, vol. 36, no. 19, pp. 7132–7137, 2003.

- [81] G. Dlubek, A. Sen Gupta, J. Pionteck, R. Häßler, R. Krause-Rehberg, H. Kaspar, and K. H. Lochhaas, "Glass transition and free volume in the mobile (MAF) and rigid (RAF) amorphous fractions of semicrystalline PTFE: A positron lifetime and PVT study," *Polymer (Guildf)*, vol. 46, no. 16, pp. 6075–6089, 2005.
- [82] P. Fossati, A. Sanguineti, M. G. De Angelis, M. G. Baschetti, F. Doghieri, and G. C. Sarti, "Gas solubility and permeability in MFA," *J. Polym. Sci. Part B Polym. Phys.*, vol. 45, no. 13, pp. 1637–1652, 2007.
- [83] C. Yin, D. F. Miranda, S. Zhang, Q. Zhang, and J. Runt, "Microstructure evolution of poly[tetrafluoroethylene-co-(perfluoropropylvinylether)] films under uniaxial deformation," *Polym. (United Kingdom)*, vol. 99, pp. 480–487, 2016.
- [84] S. . K. Biswas and K. Vijayan, "Friction and wear of PTFE - a review," *Wear*, vol. 158, no. 1–2, pp. 193–211, 1992.
- [85] C. Pooley and D. Tabor, "Transfer of PTFE and Related Polymers in a Sliding Experiment," *Nat. Phys. Sci.*, vol. 237, pp. 88–90, 1972.
- [86] J. Khedkar, I. Negulescu, and E. I. Meletis, "Sliding wear behavior of PTFE composites," *Wear*, vol. 252, pp. 361–369, 2002.
- [87] B. C. Arkles and M. J. Schireson, "The molecular weight of PTFE wear debris," *Wear*, vol. 39, no. 1, pp. 177–180, 1976.
- [88] ASTM International, *Standard Test Method for Melt Flow Rates of Thermoplastics by Extrusion Plastometer (ASTM D1238 – 13)*, no. August. 2013, pp. 1–16.
- [89] J. M. Crosby, J. E. Theberge, and K. L. Talley, "Melt Processible Fluoropolymer Composites," *J. Elastomers Plast.*, vol. 13, no. July, pp. 149–155, 1981.
- [90] F. F. Ling, W. M. Lai, and D. A. Lucca, *Fundamentals of Surface Mechanics*, 2nd ed. New York: Springer, 2002.
- [91] A. Fujimori and Y. Hayasaka, "Changes in arrangement of lamella and fine crystallite in fluorinated 'crystalline' transparent fibers with drawing," *Macromolecules*, vol. 41, no. 20, pp. 7607–7615, 2008.

- [92] R. C. Schreyer, "STABILIZED TETRAFLUOROETHYLENE-FLUOROOLEFIN COPOLYMERS HAVING —CF₂SH END GROUPS," 1962.
- [93] J. W. Chang, J. Hegenbarth, J. P. Moseley, and H. S. Wu, "THERMOPLASTIC COPOLYMER OF TETRAFLUOROETHYLENE AND PERFLUOROMETHYL VINYL ETHER AND MEDICAL DEVICES EMPLOYING THE COPOLYMER," 7462675 B2, 2008.
- [94] *Standard Test Methods of Sampling and Testing Pulps to be Used in the Manufacture*, no. ASTM D3376-14. 2014.
- [95] C. Bunn, "The fine structure of polytetrafluoroethylene," *J. Polym. Sci.*, vol. 28, no. 117, pp. 365–376, 1958.

Vita

Mark Sidebottom was born on August 8th, 1991 to Jilda and John Sidebottom in Livingston, New Jersey. Mark graduated from Montville Township High School in 2009 and began his undergraduate work at The College of New Jersey during the Fall of 2009. Mark graduated from The College of New Jersey in 2013 with a BS degree (Magna Cum Laude) in Mechanical Engineering. Mark then began his doctoral degree at Lehigh University in the Mechanical Engineering and Mechanics Department under Dr. Brandon Krick in the summer of 2013. During his time at Lehigh, Mark has been awarded the Society of Tribologists and Lubrication Engineers Early Career award, the Society of Plastics Engineers Excellence in Polymer Science and Engineering award, the Emulsion Polymers Institute Dr. Les Sperling Travel Grant award, and is a Peter C. Rossin College of Engineering Doctoral Fellow. At the time of graduation, he published nine journal articles, presented at ten conferences, and six poster presentations on work he's completed during his doctoral studies. Mark is driven to improve efficiency and reliability of sliding contacts by continuing to research interfacial materials after graduation.